THE PRODUCTION OF HOT ELECTRONS BY THE TWO-PLASMON DECAY INSTABILITY IN A CO_2 LASER PLASMA INTERACTION

By

Lawrence E. Legault

B.Sc., York University, 1984

A THESIS SUBMITTED IN PARTIAL FULFILLMENT OF
THE REQUIREMENTS FOR THE DEGREE OF
MASTER OF SCIENCE

in

THE FACULTY OF GRADUATE STUDIES
DEPARTMENT OF PHYSICS

We accept this thesis as conforming
to the required standard

THE UNIVERSITY OF BRITISH COLUMBIA

April 1987

In presenting this thesis in partial fulfilment of the requirements for an advanced degree at the University of British Columbia, I agree that the Library shall make it freely available for reference and study. I further agree that permission for extensive copying of this thesis for scholarly purposes may be granted by the head of my department or by his or her representatives. It is understood that copying or publication of this thesis for financial gain shall not be allowed without my written permission.

Department of PHYSICS

The University of British Columbia
1956 Main Mall
Vancouver, Canada
V6T 1Y3

Date APR 27, 1987

ABSTRACT

The generation of hot electrons characterizing the two-plasmon decay (TPD) instability is investigated experimentally both in and out of the plane of polarization of a CO_2 laser incident on an underdense gas target. The results presented here show that, for high intensities ($I > \sim 3.5 \times 10^{13}$ W/cm^2 for a helium target, $I > \sim 5.5 \times 10^{13}$ W/cm^2 for a nitrogen target), the electron plasma waves (EPW's) generated by the TPD instability are modified by the electron decay instability (EDI). The relatively short scale lengths at the onset of TPD for these high intensities ($<\sim$0.125 mm) cause the EPW's propagating towards the higher density regions of the plasma to undergo the EDI resulting in EPW's which contain a vector component perpendicular to the plane of polarization and accelerate electrons by nonlinear Landau damping up to 55° outside the plane of polarization.

TABLE OF CONTENTS

LIST OF TABLES

LIST OF FIGURES

ACKNOWLEDGEMENTS

I would like to thank Dr. Jochen Meyer and Dr. Frank Curzon for their supervision and comments over the course of these studies. Great appreciation is felt to Hubert Houtman for his work designing, building, and implementing the multiframe interferometer used to provide much of the data on the helium jet. I would also like to thank Al Cheuck for his technical assistance and Lore Hoffmann for her aid in cutting through the red tape and for her cheerful attitude over the years.

CHAPTER I

INTRODUCTION

Thermonuclear fusion represents a potential source of vast amounts of energy. However, the ultimate goal of an economical fusion reactor will only be achieved by a thorough understanding of many subfields. For laser induced fusion one of the important areas is non-linear parametric instabilities. The results presented in this thesis examine the parametric instability of Two-Plasmon Decay (TPD) characterized by the generation of hot electrons.

The simplest model for controlled thermonuclear fusion is the Deuterium-Tritium model[1]

$$D + T = He^4 + n + 17.6\,MeV. \tag{1-1}$$

To attain the conditions whereby fusion can occur it is necessary that the nuclei have sufficient kinetic energy to overcome their Coulomb repulsion (a plasma temperature $\sim 10^8\,K$ or $10\,KeV$). In the inertial confinement scheme, multiple laser beams are focused on a target containing Deuterium-Tritium fuel. The ablation pressure produced by the absorption of laser energy results in an implosion which compresses a fuel pellet to the required density where a significant overlap of the nuclear wave functions occurs.

The density of the ablated plasma plays a crucial role in the scheme of inertial confinement fusion. Initially the laser beams will strike the surface of the pellet and ablate a plasma atmosphere which quickly achieves a density greater than the critical density (the maximum density at which the laser radiation can propagate in a plasma) before the conditions for the onset of fusion are attained in the pellet. Energy absorbed by the plasma is then transported from the critical density layer to the ablation layer (where pressure is maximum and the sign of the fluid velocity changes from towards the center to away from the center) by thermal conduction.

There are several mechanisms whereby the laser energy is absorbed by the plasma. 1) Inverse Bremsstrahlung — absorption by electron-ion collisions — occurs over a wide density range up to the critical density. The absorption efficiency of Inverse Bremsstrahlung is proportional to the square of the plasma density and is greater for low temperature plasmas due to the thermal velocity dependence of the electron scattering cross section. 2) Resonance Absorption — the excitation of plasma waves at the critical layer — is an efficient absorption mechanism but the hot electrons generated by this process are detrimental to the fusion scheme as discussed in the following paragraph. 3) Parametric Instabilities — Stimulated Brillouin Scattering, Self-Focusing, Paramatric Decay, Stimulated Raman Scattering (SRS), and TPD — arise in the underdense plasma and contribute to the absorption and scattering of laser energy.

To reach the high densities necessary for economical fusion the fuel pellet must undergo a tremendous density increase. Thermodynamic considerations[2] show that this is best accomplished by adiabatic compression. Simple examination of the first law of thermodynamics

$$dE = dQ - pdV \tag{1-2}$$

shows that the energy required to compress the pellet is at a minimum for dQ equal to zero. There are four reasons for which the enthalpy of the system would

be increased thereby resulting in non-adiabatic compression: thermal conduction, shockwaves, energetic photons (X-rays) and hot electrons. Although the majority of electrons produced in a laser-plasma interaction arise due to resonant absorption at the critical layer, there are a significant number of electrons produced by the TPD instability at quarter critical density.

The objective of this thesis is to study the three-dimensional spatial distribution of the electrons generated by the TPD instability and determine the energy distribution of these electrons. A brief survey of the theory of parametric decay is presented in Chapter II with TPD receiving a more extensive treatment. In Chapter III, there is a discussion of the apparatus used to produce and detect the electrons. A study of the temporal and spatial evolution of the plasma, determined by interferometric techniques, is presented in Chapter IV. Chapter V contains the results of the experiment which is discussed in Chapter VI where conclusions are reviewed.

CHAPTER II

THE GENERATION OF HOT ELECTRONS

The generation of hot electrons is detrimental to any laser fusion scheme. The interaction of these fast electrons with the fuel causes an increase in enthalpy hence decreasing the efficiency of the compression process. Hot electrons are produced by a variety of mechanisms, each involving the generation of an electron plasmon wave (EPW) which accelerates electrons to higher velocities through nonlinear Landau damping (electron trapping).

At the critical density layer EPW's are produced by resonant absorption.[3-5] If the wave vector of an incident electrodynamic (EM) wave is obliquely incident on an inhomogeneous plasma and if the wave is partially polarized in the plane of incidence then the electric field of the wave will have a component in the direction of the density gradient. This component can linearly excite EPW's with phase velocities propagating toward the lower density region.

Ion acoustic and EPW turbulence generate electrons by induced scattering.[6-9] Particles influenced by turbulent fields undergo a random walk in velocity space which tends to spread out the particles in velocity space. These low phase velocity disturbances are coupled to EPW's by ion fluctuations.

EPWs are generated in the underdense unmagnetized corona due to nonlinear parametric instabilities which arise when an incident EM wave decays into two daughter plasma waves.[10] The parametric decay instability involves an EM wave with large phase velocity exciting an EPW and an ion-acoustic wave. SRS arises when the incident EM wave decays into a backscattered EM wave and an EPW. TPD is closely related to SRS with two EPW's resulting from the decay of the incident EM wave.

The production of fast electrons by parametric instabilities can be enhanced by filamentation or self-focusing.[11,12] In this process the focal area of a section of the incident laser is decreased thus the local intensity is increased. Since both the threshold and the amplitude of parametric processes are intensity dependent, the amplitude of the EPW's produced will be increased and, hence, the number of fast electrons will also increase.

Of the processes discussed only the TPD instability is important for the conditions prevalent in this experiment. Interferometric data discussed in Chapter IV and by others[13,14] shows that the densities required for the onset of resonant absorption and parametric decay are not reached, the electrons generated by turbulence have insufficient energies ($< 30\,\mathrm{keV}$) to be detected by the apparatus used, SRS generated electrons have a growth rate maximized along the wave vector of the incident EM wave (an area not examined in this report), and filamentation as a parametric process merely augments other parametric processes. Hence, only the TPD instability was investigated in full.

1. Parametric Instabilities.

Parametric instabilities arise as a result of the nonlinear Lorentz forces present in laser-plasma interactions. When the quiver velocity v_o of the electrons in the EM field is greater than the electron thermal velocity v_e the laser is able to generate and maintain plasma waves despite the randomizing effects of thermal motion. Under

the proper conditions the daughter waves induced by these forces will interact with each other and be driven to resonance by the incident EM wave.

The plasma environment requires that any induced wave must satisfy certain dispersion relations. The three types of waves associated with parametric instabilities in an unmagnetized plasma are EM waves, EPW's, and ion acoustic (IA) waves with their respective dispersion equations:

$$\omega^2 = \omega_p^2 + k^2c^2, \qquad \text{(EM wave)} \qquad (2\text{–}1)$$

$$\omega^2 = \omega_p^2 + \frac{3}{2}k^2v_e^2, \qquad \text{(EPW)} \qquad (2\text{–}2)$$

and

$$\omega^2 = \left(\frac{Zk_bT_e + 3k_bT_i}{m_i}\right)k^2 \qquad \text{(IA wave)} \qquad (2\text{–}3)$$

where ω is the wave frequency, ω_p is the plasma frequency, k is the amplitude of the wave vector $\vec{k}$, c is the speed of light, k_b is Boltzman's constant, Z is the atomic number of the plasma material, T_e and T_i are the electron and ion temperatures, and m_i is the ion mass.

In addition to the dispersion relations, the incident and daughter waves must satisfy the frequency and wave vector matching conditions given by

$$\omega_o \simeq \omega_1 \pm \omega_2 \qquad (2\text{–}4)$$

and

$$\vec{k}_o \simeq \vec{k}_1 \pm \vec{k}_2 \qquad (2\text{–}5)$$

where the ω_o and $\vec{k}_o$ refer to the incident EM wave while $\omega_{1,2}$ and $\vec{k}_{1,2}$ refer to the daughter waves. These matching conditions arise by assuming that the interaction between the waves X_o, X_1, and X_2 is given by a set of nonlinearly coupled

equations:[15]

$$\left\{\frac{\partial^2}{\partial t^2}+2\gamma_1\frac{\partial}{\partial t}+\omega_1^2-c_1^2\frac{\partial^2}{\partial x^2}\right\}X_1(x,t)=\lambda_1 X_2(x,t)\,X_o(x,t) \tag{2–6a}$$

$$\left\{\frac{\partial^2}{\partial t^2}+2\gamma_2\frac{\partial}{\partial t}+\omega_2^2-c_2^2\frac{\partial^2}{\partial x^2}\right\}X_2(x,t)=\lambda_2 X_1(x,t)\,X_o(x,t) \tag{2–6b}$$

where $\gamma_{1,2}$ are damping rates, $c_{1,2}$ are phase velocities, $\lambda_{1,2}$ are coupling constants, and $\omega_{1,2}$ are natural frequencies of the unperturbed waves. It can be shown[10] that the driving forces of the right hand side of (2–6) can excite waves with modes $X_1(\omega,\vec{k})$ and $X_2(\omega_o\pm\omega,\vec{k}_o\pm\vec{k})$ which are coupled by (2–6)

$$\alpha\,X_1(\omega,\vec{k})-\lambda_1 E_o(\omega_o,\vec{k}_0)\left[X_2(\omega_o-\omega,\vec{k}_o-\vec{k})+X_2(\omega_o+\omega,\vec{k}_o+\vec{k})\right]=0 \tag{2–7a}$$

$$\beta\,X_2(\omega_o-\omega,\vec{k}_o-\vec{k})-\lambda_2 E_o(\omega_o,\vec{k}_o)\,X_1(\omega,\vec{k})=0 \tag{2–7b}$$

$$\delta\,X_2(\omega_o+\omega,\vec{k}_o+\vec{k})-\lambda_2 E_o(\omega_o,\vec{k}_o)\,X_1(\omega,\vec{k})=0 \tag{2–7c}$$

where

$$\alpha\equiv\omega_1^2-\omega^2-2i\gamma_1\omega+c_1^2k^2 \tag{2–8a}$$

$$\beta\equiv\omega_2^2-(\omega_o-\omega)^2-2i\gamma_2(\omega_o-\omega)+c_2^2(\vec{k}_o-\vec{k})^2 \tag{2–8b}$$

$$\delta\equiv\omega_2^2-(\omega_o+\omega)^2-2i\gamma_2(\omega_o+\omega)+c_2^2(\vec{k}_o+\vec{k})^2\,. \tag{2–8c}$$

The dispersion relation is obtained by setting the determinant of (2–7) to zero and finding solutions for growing instabilities where $\Im(\omega)>0$.

2. The Two-Plasmon Decay Instability.

The TPD instability is an anomalous absorption mechanism which involves an incident EM wave decaying into two plasma waves in the quarter-critical density

region (where the local plasma frequency is half that of the EM wave). Nonlinear Landau damping provides the mechanism whereby electrons are accelerated by the EPW's and it is the detection of these electrons that indicates the occurence of TPD. TPD as a parametric instability was first discussed by Silin,[16] Goldman,[17,18] and Jackson[19] with subsequent revisions by Lee and Kaw,[20] Liu and Rosenbluth,[21] Lasinski and Langdon,[22] and Simon *et al.*[23]

Current theory[22] holds that TPD along with SRS are two branches of the same parametric process where Wave 2 is longitudinal for both processes while Wave 1 may be either longitudinal (TPD), transverse (SRS), or a combination of the two. Without making any assumption as to the polarization of Wave 1, linear analysis yields the vector equation for E_1:

$$\begin{aligned}(\omega_2^2 - \omega_p^2 - 3k_2^2 v_e^2)\left[(\omega_1^2 - \omega_p^2)\,\vec{E}_1 - 3v_e^2\vec{k}(\vec{k}_1\cdot\vec{E}_1) + c^2\vec{k}_1\times(\vec{k}_1\times\vec{E}_1)\right] \\ = \frac{1}{4\omega_1\omega_2}\left[\frac{\vec{k}_1}{k_2^2}(\vec{k}_1\cdot\vec{v}_o) + \frac{\omega_1}{\omega_2}\vec{v}_o\right]\left[k_2^2(\vec{v}_o\cdot\vec{E}_1) + \frac{\omega_2}{\omega_1}(\vec{k}_1\cdot\vec{v}_o)(\vec{k}_1\cdot\vec{E}_1)\right].\end{aligned} \tag{2–9}$$

For a non-trivial solution for $\vec{E}_1$ the secular equation

$$\begin{aligned}\frac{4\,(\omega_2^2 - \omega_p^2 - 3k_2^2v_e^2)}{\omega_p^2} &= \frac{k_2^2}{k_1^2}\,\frac{(\vec{k}_1\times\vec{v}_o)^2}{(\omega_1^2 - \omega_p^2 - c^2k_1^2)} && \text{(SRS)} \\ &\quad + \frac{(k_1^2 - k_2^2)^2}{k_1^2\,k_2^2}\,\frac{(\vec{k}_1\cdot\vec{v}_o)^2}{(\omega_1^2 - \omega_p^2 - 3k_1^2v_e^2)} && \text{(TPD)}\end{aligned} \tag{2–10}$$

must be satisfied. If Wave 1 is longitudinal only the last term in (2–10) is retained and the dispersion relation for the TPD instability is recovered:

$$\frac{4\,(\omega_2^2 - \omega_p^2 - 3k_2^2v_e^2)}{\omega_p^2} = \frac{(k_1^2 - k_2^2)\,v_o^2}{k_2^2\,(\omega_1^2 - \omega_p^2 - 3k_1^2v_e^2)}. \tag{2–11}$$

The EPW's produced by TPD can be characterized by growth factors given by

$$A = A_o e^{\gamma t} \tag{2-12}$$

where A and A_o are the amplitudes of the EPW and the initial (thermal) wave. Jackson[19] shows that two sets of EPW's are generated with a growth factor proportional to $[\sin(\theta)\cos(\theta)]$ where θ is the angle between the EPW and k_o. Each set contains two EPW's in the plane of polarization, travelling in opposite directions to each other, perpendicular to the other set, with maximum growth at 45° to $\vec{k}_o$.

More recently Lasinski and Langdon[22] derive a threshold intensity given by

$$\left(\frac{v_o}{v_e}\right)^2 k_o L > 2.58 \tag{2-13}$$

and, for $\hat{k}_o = \hat{z}$ and $\hat{E}_o = \hat{y}$, a growth factor of

$$\gamma = \frac{k_o v_o}{4}\left(1 - \frac{3\sqrt{3}v_e^2}{2\omega_p v_o}k_y\right) - \frac{\omega_p}{k_y L} \tag{2-14}$$

for which growth is maximized at

$$\left(\frac{k_y}{k_o}\right)^2_{max} = \frac{8}{3\sqrt{3}}\frac{\omega_p^2}{v_e^2 k_o^3 L} \tag{2-15}$$

where k_y is the component of the EPW along $\hat{E}_o$.

Simon *et al.*[23] characterize the decay process by two parameters

$$\alpha \equiv \frac{4k_o|v_o|}{\omega} \tag{2-16}$$

and

$$\beta \equiv \frac{9v_e^4 k_o^2}{|v_o|^2 \omega_o^2} \tag{2-17}$$

and, in the limit of small β applicable for low temperature, high intensity, long wavelength interactions, give a threshold value of

$$\left(\frac{v_o}{v_e}\right)^2 k_o L > 3.094 \tag{2-18}$$

which, in practical units is given as

$$\frac{L_\mu \lambda_\mu I_{14}}{T_{keV}} > 61.25 \tag{2-19}$$

where L_μ is the scale length given by

$$L_\mu = \left(\frac{1}{n}\frac{dn}{dx}\right)^{-1} \tag{2-20}$$

in microns, λ_μ is the wavelength in microns, T_{keV} is the electron temperature in keV, and I_{14} is the intensity in units of 10^{14} W/cm^2. A value for (k_y/k_o) is derived as

$$\left(\frac{k_y}{k_o}\right)^2_{max} = 0.19 \left(\frac{I_{14}\lambda_\mu^2}{T_{keV}^2}\right) \tag{2-21}$$

For typical CO_2 laser-plasma interactions, $L_\mu = \sim 300$, $T_{keV} = \sim 0.3$, and $\lambda_\mu = 10.591$, (2-19) gives a threshold of $\sim 0.6 \times 10^{12}$ W/cm^2 for which

$$\left(\frac{k_y}{k_o}\right)^2_{max} = 1.42. \tag{2-22}$$

Figure 2.1 shows the two-dimensional wave vector diagram for TPD with the loci of maximum ω (for $k_y^2 = k_x[k_x - k_o]$). For the threshold intensity, the angle between k_1 and k_o is $\sim \pm 34°$ while that between k_2 and k_o is $\sim 180 \pm 56°$. For higher intensities the angles approach $\pm 45°$ and $180 \pm 45°$, respectively. In practice, strong Landau damping inhibits the growth rates of EPW's for $k_y/k_o > \sim 3.5$. Hence, for

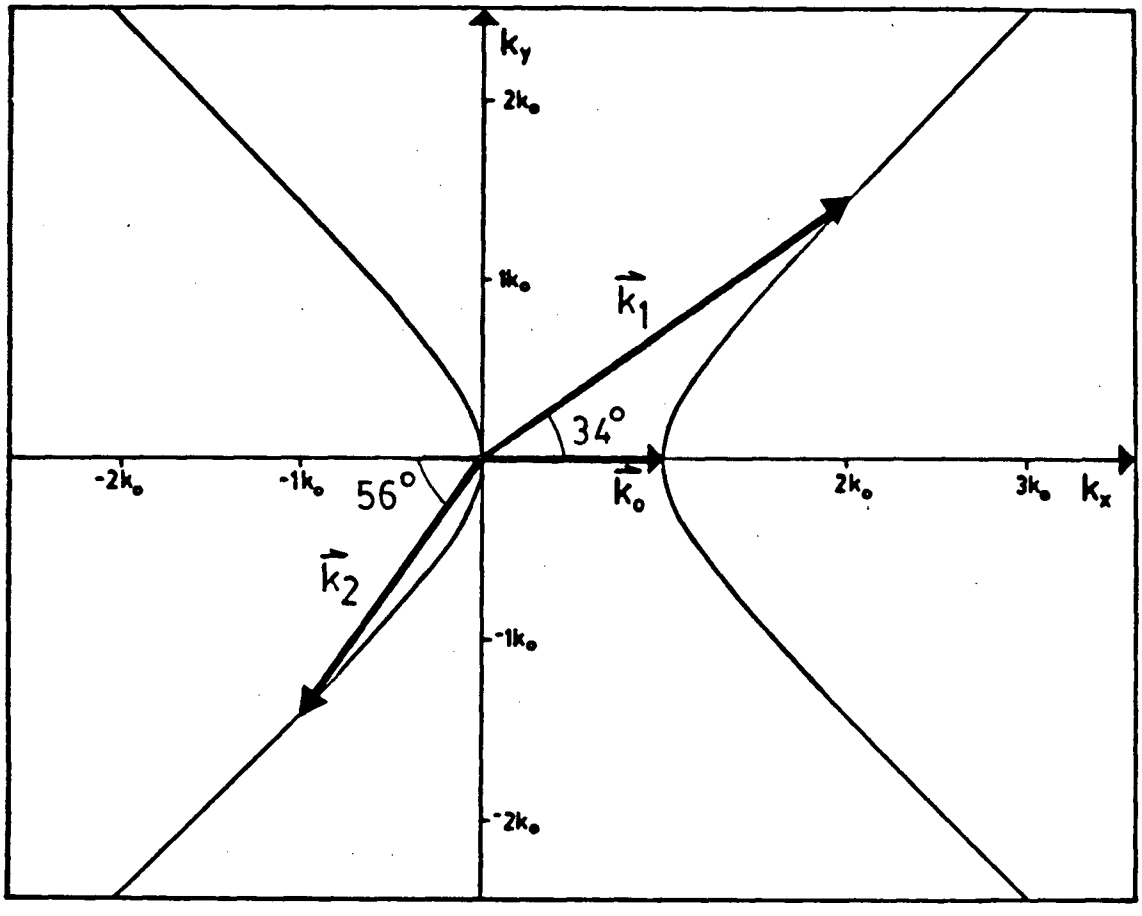

Figure 2.1 — The two-dimensional wave vector diagram for TPD.

detectable EPW's, the angles vary from $\sim 34°$ to $\sim 40°$ and from $\sim 180 \pm 56°$ to $\sim 180 \pm 50°$. Figure 2.2 shows the range of the magnitudes of k_y/k_o as a function of peak laser intensity. Curve (a) represents $(k_y/k_o)_{max}$ derived from (2–21) while curve (b) is the lower bound of the threshold intensity given by (2–22). The shaded area signifies the region where strong Landau damping inhibits the growth of the EPW's. The nature of the incident laser pulse (a 1.2 nsec rising front to the peak intensity followed by a 2.8 nsec fall) and the relatively short time scales of TPD, as discussed below, imply that EPW's could be produced at times with the laser intensity equal to the threshold up to the peak intensity.

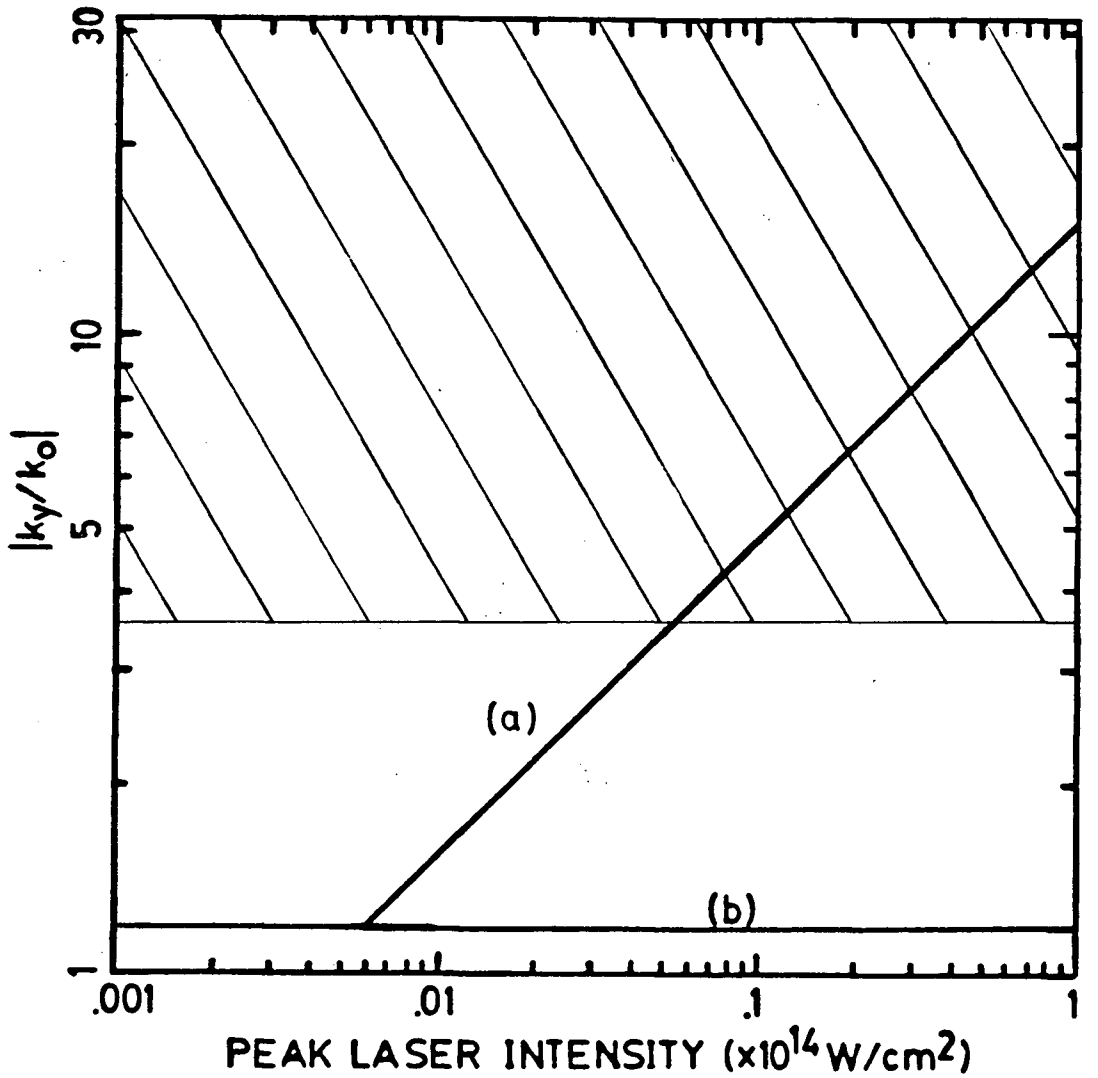

Figure 2.2 — The magnitude of $(k_y/k_o)_{max}$ as a function of (a) peak laser intensity and (b) the threshold intensity. The shaded region represents values of $(k_y/k_o)_{max}$ which are heavily damped due to Landau damping.

Computational and experimental evidence show that the EPW's generated by TPD do not continue to grow at the rates given by (2–14).[24–28] Various mechanisms have been proposed to account for the saturation, quenching and re-occurrence of the EPW's. Of the proposed mechanisms, pump depletion is unimportant for the high intensities available and nonlinear Landau damping cannot account for the low saturation levels observed.[28] Hence, the main saturation mechanisms applicable to

TPD are those which arise due to pondermotive effects: profile steepening and coupling of electrostatic waves to shorter wavelength ion fluctuations.

Pondermotive effects arise due to the interaction of EPW's given by[25]

$$f_p = -\left(\frac{e^2}{m\omega_p^2}\right) \bullet \nabla \left\{E_1^2 + E_2^2 + E_1 E_2 \exp\left[i\left(k_1 - k_2\right)x - i\left(\omega_1 - \omega_2\right)t\right] + c.c.\right\}. \tag{2-23}$$

The first two terms on the right hand side of (2-23) force particles out of the resonant density region resulting in a steepening of the density contours (profile steepening). The last two terms are rapidly varying compared to the time scales of the first two terms, however, with $\omega_1 \simeq \omega_2$ these terms become low frequency with spatial periodicity of

$$k_1 - k_2 \simeq 2k \tag{2-24}$$

since $k_1 \simeq -k_2$. This low frequency allows the pondermotive force to drive ion perturbations with $k_{ion} \simeq 2k$ which couple with EPW's of longer k which are heavily damped. Ion fluctuation coupling occurs within ~50 psec after the onset of TPD and is thought to be the main mechanism by which the EPW's are saturated. Profile steepening, occuring on longer time scales, eventually quenches TPD for periods of ~120–240 psec until the density profile relaxes and TPD reoccurs.

3. Nonlinear Landau Damping – Electron Trapping.

The presence of electrons characterizing EPWs can be attributed to nonlinear Landau damping.[29,30] Particles travelling along with the wave that have velocities nearly equal to the phase velocity of the wave will interact with the wave. Particles travelling slightly slower than the wave will be accelerated to the phase velocity resulting in a transfer of energy from the wave to the particles. Similarly, particles travelling slightly faster than the wave will be decelerated to the phase velocity resulting in a transfer of energy from the particles to the wave. However,

for the Maxwellian distribution[31-33] that the electrons have been shown to exhibit, there are more particles traveling at slower velocities than faster. Hence, the net energy transfer is from the wave to the particles and the wave is damped. For low amplitude EPWs linear Landau damping suffices to damp the wave and the electron velocity distribution remains essentially unchanged. Conversely, for large amplitude EPWs nonlinear effects become important as electrons become trapped in the wave potential and the electron velocity distribution is significantly altered.

Consider the potential of an EPW

$$\phi(z,t) = \phi_o \cos(\omega t - kz) \tag{2-25}$$

and an electron with velocity v'. In phase space

$$kx = kz - \omega t, \tag{2-26}$$

the potential is given by

$$\phi(x) = -\phi_o \cos(kx), \tag{2-27}$$

and the velocity of the electron is given by

$$v = v' - v_\phi. \tag{2-28}$$

Trapping of the electron will occur when its energy in the wave frame is less than the wave potential. Conservation of energy gives

$$\frac{1}{2}mv^2 - e\phi \cos(kx) = W \tag{2-29}$$

and it is clear that an electron with energy in the range

$$-e\phi \leq W \leq e\phi \tag{2-30}$$

is trapped by the potential. Integration of

$$v = \sqrt{\frac{2}{m}} \left[e\phi \cos(kx) + W \right]^{1/2} \tag{2-31}$$

yields the phase space trajectories shown in Figure 2.3. While untrapped electrons decelerate and accelerate when passing over the potential (without reversing direction), electrons in the shaded region (trapped electrons) oscillate in the troughs of the wave in phase space and are carried along with the wave at the phase velocity in the lab frame.

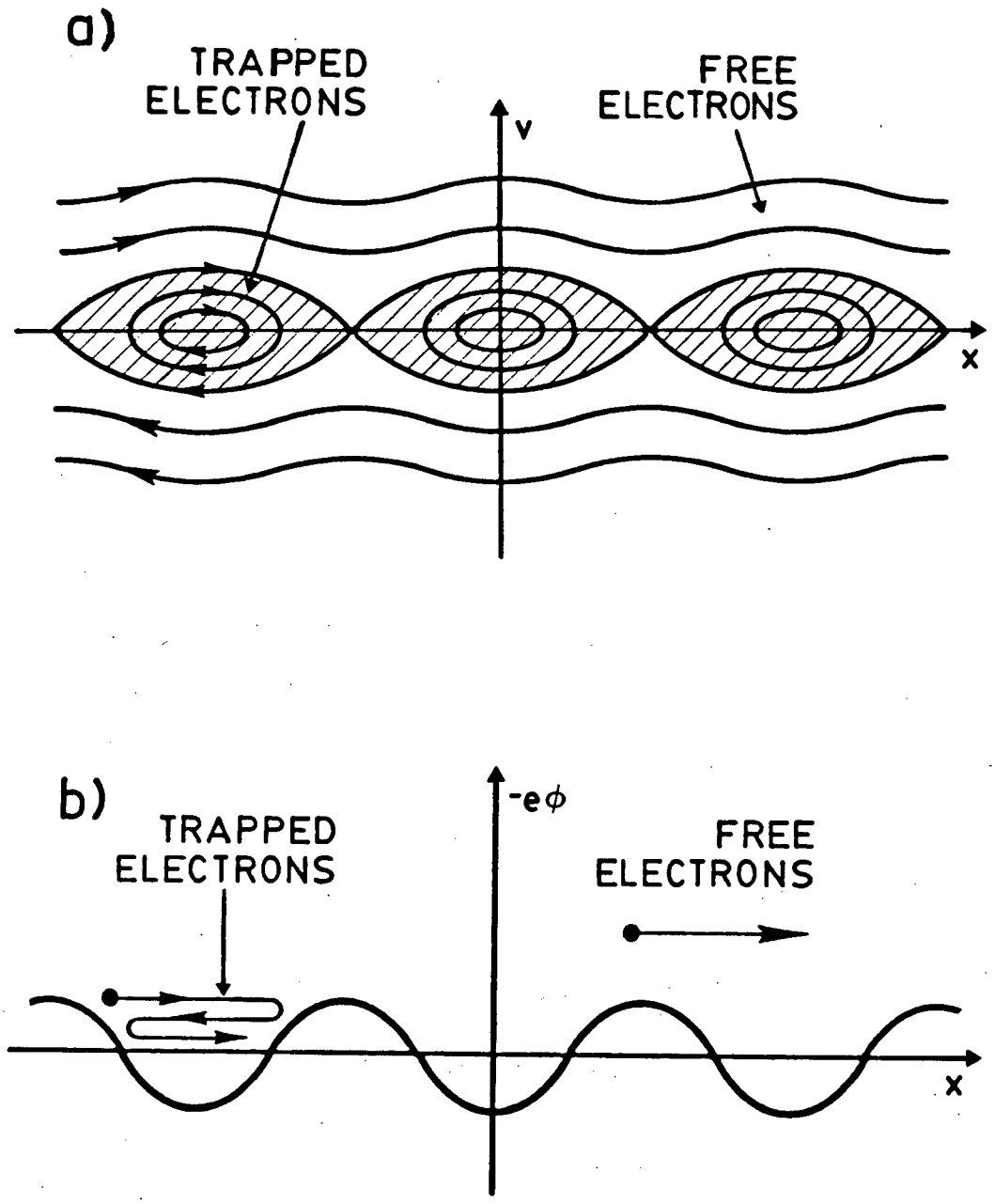

Figure 2.3 — a) The phase space trajectories of electrons in the b) potential of an EPW.

CHAPTER III

EXPERIMENTAL APPARATUS

The measurements reported in this thesis utilize five basic apparatus to investigate the hot electrons generated by a CO_2 laser produced plasma: 1) the CO_2 laser which produces and then interacts with the plasma; 2) the gas jet target where the plasma is formed; 3) a multi-frame Mach Zehnder interferometer which characterizes the plasma; and 4) the electron spectrometer and 5) the film holder which are used to analyze the electrons.

1. The CO_2 Laser.

A CO_2 laser developed over the years[13] was chosen to investigate the parametric effects evident when an intense laser beam interacts with a plasma. As discussed in §2.1, the ratio of the electron quiver velocity to the thermal velocity v_o/v_e, which is proportional to $I\lambda_o^2$, indicates the level of parametric instabilities that result in a laser plasma interaction. The high intensities and long wavelengths available with CO_2 lasers provide the ideal parameters to drive the instabilities.

Figure 3.1 shows the laser used. The hybrid oscillator consists of a folded continuous wave section and a high pressure pulsed section. The 100 nsec gain switched pulse produced by the hybrid oscillator is then linearly polarized before

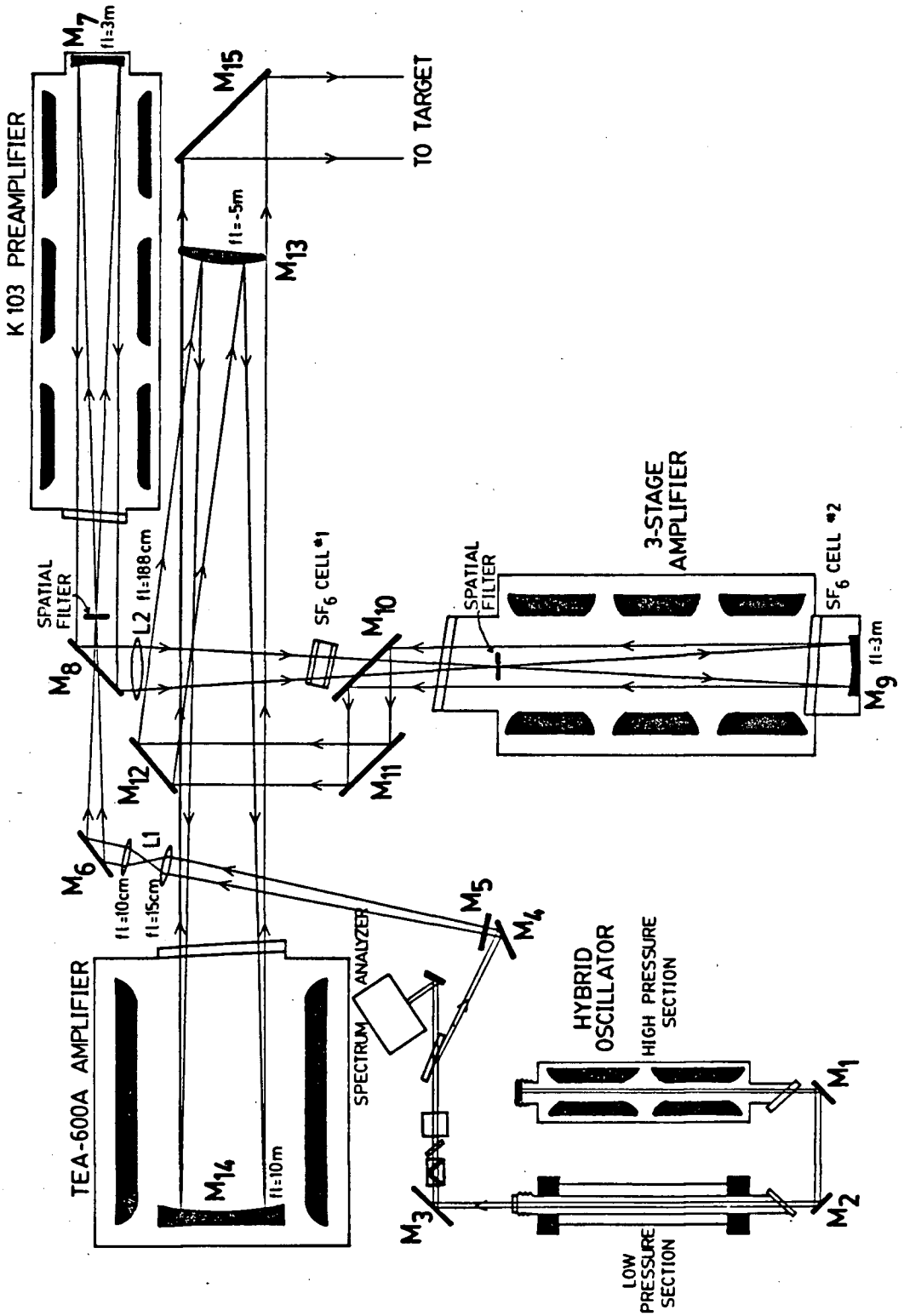

Figure 3.1 — The CO_2 laser.

passing through a short pulse generator which switches out a 2 nsec pulse at the peak of the 100 nsec pulse (the short duration of the pulse minimizes damage to the optics in the remainder of the system). The 2 nsec pulse is then passed through an amplifier chain before delivering up to 10 Joules to the target.

a. The Hybrid Oscillator. Temporally smooth Gaussian pulse shapes are desirable for laser produced plasma experiments. Mode beating, which causes severe temporal oscillations, can be eliminated with a single longitudinal, single transverse mode pulse. Hence, the hybrid oscillator (Figure 3.2), which produces pulses of this type, is used. In the continuous wave section, the single transverse mode is attained simply due to the large length to diameter ratio. The continuous wave section runs on a single longitudinal mode since the medium gain profile is homogeneously broadened. A temperature controlled germanium flat etalon at the exit of the continuous wave section controls the rotational line. The single longitudinal, single transverse mode continuous wave beam then mode locks the pulse from the high pressure pulse section and the output of the oscillator is then effectively a single longitudinal, single transverse pulse.

At room temperature, CO_2 lasers achieve greatest gain operating at the P(20) transition of the 10.6 μm band ($\lambda = 10.591\,\mu$m, $E = 0.117$ eV). The continuous wave section, operating at low pressure (26 Torr), at P(20) produces ~ 3 W with a mix of (He:CO_2:N_2) = (15:15:70) %. The output of the high pressure (1 atm) pulsed section is 1/4 - 1/2 J in a 100 nsec (FWHM) pulse with a mix of (He:CO_2:N_2) = (76:13:11) % flowing at a rate of 2.6 l/min.

b. Short Pulse Generation. The 100 nsec pulse produced by the hybrid oscillator would, if passed through the amplifier chain, heat the plasma and cause severe damage to the optics in the remainder of the system. To prevent this a Pockels cell is used to switch out a 2 nsec pulse which is then fed to the amplifier

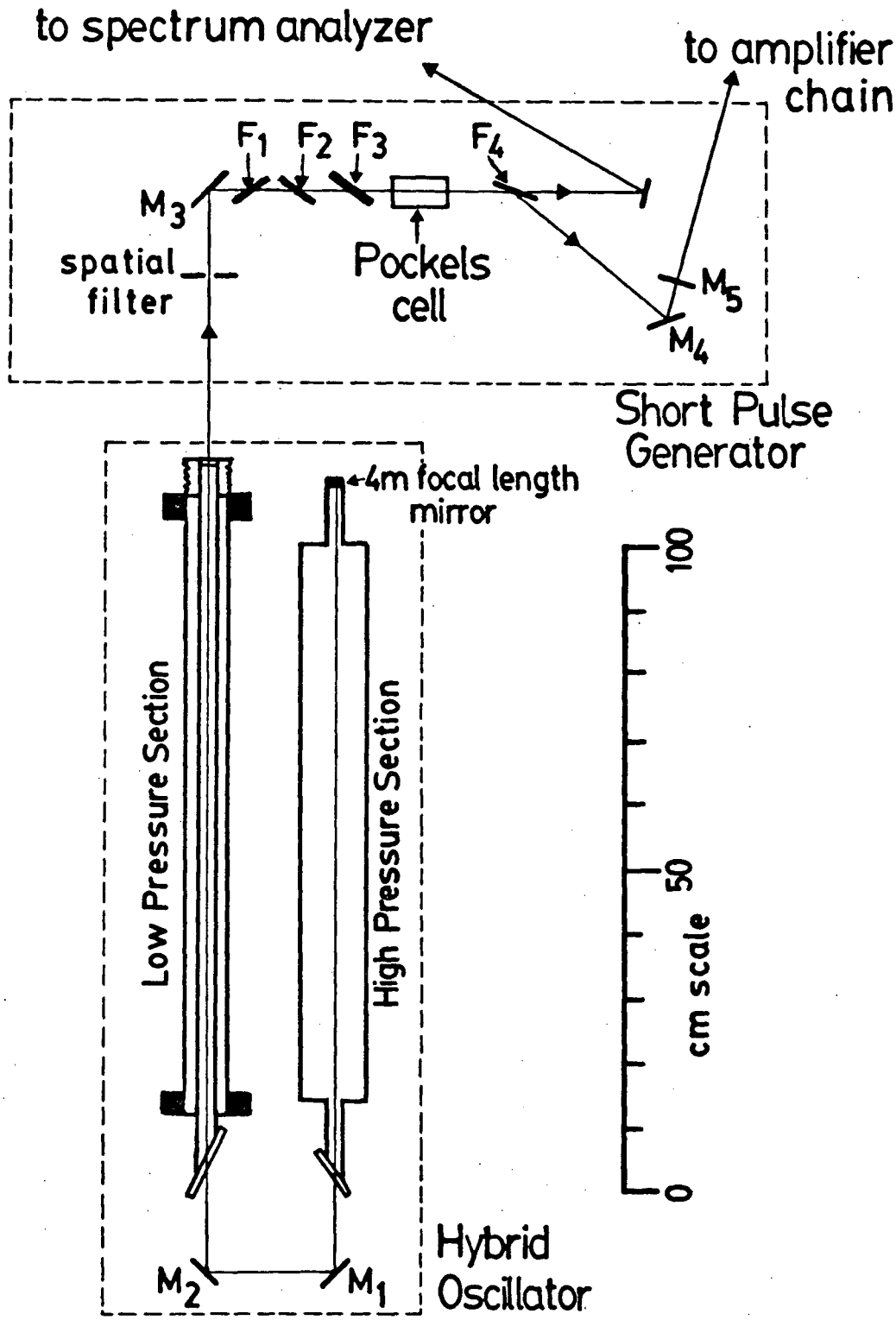

Figure 3.2 — The hybrid oscillator and short pulse generator.

chain. The cell is made from a GaAs crystal which, when no voltage is applied to the crystal, transmits a linearly polarized signal with little significant change to the signal. However, when voltage is applied to the crystal, a birefringence is produced which alters the polarization of the pulse from linear to elliptical.

Figure 3.2 shows the short pulse generater. The pulse from the hybrid oscillator is already partially polarized due to two intercavity KCl Brewster windows in the continuous wave section. Three germanium flats (F1, F2, and F3) positioned at the Brewster angle ensure maximum polarization prior to the beam entering the Pockels cell. With no voltage applied, the beam is transmitted by a fourth germanium flat (F4) at the Brewster angle to an Optical Engineering CO_2 Spectrum Analyzer. With applied voltage, the elliptically polarized beam is partially reflected by F4 and passed to the amplifier chain. A 2 nsec high voltage pulse (28 kV) applied to the Pockels cell near the peak of the 100 nsec pulse results in a symmetric, 2 nsec (FWHM), vertically polarized output pulse with power ~70 kW and energy ~0.15 mJ reflected off F_4. The polarization of the pulse is then flipped to the horizontal plane by mirrors M4 and M5 before it is passed to the amplifier chain.

c. The Amplifier Chain. The 2 nsec pulse output by the short pulse generator is passed through three amplifiers prior to impacting on the target. Each amplifier operates in the saturated regime and, since only 60 % of the available energy is absorbed in a single pass, each amplifier is double passed. The first amplifier is a Lumonics model K103 preamplifier (operating with the same gas mix as the high pressure section of the hybrid oscillator) which has a measured gain of 280 over an active length of 282 cm (~2 %/cm). The second amplifier is a home built three-stage amplifier (operating at 1 atm with a gas mix of ($He:CO_2:N_2$) = (63:25:12) % flowing at a rate of 8.5 l/min) which has a gain of ~200 over an active length of 180 cm (~3 %/cm). The final amplifier is a Lumonics model TEA600A

amplifier (operating with the same gas mix as the three-stage) which has a gain of ~20 over an active length of 100 cm (~3 %/cm). Typical output energies for an input pulse of 0.15 mJ into the chain are 0.042 J from the K103, 4.0 J from the three-stage, and 10.4 J in a 7.0 cm diameter beam from the TEA600A amplifier.

d. Backscattered, Leakthrough, and Self-Lasing Energies. Since up to 10 % of the laser energy can be backscattered and amplified on the return trip, precautions must be taken to prevent optical damage. Two spatial filters and a sharp focus between lenses L_1 and L_2 effectively absorb the reflected beam. The high intensities of the beam at the sharp focus break down the surrounding atmosphere dissipating the energy in an air spark.

Two absorption cells are used in the system to counter the effects of self-lasing and to enhance the contrast ratio of the Pockels cell. The gases used are freon-502 and ethanol which are strong absorbers in the 9 - 10.3 μm region, and SF_6 which absorbs weak signals at 10.6 μm but bleaches for strong signals. Hence the strong main pulse is only weakly attenuated by the bleached SF_6 while other signals are strongly absorbed. Helium is added to each cell to aid in the recovery of the bleached SF_6.

A small portion of the linaerly polarized 100 nsec pulse leaks through the short pulse generator when no voltage is applied to the Pockels cell. Despite the low power of this leakthrough (~0.5 % of the 2 nsec main pulse), the time scale is considerably longer and, hence, the energy is comparable to that of the main pulse (~25 %). Cell C_1, containing ~12 torr SF_6 and ~748 torr helium, dramatically reduces the level of leakthrough to acceptable levels through absorption of the low power leakthrough by the SF_6.

Parasitic oscillations arising due to random noise in the amplifier chain lead to amplifier self-lasing. Cell C_2, located at the rear mirror of the three-stage, filled with ~1.2 torr SF_6, ~28 torr ethanol, ~80 torr freon-502, and ~651 torr helium,

effectively eliminates this problem. The oscillations in the $9-10.3\,\mu$m band are absorbed by the freon-502 and the ethanol while those at $10.6\,\mu$m are absorbed by the SF_6 before they grow to appreciable strength.

e. Laser Output. Typically, output pulses of $0-10$ J in a 7.0 cm diameter beam at $10.591\,\mu$m with a roughly triangular pulse shape are observed. The rapid rise time of 1.2 nsec compared to a fall time of 2.8 nsec is attributed to the effects of the SF_6 in the absorption cells and to the saturation effects in the amplifiers. These pulses focused to intensities of up to 10^{14} W/cm^2 easily provide sufficient intensities to initialize non-linear parametric processes.

2. The Gas Jet Target.

Investigations of interactions occuring in an underdense plasma are easily accomplished with gas jet targets. The long scale lengths, the precise control over densities and the low bulk plasma movement makes the choice of a laminar jet flowing out of a planar Laval nozzle advantageous. Both helium and nitrogen were chosen as target gases flowing into a low pressure background helium gas.

The Laval nozzle, shown in Figure 3.3, has a fixed $70\,\mu$m throat and a mouth (controlled with stainless steal jaws) of 1.2 mm. The target gas is stored in a high pressure reservoir until a solenoid valve is triggered. The pressure change in the nozzle is detected by a piezo detector which sends a signal to fire the laser after a suitable delay to allow the jet to stabilize (≥ 10 msec).

The maximum density reached in the gas target is controlled by the pressure in the reservoir. Given the basic assumptions of 1) constant mass flow rate in the nozzle, 2) isentropic and adiabatic flow in a perfect gas, and 3) the first law of thermodynamics, it can be shown[34,35] that the ratio of pressure at any point in the

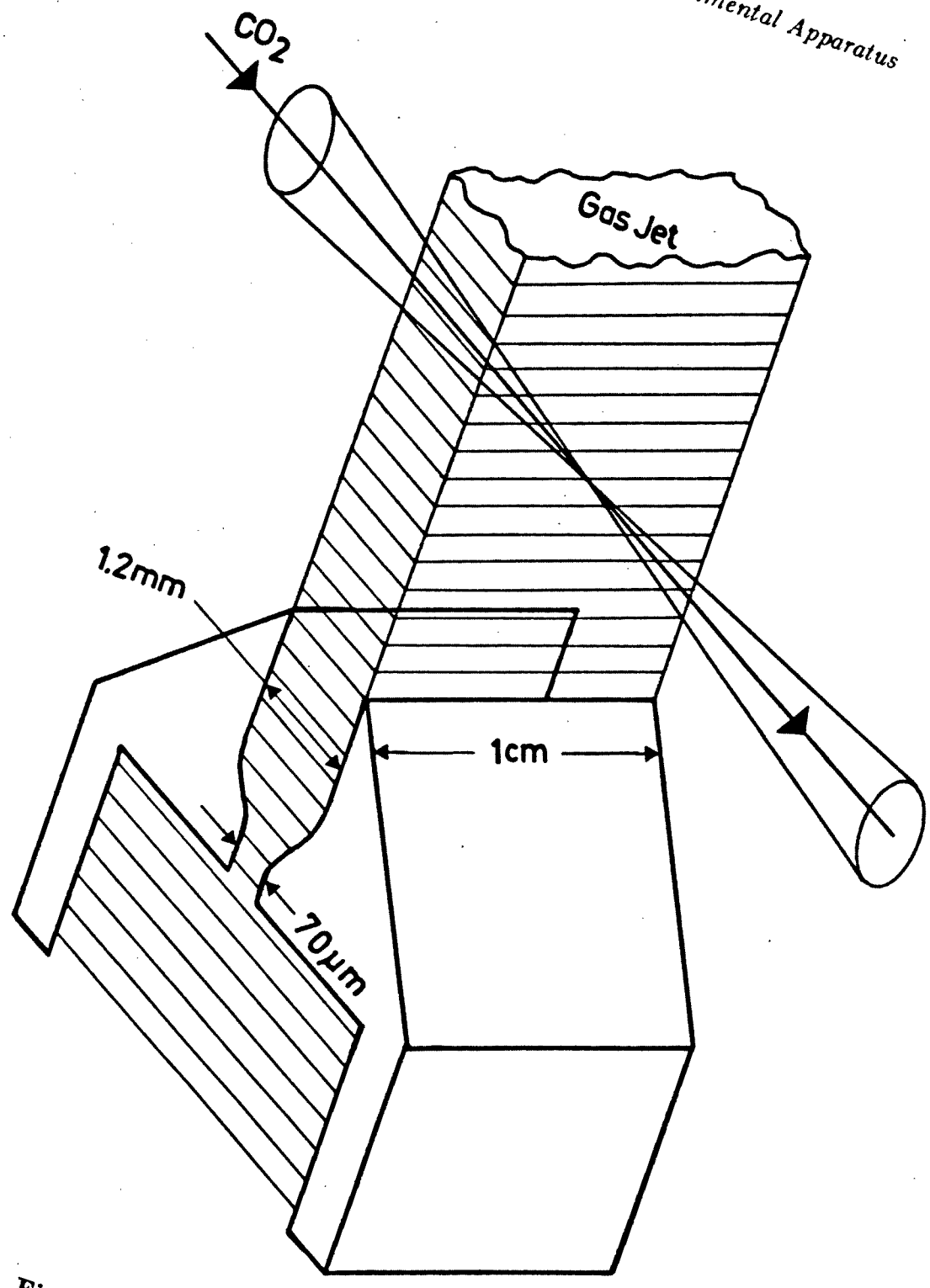

Figure 3.3 — The Laval gas jet nozzle.

nozzle p to the pressure in the reservoir p_o is related to the local Mach number M by

$$\frac{p}{p_o} = \left(1 + \frac{\gamma - 1}{2} M^2\right)^{-\gamma/(\gamma-1)} \tag{3-1}$$

where γ is the ratio of specific heats, and that the cross-sectional area a is given by

$$a = \frac{m}{M\sqrt{\gamma p_o \rho_o}} \left(\frac{p}{p_o}\right)^{-(\gamma+1)/2\gamma} , \tag{3-2}$$

where m is the mass flow rate. The Laval nozzle is designed such that the Mach number at the throat equals one. Hence, the Mach number at the exit M_e can be determined from the ratio of cross sectional areas at the throat and exit

$$\left(\frac{a_e}{a_t}\right)^2 = \frac{1}{M_e^2}\left[\frac{2}{\gamma+1}\left(1 + \frac{\gamma-1}{2}M_e^2\right)\right]^{(\gamma+1)/(\gamma-1)} . \tag{3-3}$$

Once M_e is determined, the design pressure ratio p_o/p_e can be found from equation (3-1).

The nozzle used has a throat to exit area ratio of 17 and a design pressure ratio of 648 for helium ($\gamma = 5/3$) and of 285 for nitrogen ($\gamma = 7/5$). Assuming complete ionization, a density of $1.17\,n_c$ would be reached with a nitrogen jet in a 5 torr background while a density of $0.537\,n_c$ would be reached with a helium jet in an 8 torr background. A maximum of 100 psi imposed by the limits of the piezo detector did not allow higher densities to be reached for the helium jet. Interferometric results, reported by others[13,14] and in Chapter IV, show that densities in the range $0.4\,n_c \leq n \leq 0.5\,n_c$ are generally achieved with both gases. The fact that the observed densities are lower than those predicted is attributed to plasma expansion. This expansion has less effect on the helium jet due to the fact that, despite the higher ionization potential of helium compared to nitrogen, helium ionizes at a

faster rate due to a cascade process resulting from the collisions between the helium and energetic electrons.[36]

The nozzle is enclosed in the target chamber shown in Figure 3.4. The chamber is a 60 cm diameter, 38 cm long cylinder standing on end with a 20 cm extension holding a f/5, 50 cm KCl lens which focuses the 7.0 cm beam down to 50 μm at the gas jet thus attaining intensities up to 10^{14} W/cm^2. Three large (10 cm) and 16 smaller (5 cm) ports arranged symmetrically about the cylinder allow access for optical diagnostics. Automatic controls[37] regulate the evacuation and filling of the chamber and the high pressure reservoir.

3. The Multi-Frame Interferometer

A thorough understanding of the plasma is necessary in order to explain the processes occurring in laser-plasma interactions. Interferometers are simple tools which can measure scale lengths, densities, expansion rates and temperatures of a plasma. Knowledge of these parameters are essential in the application of the theory presented in §2.2. The use of multi-frame interferometry provides the advantages that the temporal separation between the frames is accurately known to within 1% and that the four frames follow the history of a single laser-plasma interaction.

a. Interferometric Theory. Interferometric techniques are based on the phenomenon of interference fringes which result when two monochromatic, coherent beams are superimposed after travelling paths of different optical lengths.[38] The relative phase shift between the two beams gives rise to an interference term in the intensity of the superimposed beams which, in turn, accounts for the interference fringes observed. The presence of any localized variation of the optical index of refraction will modify the phase shift of the section of the scene beam passing through the variation relative to the rest of the beam. This phase shift is evident as

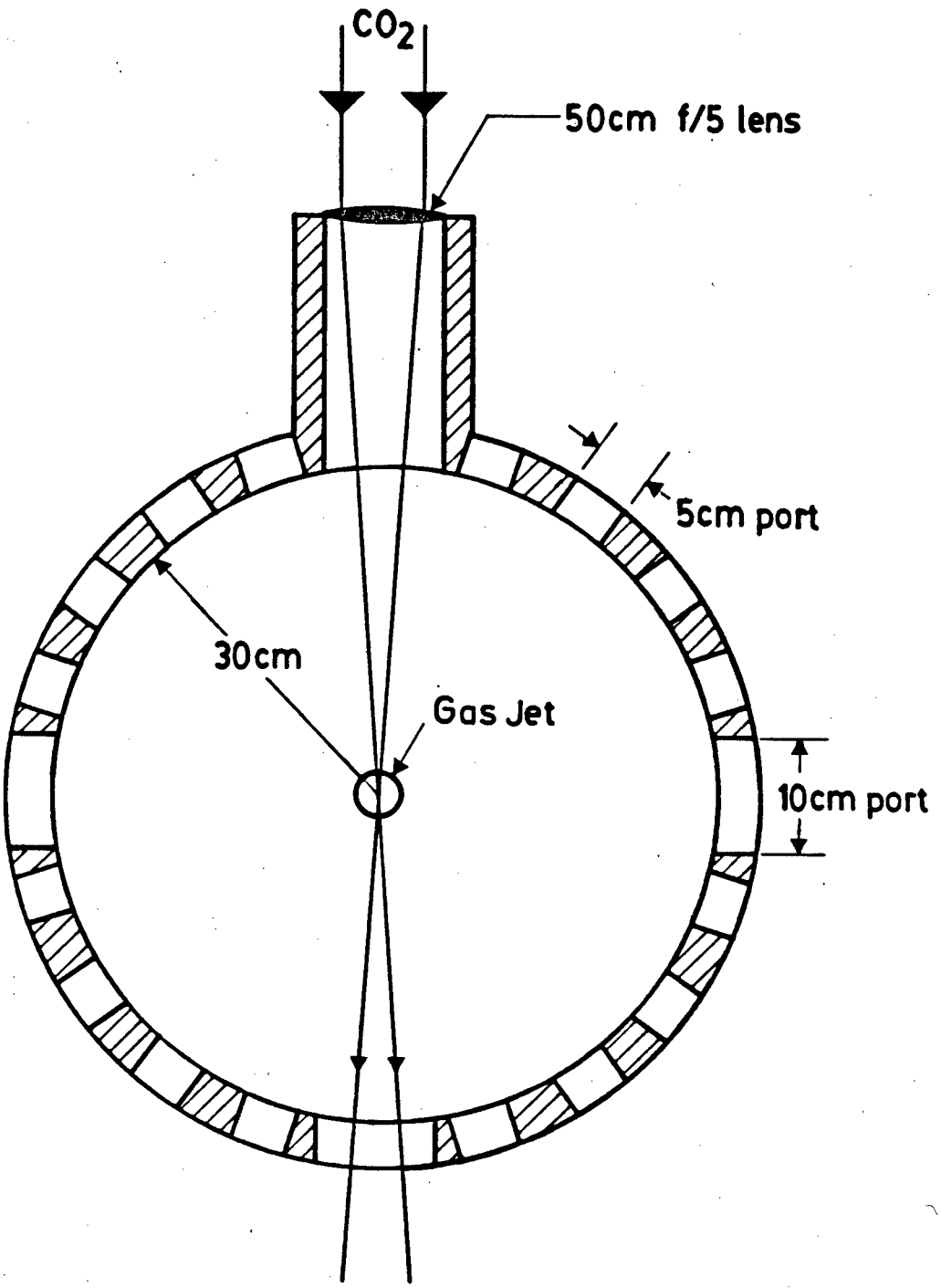

Figure 3.4 — The target chamber.

a shift in the fringes of the interference pattern. This shift f is easily related to the difference between the actual length of the variation L and the optical path length:

$$f = \frac{2\pi}{\lambda} \int_{-L/2}^{L/2} (\mu - 1)\, dl \tag{3-4}$$

where λ is the wavelength of the ruby beam in vacuum and μ is the index of refraction given by[10]

$$\mu = \left(1 - \frac{\omega_p^2}{\omega^2}\right)^{1/2} \tag{3-5}$$

or

$$\mu = \left(1 - \frac{n_e}{n_c}\right)^{1/2} \tag{3-6}$$

where n_e is the electron density and n_c is the critical density. Hence, the plasma density can be determined from measurements of the fringe shifts obtained. Since we are dealing with densities below critical density, μ will be less than one and, hence, the fringe shifts will be negative — the fringes will shift towards the incoming CO_2 laser.

The fringe shift given by (3–4) is the result of the integrated sum of infinitesimal density variations along the path lengths perpendicular to the CO_2 laser beam. Since the plasma density in the path is not constant through the plasma, the fringe shifts must be unfolded. If cylindrical symmetry is assumed, (3–4) can be transformed to cylindrical coordinates and integrated over the half diameter

$$f = \frac{4\pi}{\lambda} \int_y^\rho r\,(\mu - 1)\,\left(r^2 - y^2\right)^{-1/2}\, dr. \tag{3-7}$$

Abel inversion[39] of (3–7) gives

$$\mu - 1 = -\frac{\lambda}{2\pi^2} \int_r^\rho \frac{\partial f}{\partial y} \left(y^2 - r^2\right)^{-1/2} dy \tag{3–8}$$

or, by (3–6)

$$n_e = n_c - n_c \left[1 - \frac{\lambda}{2\pi^2} \int_r^\rho \frac{\partial f}{\partial y} \left(y^2 - r^2\right)^{-1/2} dy\right]^2 . \tag{3–9}$$

b. The Multi-Frame Interferometer. A Mach-Zehnder interferometer[40] (Figure 3.5) was chosen due to the ability to attain large separations between the scene and reference beams. This allowed for large plasma expansions to take place with out interaction of the plasma with the reference beam. The strength of any EM wave plasma interaction is dependent on the ratio between the plasma frequency and the wave frequency. Hence, a 50 psec, Q-switched, mode-locked, cavity dumped ruby laser[41] (wavelength 694.3 nm) was chosen as the probe beam. The interference fringes were recorded on polaroid film which allowed instant data analysis.

The frame delay mechanism, which provides the multi-frame attributes of the interferometer, consists of an uncoated BK7A crown glass flat ($\mu = 1.50$) which has a wedge angle $\epsilon = 30 \pm 5$ min oriented with its narrowest part up. Figure 3.6 shows the top view of the wedge where the wedge angle is directed down into the page. Four spatially and temporally separated beams arising from reflections at the surfaces of the wedge are utilized while other reflections are spatially filtered out of the apparatus by the neutral density filter holder in Figure 3.5. Beams 1 and 2 are temporally separated by a difference in optical path length of

$$2\mu a - c = 2t \left(\mu^2 - \sin^2 \theta\right)^{1/2} = 2.85\,\text{cm} \tag{3–10}$$

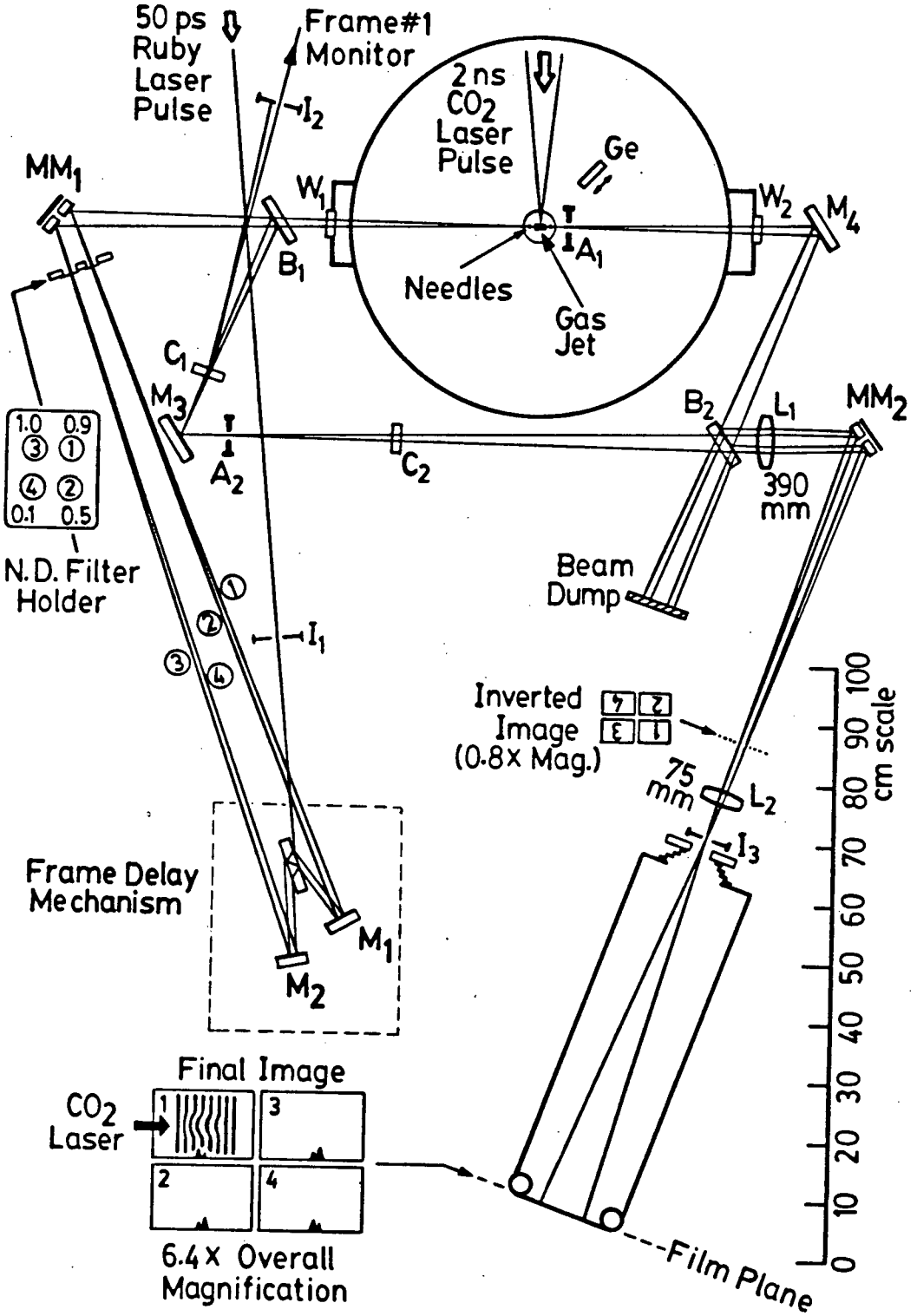

Figure 3.5 — The multi-frame interferometer.

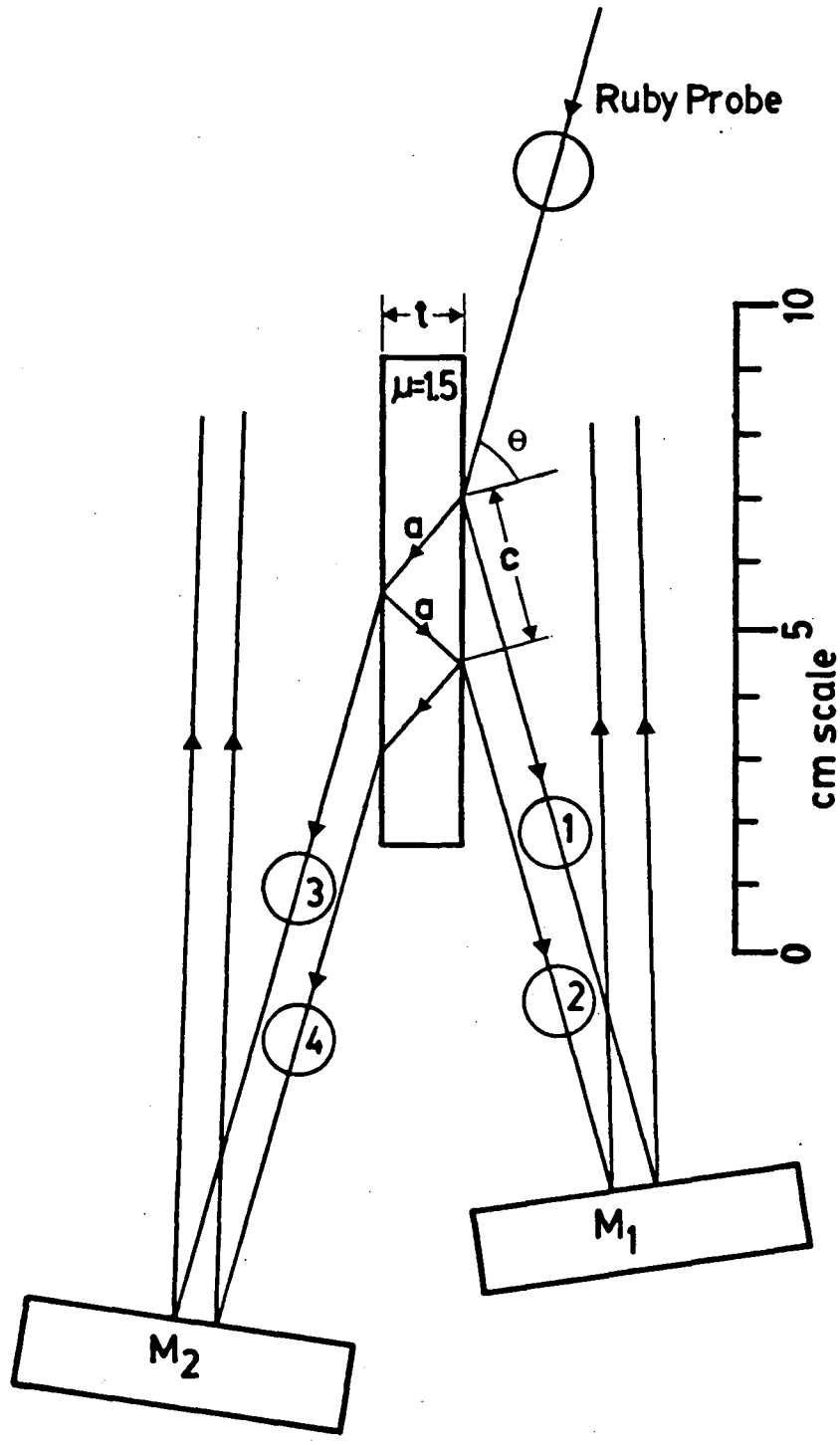

Figure 3.6 — Top view of the frame delay mechanism.

or a temporal delay of 95 psec for $t = 12.45$ mm, $\theta = 74.7°$. Similarly beams 3 and 4 are also separated by 95 psec. These calculations assume the thickness of the wedge is constant over the paths travelled. In fact, the paths in Figure 3.5 are not in the plane of the page. However, with a wedge angle of 30 min, the difference in path lengths is less than 0.002% and is neglected. The difference in path lengths from the wedge to mirrors M1 and M2 allow temporal adjustments to be made for the two sets of beams such that the time delay between all four beams is 95 psec.

Spatial separation of the beams is easily achieved with the wedge. Figure 3.7 shows the edge on view of the wedge where all four beams are directed out of the page. For small ϵ and α,

$$\begin{aligned} \alpha &= \mu\beta \\ \gamma &= \mu(2\epsilon + \beta) \\ \delta &= \mu(\epsilon + \beta) \\ \varphi &= \mu(3\epsilon + \beta) \end{aligned} \tag{3-11}$$

and the angular separation between the two sets of beams on each side of the wedge is given by

$$\gamma - \alpha = \varphi - \delta = 2\mu\epsilon. \tag{3-12}$$

For the wedge used, $\mu = 1.5$ and $\epsilon = 30 \pm 5$ min. Hence, at 1 meter the spatial separation of the beams is ~ 26 mm.

To facilitate alignment of the four beams two multiple mirror mounts MM_1 and MM_2 are used. Each mount consists of four individualy adjustable one inch round mirrors, thus each beam could be directed to the same point in the jet by MM_1 and to their proper position in the film plane by MM_2. Two square apertures, A_1 in the scene beam and A_2 in the reference beam, are used to prevent overlapping of the beams in the film plane.

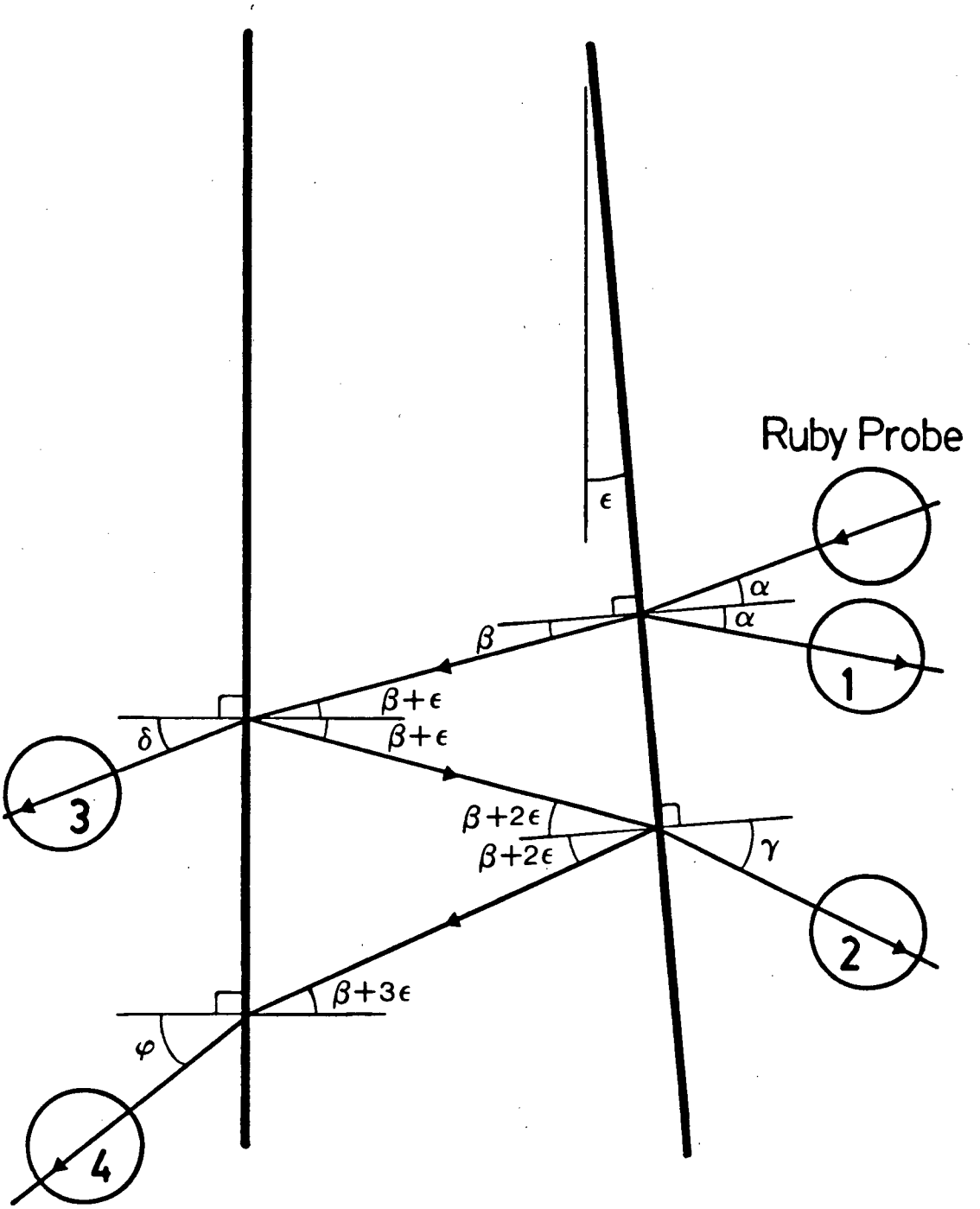

Figure 3.7 — Edge-on view of the frame delay wedge.

Two flats C_1 and C_2 in the reference beam compensate for the presence of the two windows in the gas chamber. Without these flats the scene beam experiences both a temporal delay and a shift in spatial separation relative to the reference beam. Although the beam path of the scene beam could be shortened to compensate for the temporal delay, the beam path must be lengthened to compensate for the shift in spatial separation. Hence, the presence of these flats is necessary.

The four beams are of unequal intensity due to the nature of the frame delay mechanism. To counter this effect, neutral density filters are placed in the beam just prior to the first multiple mirror mount MM_1. This resulted in four interferograms of equal intensity in the final image.

Lenses L_1 and L_2 imaged the interferograms at the film plane. The combination of these two lenses results in a calculated magnification of $6.4\times$ which was confirmed by photographing a mm scale placed at the jet. Photographs of the interference fringes with no plasma present show a fringe separation of 0.294 mm in the film plane representing a resolution of 46 μm at the jet.

Absolute timing of the ruby pulse relative to the CO_2 pulse is easily determined. It has been shown that optically induced carriers in a semiconductor sample effectively attenuates 10 μm radiation.[42] With a germanium flat positioned over the jet at 45° to the incident CO_2 pulse, both the incident ruby and CO_2 pulses were observed with a Hamamatsu R1193U-03 detector and a Labimex P005 room temperature HgCdTe detector, respectively, on a single Tektronix 7104 oscilloscope with two 7A29 plug-ins while the transmitted CO_2 pulse was monitored by a second P005 detector on a second Tektronix 7104 oscilloscope with a 7A29 plug-in. Absorption of the ruby pulse creates free carriers in the germanium flat which reflect the incident CO_2 pulse. Hence, any decrease in the transmitted signal is attributed to the arrival of the ruby pulse at the jet and the time delay between the arrival of the two incident monitor signals can be calibrated to the arrival of the two pulses at the jet.

4. The Electron Detectors

The electrons trapped by the EPWs are detected and analyzed by an electron spectrometer and by exposing the electrons to photographic film (KODAK Direct Exposure Film). Analysis of the energy spectrum obtained from the spectrometer leads to a determination of the thermal velocities of the electrons while investigation of the film exposed by the electrons reveals the wave vectors of the EPWs.

a. The Electron Spectrometer. The spectrometer used is a five channel self-focusing spectrometer constructed with two permanent magnets as shown in Figure 3.8. The entire spectrometer cavity is light tight with the entrance covered with a thin (25 μm) Beryllium foil. The five detectors are NE102 scintillator discs embedded in an aluminum block and are connected to the cathode of an optical multi-channel analyser (OMA) via optical fibre. The magnetic field channels electrons with energies of 32, 88, 173, 285, and 407 keV to the five discs.

The response of the NE102 scintillator to electrons is well documented[43–45] and is known to be linear with respect to the energy of the electrons. The specific fluorescence dS/dr resulting from the passage of ionizing particles (electrons) through the scintillator is given by

$$\frac{dS}{dr} = \frac{A\,(dE/dr)}{1 + kB\,(dE/dr)} \quad . \tag{3–13}$$

For electrons dE/dr is small, hence

$$\frac{dS}{dr} = A\,\frac{dE}{dr} \tag{3–14}$$

or

$$S = AE. \tag{3–15}$$

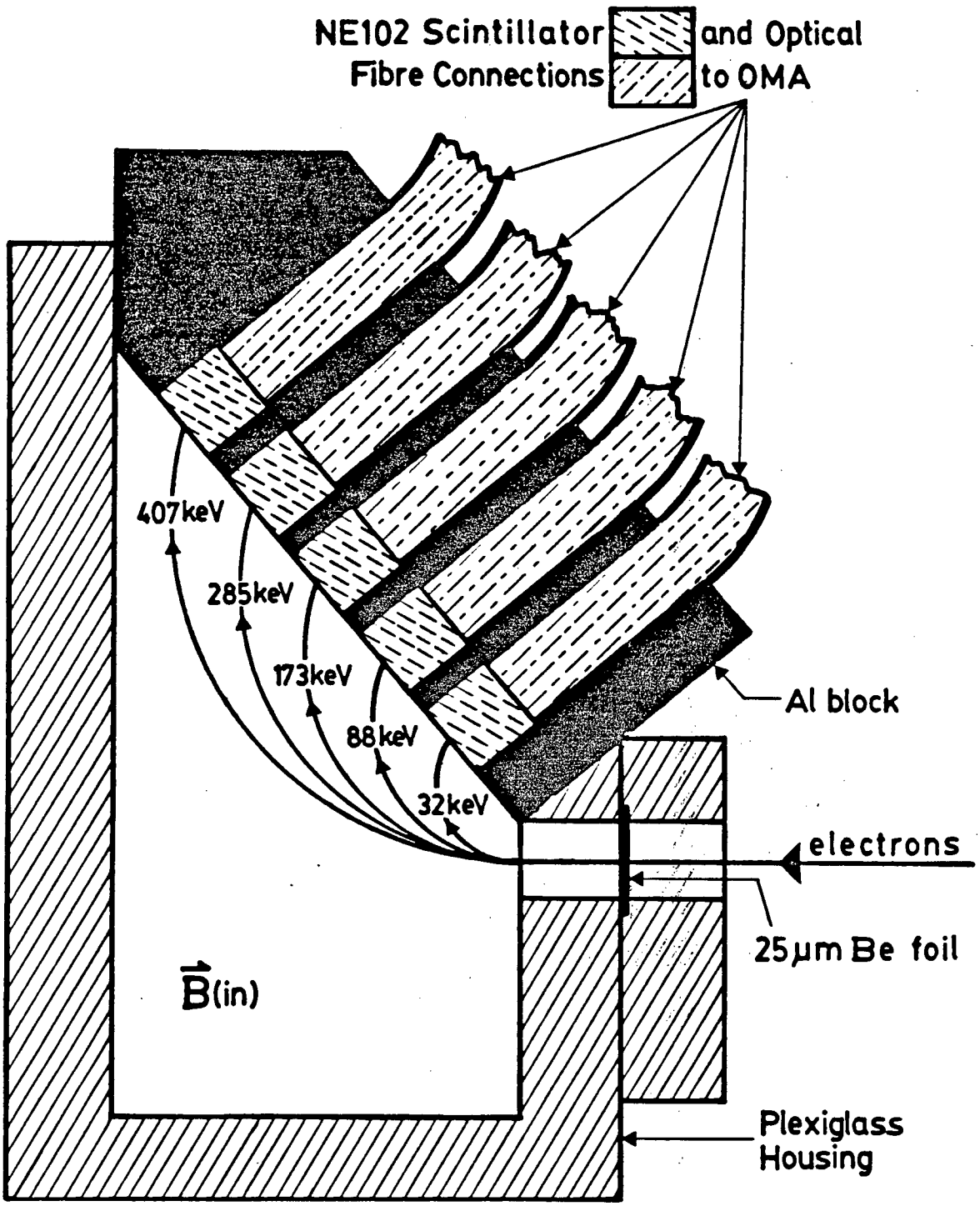

Figure 3.8 — The electron spectrometer.

The use of optical fibre to transmit the scintillator signals to the OMA results in an attenuation of the signals. The fibre used was obtained from Welch Allyn, Skaneateles Falls, N.Y. and has an attenuation coefficient of $0.032\,cm^{-1}$ for scintillation light. The 60 cm of fibre used represents a 85 % loss in signal from the spectrometer to the OMA.

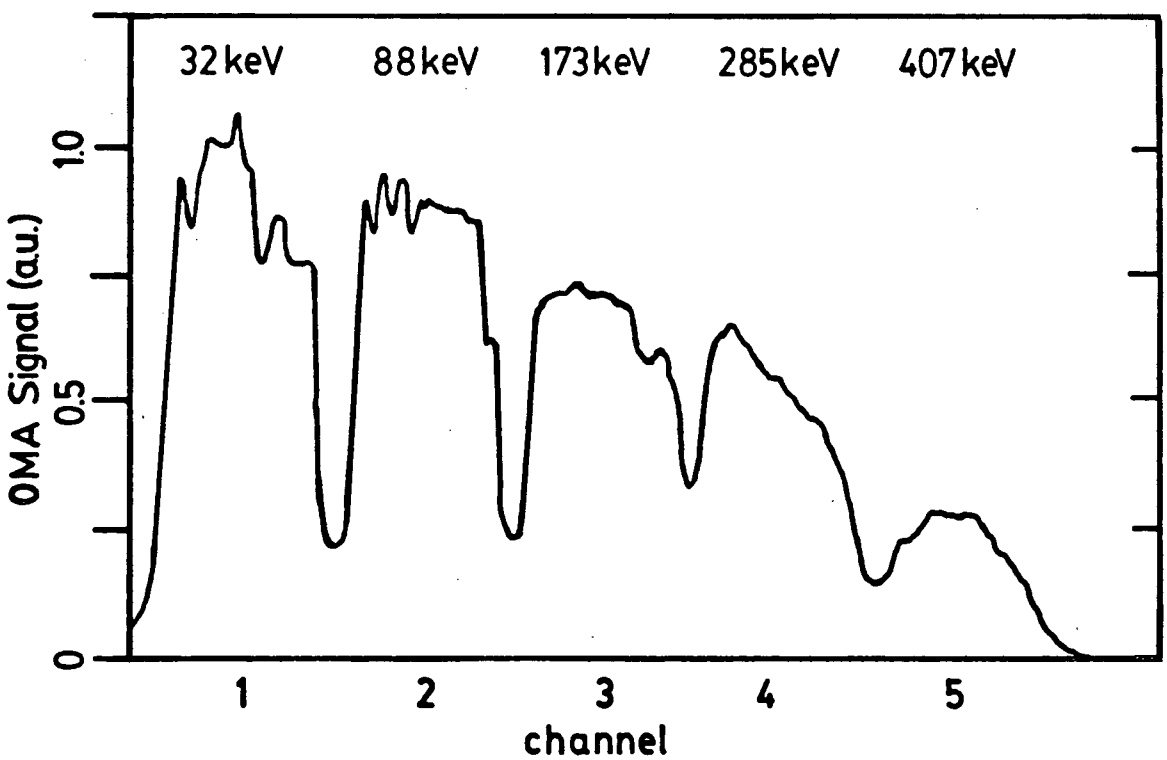

Figure 3.9 — Signal obtained from uniform illumination of the five scintillator discs by ultra-violet radiation.

The signals received at the OMA exhibit channel to channel variations in amplitude. Figure 3.9 shows the spectrum obtained from uniform illumination of the five scintillator discs by uniform ultra-violet light. The variance in channel output is attributed to the manufacturing process and to the inability to achieve perfect

alignment of the optical fibres with the cathode of the OMA. Table III–I shows the normalization factors used to negate this variance and the energy dependence in the scintillator signal.

CHANNEL	ELECTRON ENERGY (keV)	NORMALIZATION FACTORS
1	32	1.000
2	88	0.387
3	173	0.244
4	285	0.167
5	407	0.238

Table III–I — Calibration factors used to normalize the spectrometer channel signals.

b. Photographic Detection of Electrons. The spatial distribution of the hot electrons can be determined with the use of photographic film. The film, wrapped in 7 mg/cm^2 thick aluminum foil is bent into the shape of a cylinder with a 5 mm diameter, co-axial with the laser beam in the center as shown if Figure 3.10. The coverage of the film is limited by the f/5 optics and the gas jet nozzle as shown in Figure 3.10.

The thickness of the foil is not sufficient to stop the majority of the hot electrons generated.[46,47] The electron range in a material can be expressed in the form[46]

$$R_e\rho = \alpha E_e^n \times 10^{-8} \qquad (3\text{–}16)$$

where $R_e\rho$ is the thickness of the foil in g/cm^2, E_e is the electron energy in keV, and the values of α and n have been determined experimentally[48] to be 540 and

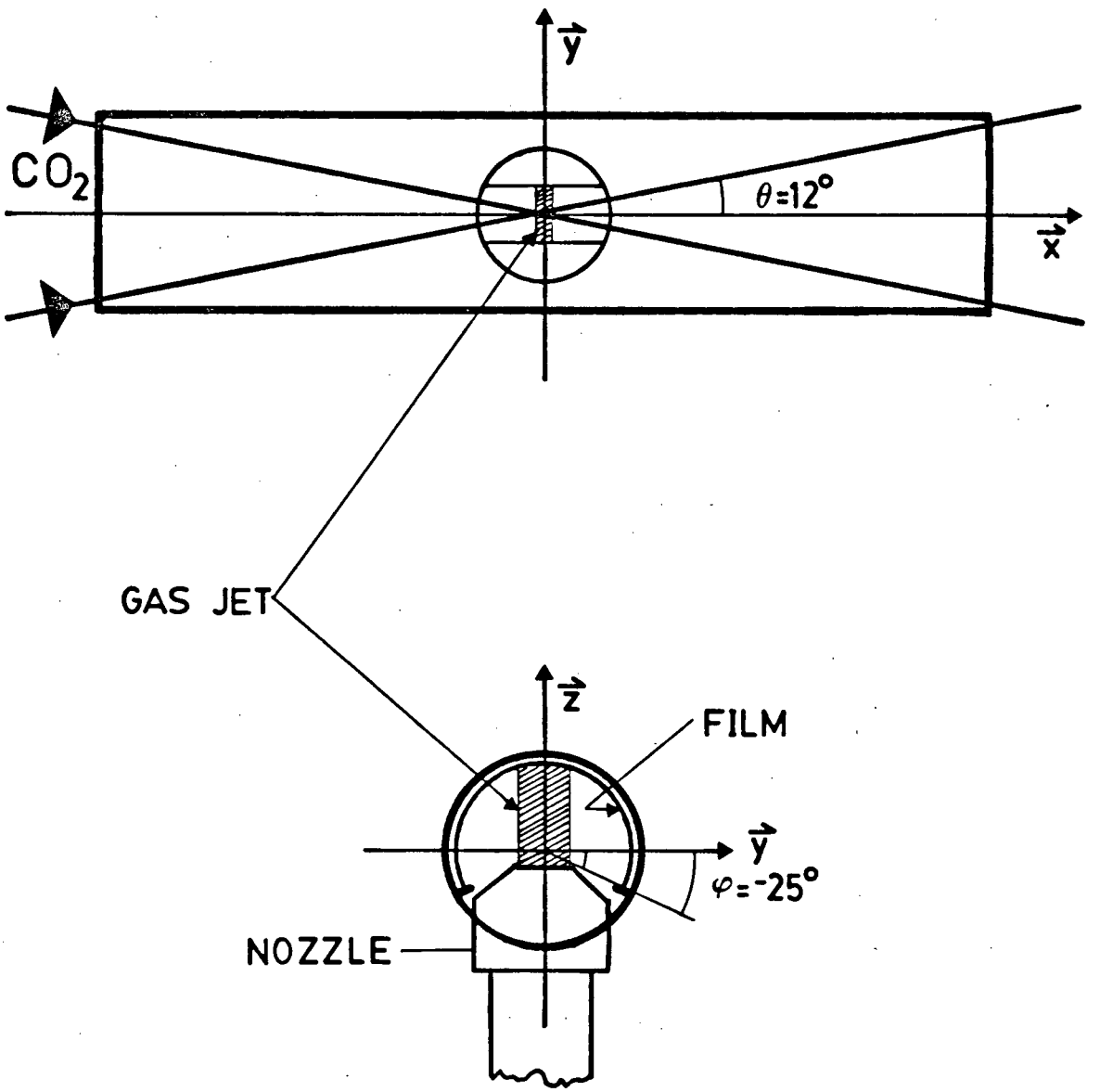

Figure 3.10 — The film holder.

1.65, respectively. Consequently electrons with energies greater than 77 keV are capable of penetrating 7 mg/cm^2 foil and exposing the film while electrons with lower energies expose the film indirectly by means of the bremsstrahlung and aluminum K x-rays produced in the foil.

The main mechanism by which the film is exposed is ionization of the silver salts by the hot electrons themselves. Figure 3.11 shows the film density measured for shots with step-like variations in foil thickness. For an increase in foil thickness, film density decreases as fewer electrons have the energy required to penetrate the thicker foil. Figure 3.12 shows the continuous energy spectrum obtained by replacing the scintillators in the spectrometer with film. While the dependence of film density on the number of electrons striking the film is known to be linear, Figure 3.13 shows the dependence of film density on electron energy.[49] The solid line in Figure 3.12 indicates the density spectrum obtained while the dashed line indicates the absolute density spectrum allowing for this dependence on electron energy. The sharp drop in density for energies less than 77 keV shows that the film is more sensitive to electrons than to x-rays. Since the majority of the hot electrons have energies greater than 77 keV and since the film has a greater sensitivity to electrons than to x-rays, the majority of any exposure of the film is attributed to electrons striking the film.

X-rays originating from the plasma will also expose the film. To investigate this effect film was placed behind the magnetic field of the spectrometer at the same time that the energy spectrum of Figure 3.12 was obtained. The resulting film density from these x-rays was several orders of magnitude less than the densities of the energy spectrum and, hence, any effect of x-rays originating from the plasma can be ignored.

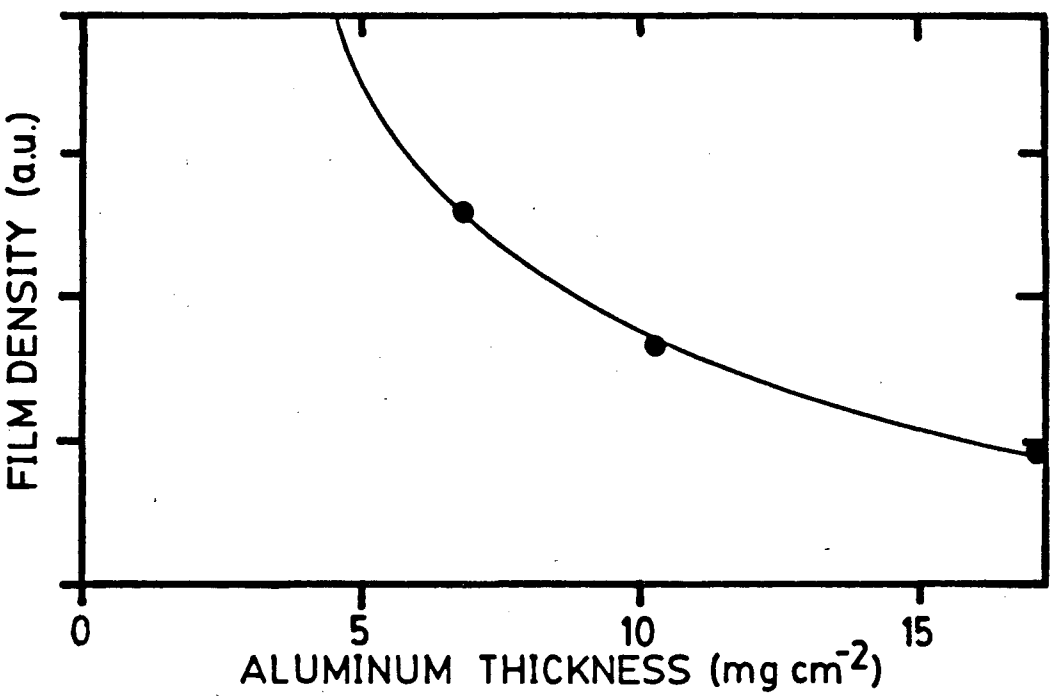

Figure 3.11 — Film density for various foil thicknesses.

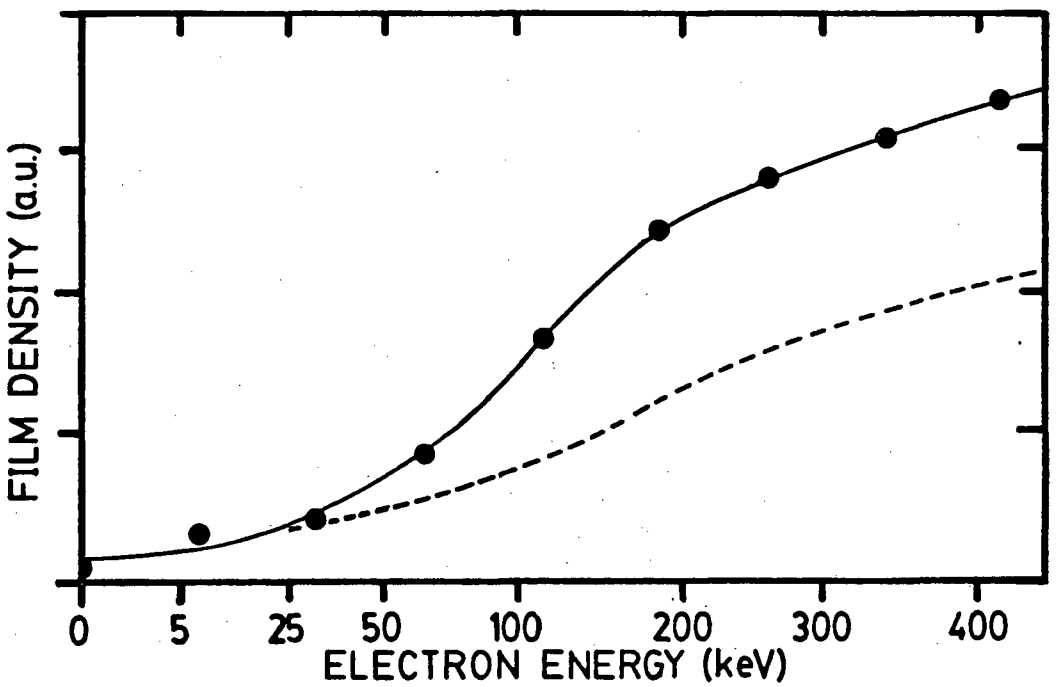

Figure 3.12 — The continuous energy spectrum.

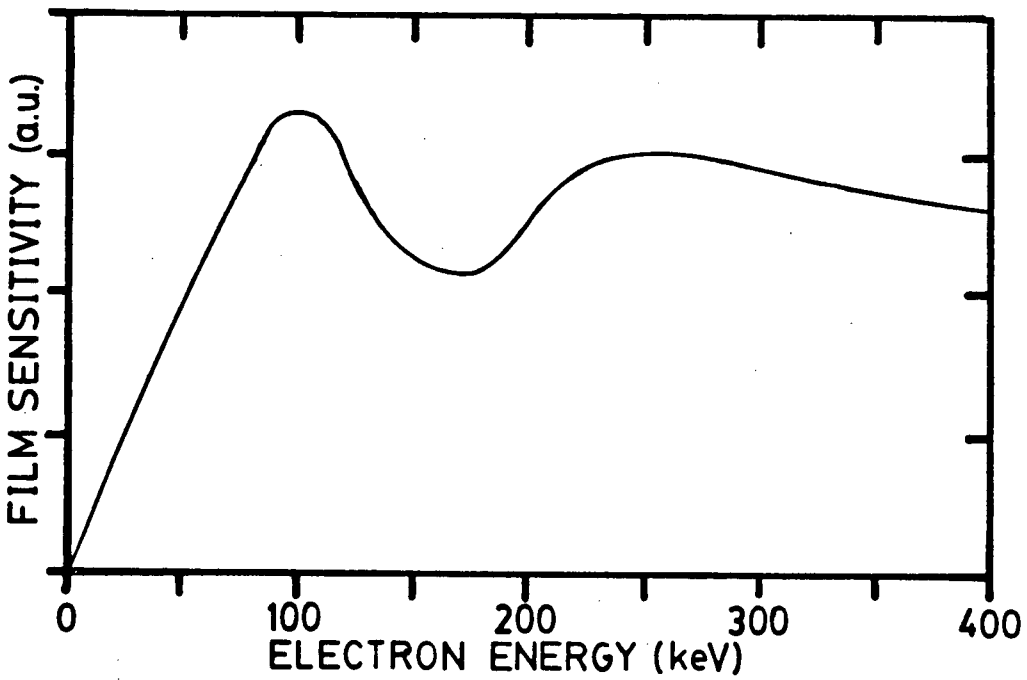

Figure 3.13 — The dependence of film density on electron energy.

CHAPTER IV

THE SPATIAL AND TEMPORAL EVOLUTION OF THE PLASMA

This report examines the hot electrons produced with two different gas jets. The evolution of the nitrogen jet has been well diagnosed and characterized[13,14,37,50] as having a maximum density of $0.4\,n_c < n_e < 0.5\,n_c$, a scale length of $\sim 300\,\mu$m, and a plasma temperature of 300-500 eV. A number of interferograms were taken in order to determine the properties of the helium gas jet.

1. Density Contours and General Features.

Several series of interferograms were taken for different laser energies and with various time delays with respect to the laser pulse. Figure 4.1 shows a typical set of the four frames of interferograms obtained from a single laser shot. As mentioned in §3.3 there is a 95 psec time lag between each frame and the times given are relative to the arrival of the half maximum of the rising edge of the laser pulse.

Figure 4.2 shows a series of ten interferograms with $E_{CO_2} \simeq 6.0\,$J where Figures 4.2a and 4.2b are frames 3 and 4 of one shot while Figures 4.2c through 4.2f and Figures 4.2g through 4.2j are two sets of four frames from two other shots. The

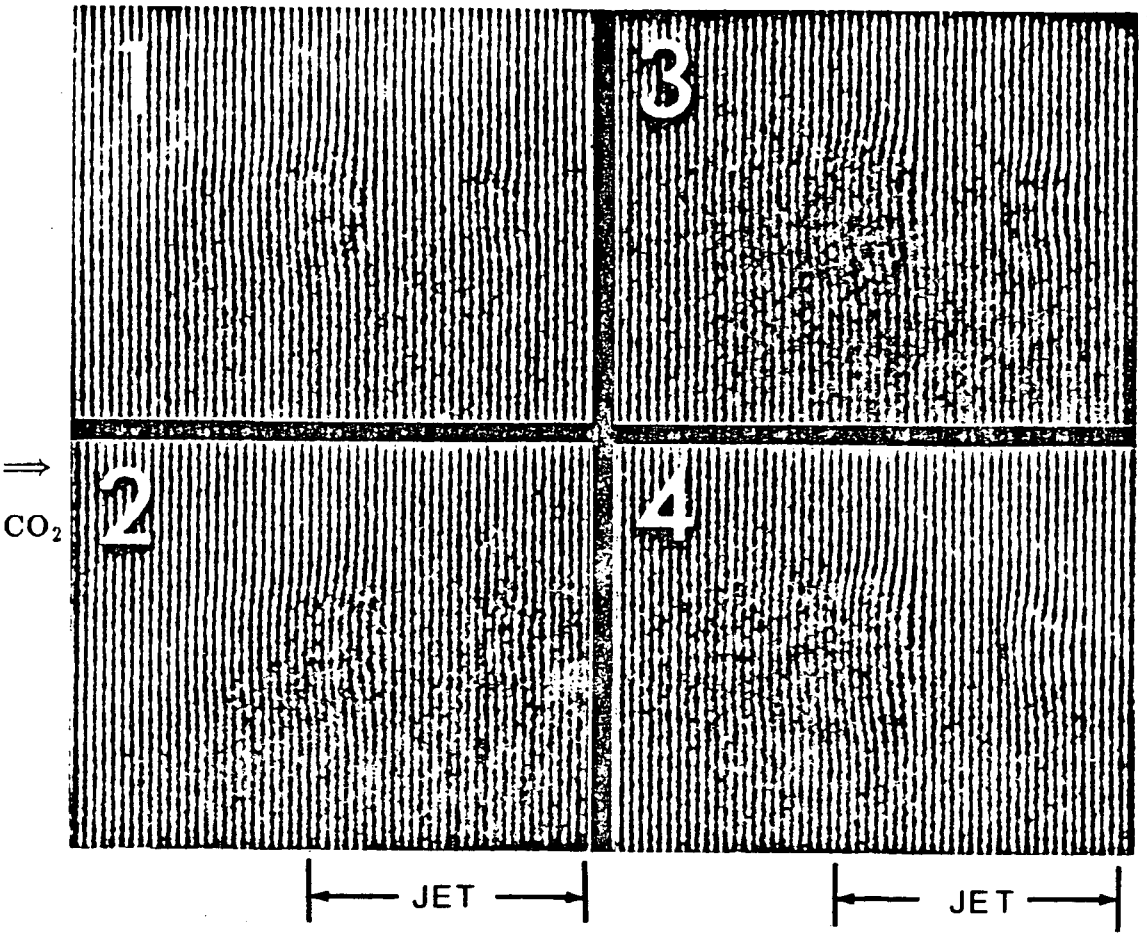

Figure 4.1 — The series of interferograms obtained from a single shot where $E_{CO_2} = 7.25\,\text{J}$, $t_1 = 660\,\text{psec}$.

CO_2 laser is directed from the origin along the z-axis and the solid lines represent density steps of $0.1\,n_c$ while the dashed line is the quarter-critical density boundary.

The earliest observed fringe shifts result in the formation of a plasma island at the front of the jet at $t = 50\,\text{psec}$ as shown in Figure 4.2a. The lack of any fringe shifts in the previous interferogram frame and the correlation between the cross sectional areas of the island and the incident laser beam indicate this is the initial formation of the plasma after $\sim 0.6\,\text{J}$ of temporally integrated energy has been delivered to the target. The island expands and increases in density until $t = 1070\,\text{psec}$ in Figure 4.2g whence the rate of expansion is greater than the

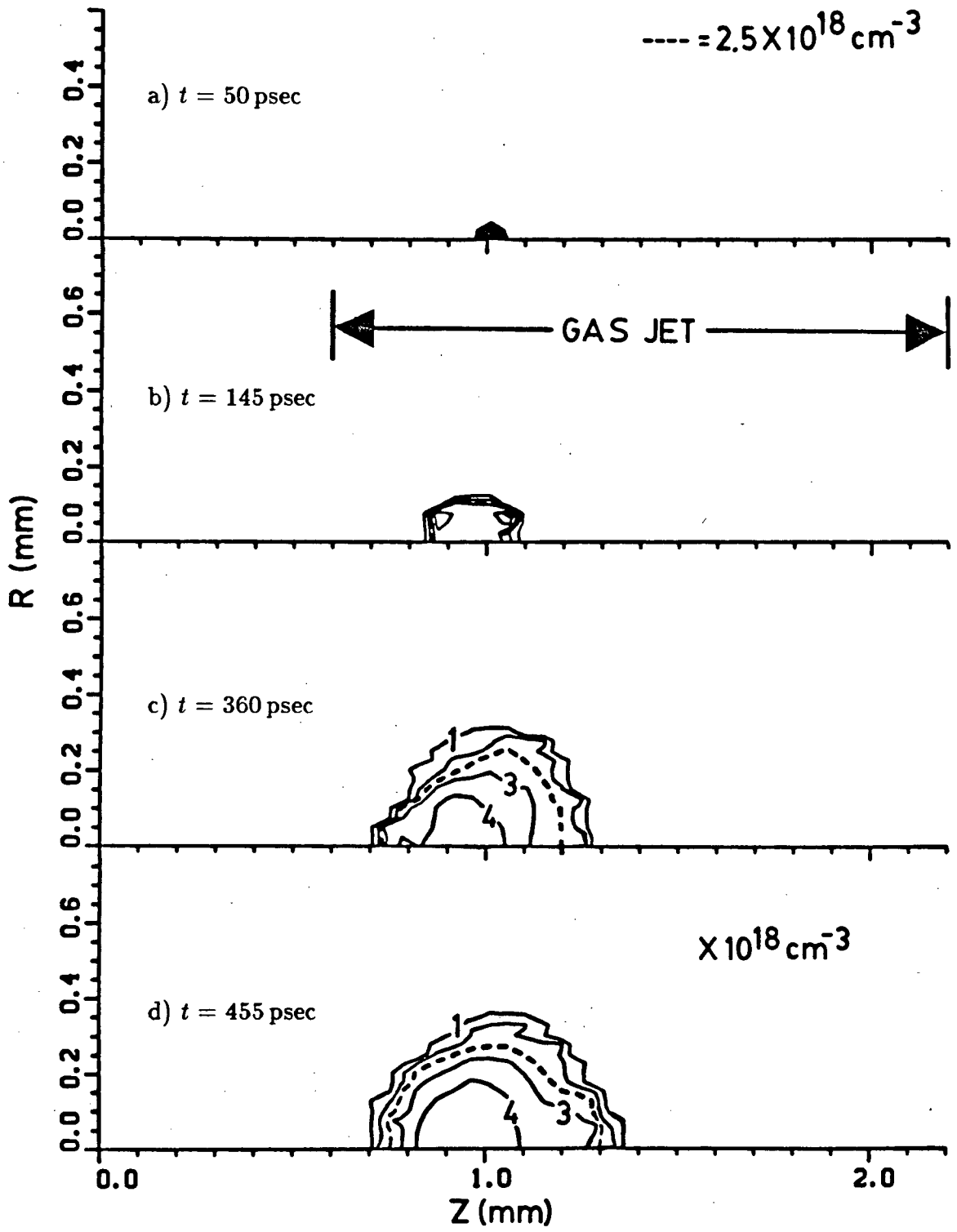

Figure 4.2 — Plasma density contours for $E_{CO_2} \simeq 6.0\,\mathrm{J}$.

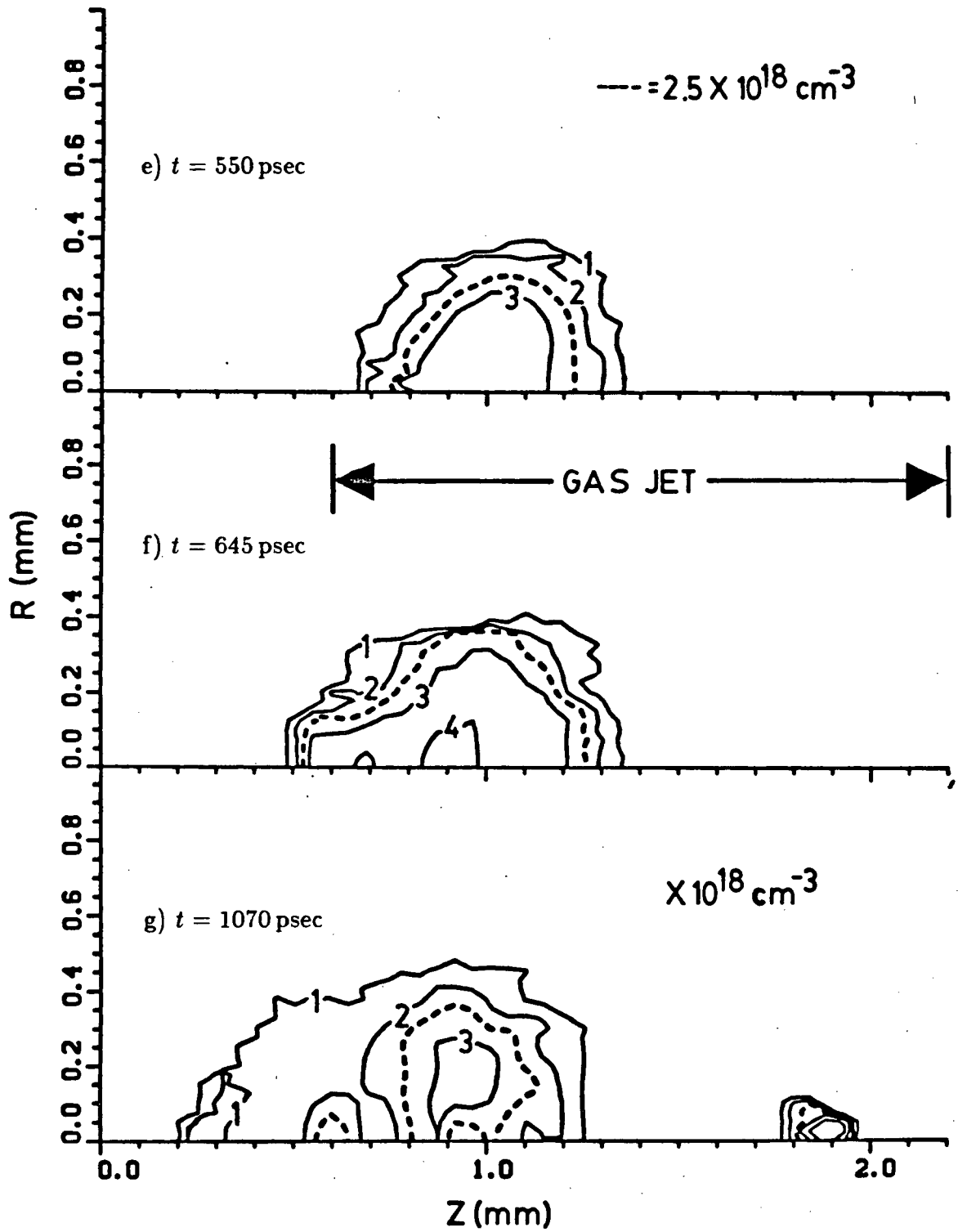

Figure 4.2 — Continued.

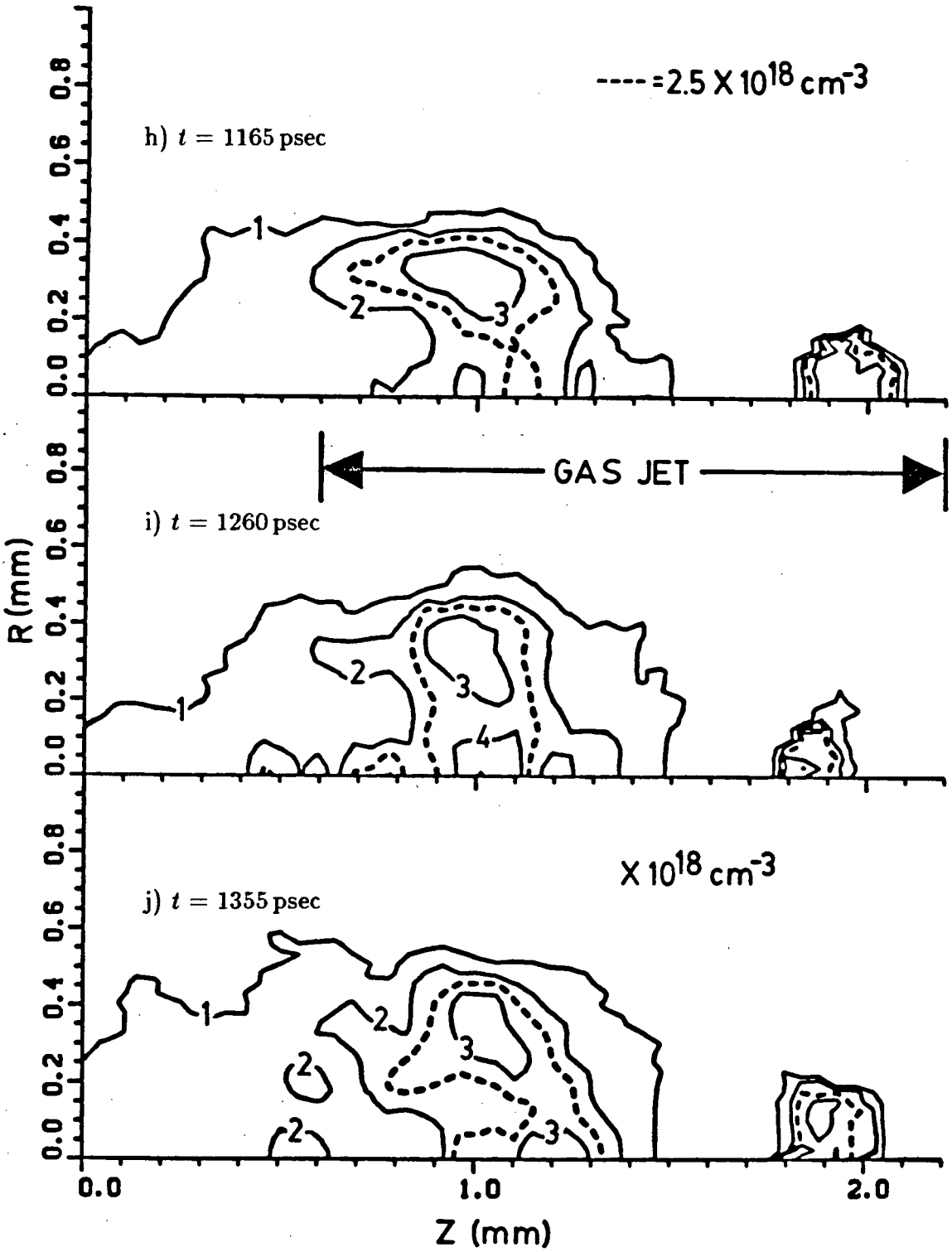

Figure 4.2 — Continued.

density increase. As a result, the density profile assumes a doughnut like shape where the greatest densities lie off the central axis of the laser beam. This high density profile typifies shock wave formation described by blast wave theory with heat transfer.[37,51] Also evident in Figure 4.2g is the emergence of a second island near the rear of the jet. The late emergence of this island is attributed to refraction, reflection, and absorption of the early part of the pulse by the front island.[13] This prevents the build up of sufficient energy to break down the plasma at the center of the jet until this later time.

In the preceding paragraph it was stated that a second island emerged at a later time relative to the first island. Since Figures 4.2f and 4.2g are frames from two different shots it may be argued that this second island did not emerge late but rather it is present at all times for some shots and is absent in other shots even at later times. Figure 4.3 refutes this argument showing four frames of a single shot where the second island is absent in the first frame then emerges and grows in the last three frames.

Figure 4.4 outlines the evolution of the plasma through the later stages of the 2 nsec CO_2 pulse for energies of $\sim$ 7.75 J. Figures 4.4a through 4.4d and 4.4e through 4.4h are two sets of four frames from two separate shots while Figures 4.4i and 4.4j are frames 1 and 3 of a single shot and Figures 4.4k and 4.4l are frames 2 and 4 of still another shot.

Figure 4.4a shows that the second island near the rear of the jet forms much earlier compared to its emergence in Figure 4.2g simply because there is more energy available at t = 660 psec from a 7.75 J shot than a 6.0 J shot. Both the front and rear islands then expand and increase in density until they assume the same doughnut like shape exhibited in Figure 4.2. At later times ($>\sim$ 1400 psec) the majority of the energy from the laser pulse has been delivered to the target and the main features of the denser regions of the plasma remain relatively unchanged. However, diffusive effects greatly affect the lower density regions as the 0.1 n_c boundary of the

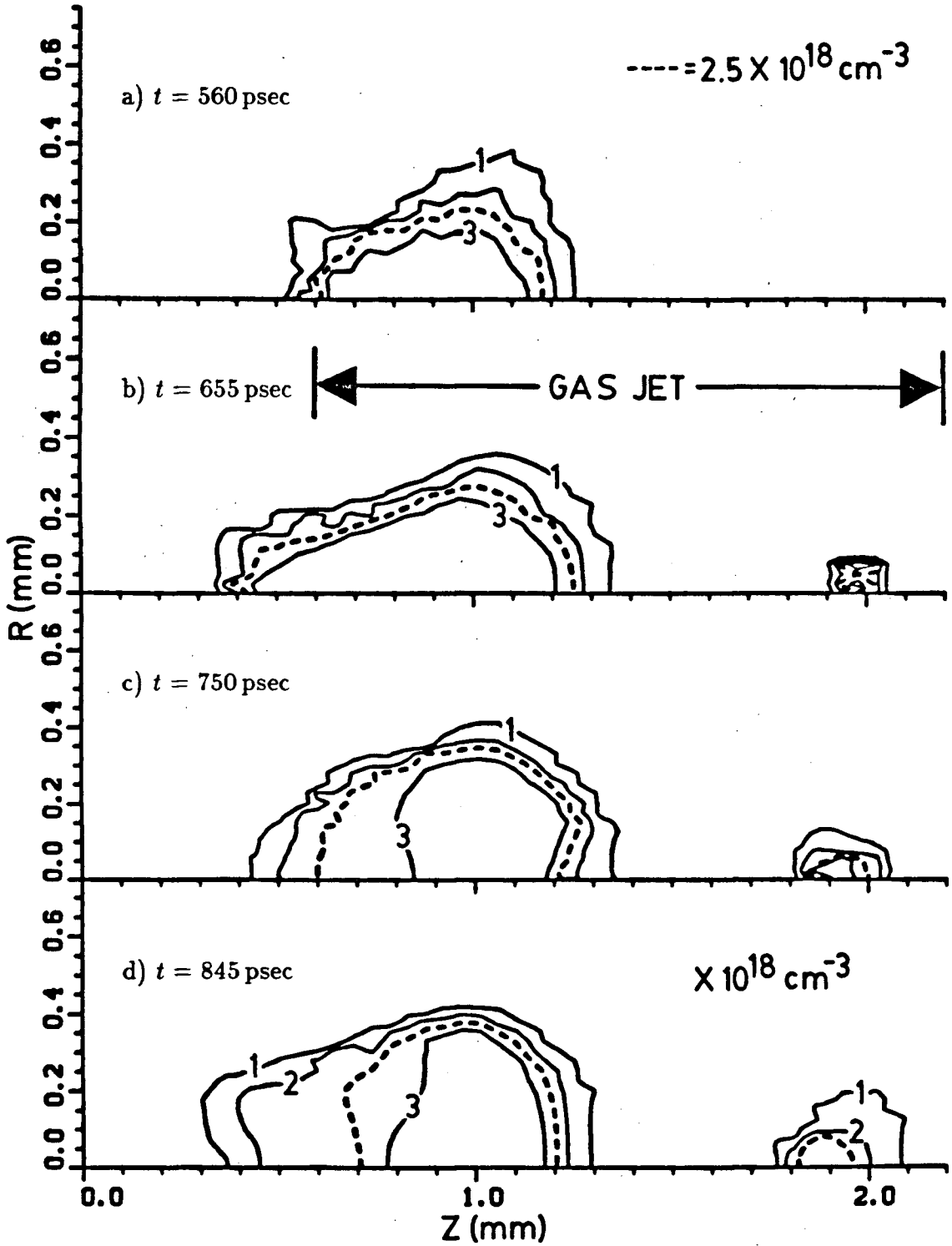

Figure 4.3 — Plasma density contours showing the late emergence of a second plasma island for $E_{CO_2} = 4.75\,\mathrm{J}$.

two islands merges and expands well beyond the region of the jet. This expansion is especially noticable at the front of the jet in Figures 4.4i through 4.4l.

2. Plasma Density Distribution.

The study of TPD requires the presence of densities above $0.25\,n_c$. Considerations in §3.2 showed that, without allowing for expansion of the plasma, densities up to $0.537\,n_c$ could be achieved with the helium jet in an 8 torr background. The dashed line representing the $0.25\,n_c$ boundary is clearly evident for all the density contours throughout Figures 4.2, 4.3 and 4.4, thus ensuring the proper initial condition for TPD is met.

Figures 4.5a and 4.6a show the total number of free electrons and the number of electrons enclosed by the quarter critical boundary for the two series of density contours shown in Figures 4.2 and 4.4. Clearly evident is that, while the total number of electrons increases linearly over the time intervals shown, the number of electrons bounded by the quarter critical boundary reaches a maximum value at $t >\sim 0.6$ nsec in Figure 4.5a ($E_{CO_2} = 6.0$ J) and at $t >\sim 1.0$ nsec in Figure 4.6a ($E_{CO_2} = 7.75$ J).

Figures 4.5b and 4.6b show the volume enclosed by the $0.1\,n_c$ and $0.25\,n_c$ boundaries for the two series. The two volumes in Figure 4.5b are expanding at rates of 1.1 m^3/sec and 0.16 m^3/sec for the $0.1\,n_c$ and $0.25\,n_c$ boundaries, respectively. For the higher energies the boundaries expand at rates of 1.7 m^3/sec and 0.52 m^3/sec. The fact that the number of electrons enclosed by the quarter critical boundary is constant at later times indicates a shift in the electron density distribution. Indeed this is evident in Figure 4.7 which shows a series of historgrams for the 7.75 J series and a shift in the distribution from higher to lower densities.

3. Scale Lengths and Radial Expansion Rates.

The scale length L is easily derived from (2–20) and the density contours of §4.1. Figure 4.8, which shows the scale length determined along the quarter

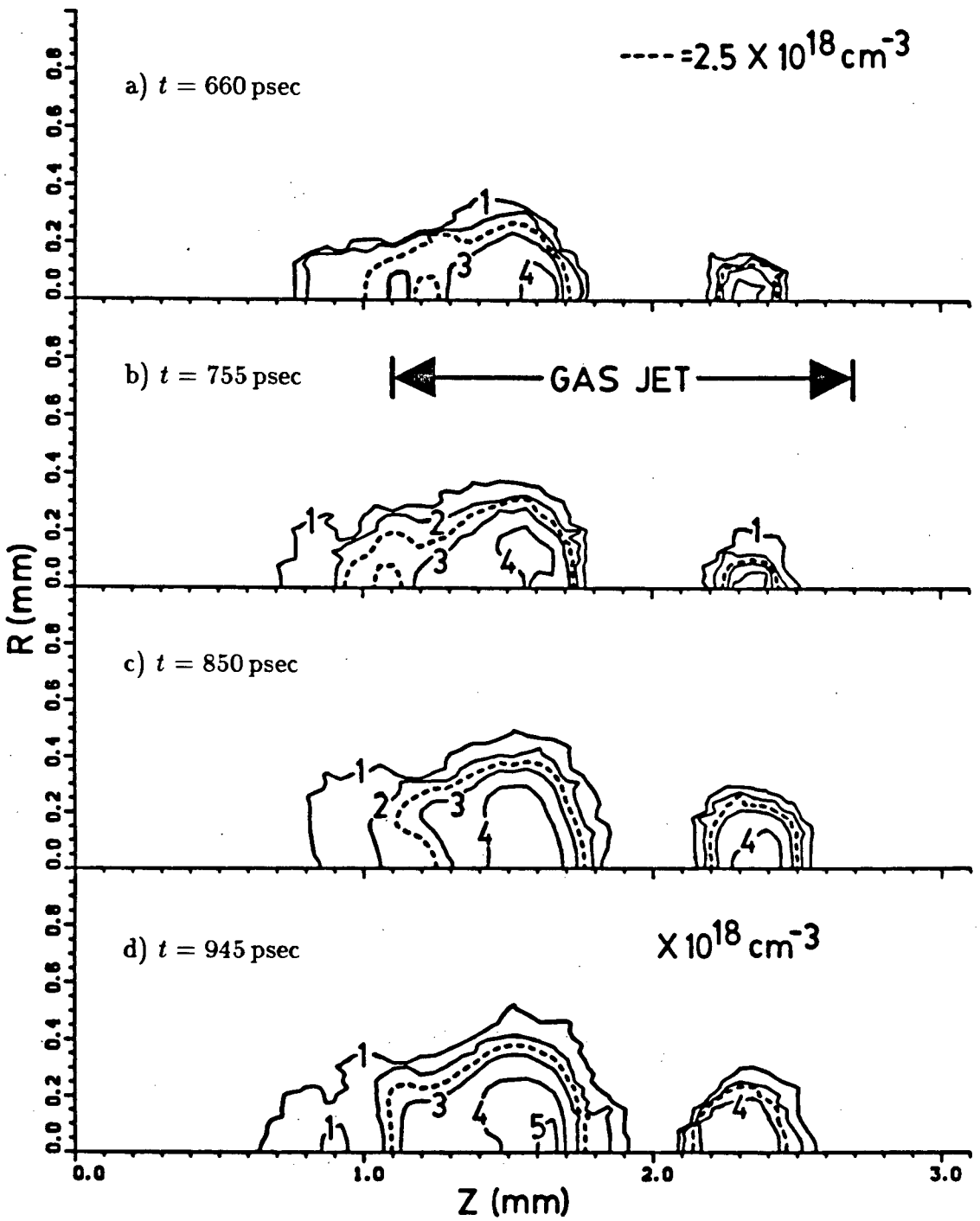

Figure 4.4 — Plasma density contours for $E_{CO_2} \simeq 7.75\,\mathrm{J}$.

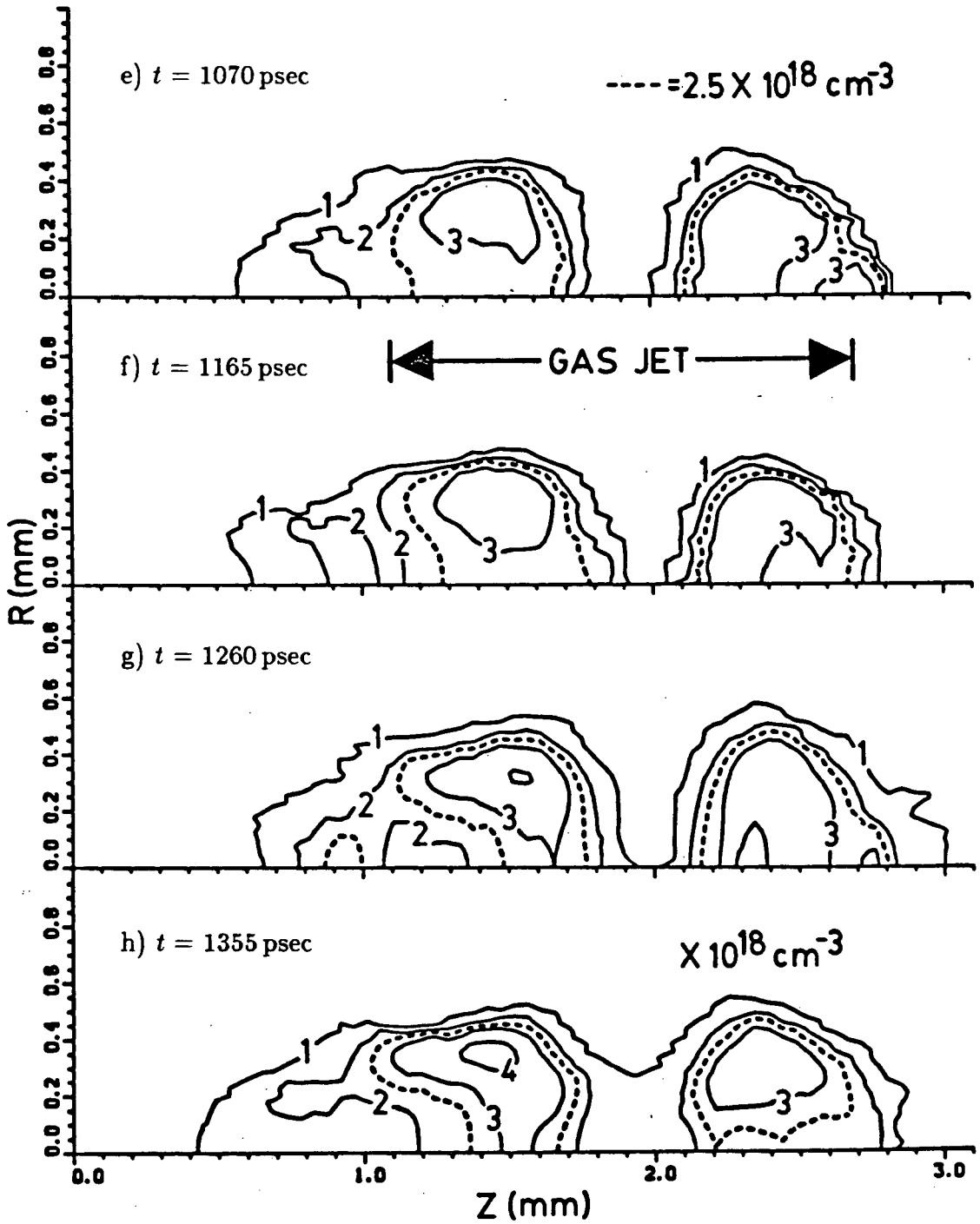

Figure 4.4 — Continued.

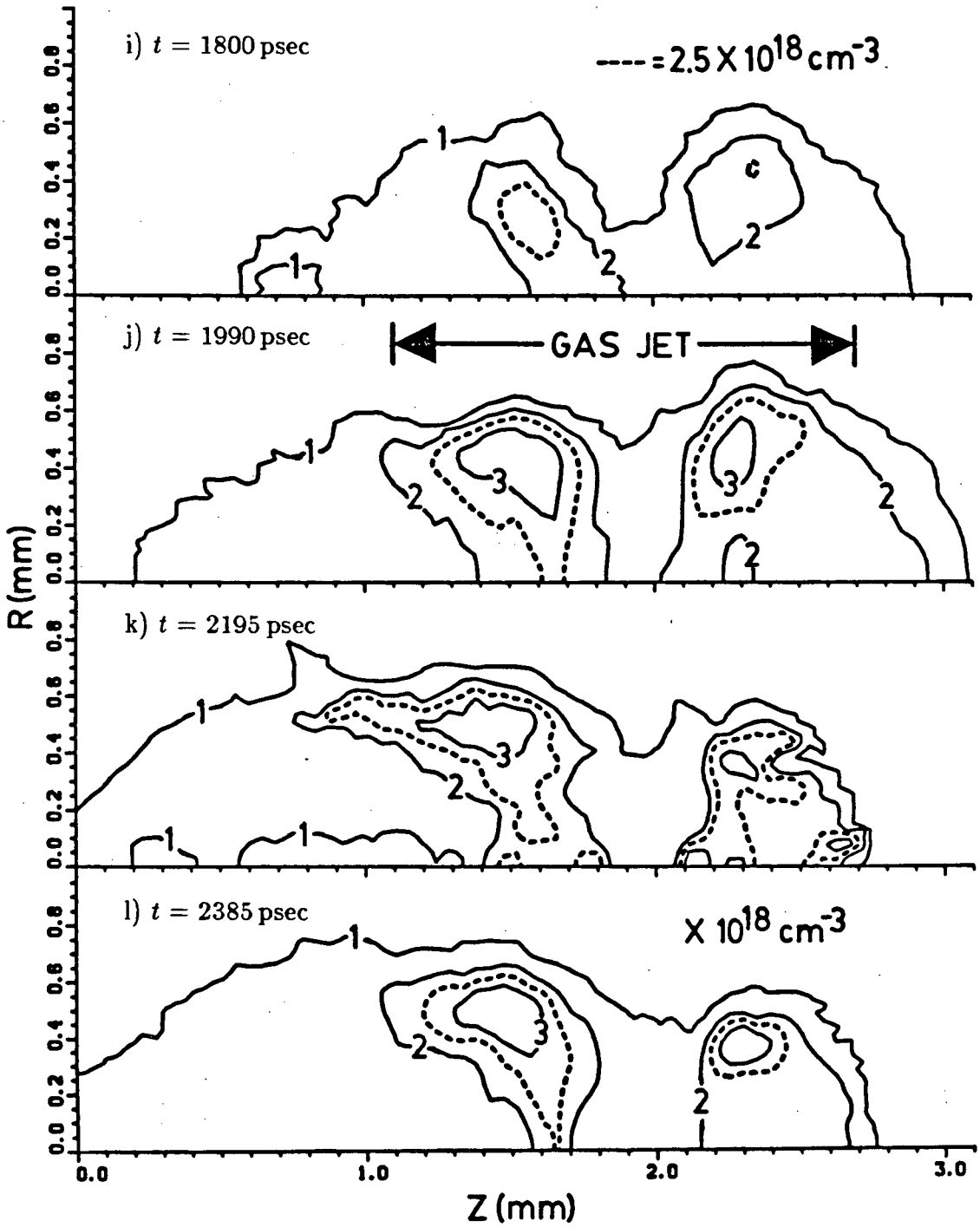

Figure 4.4 — Continued.

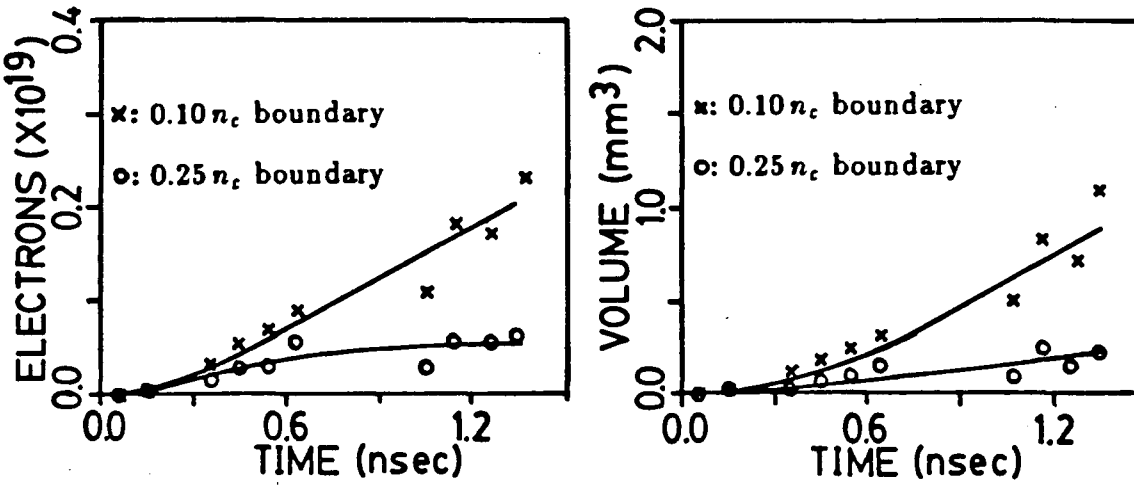

Figure 4.5 — The number of electrons and the volume of a 6.0 J plasma.

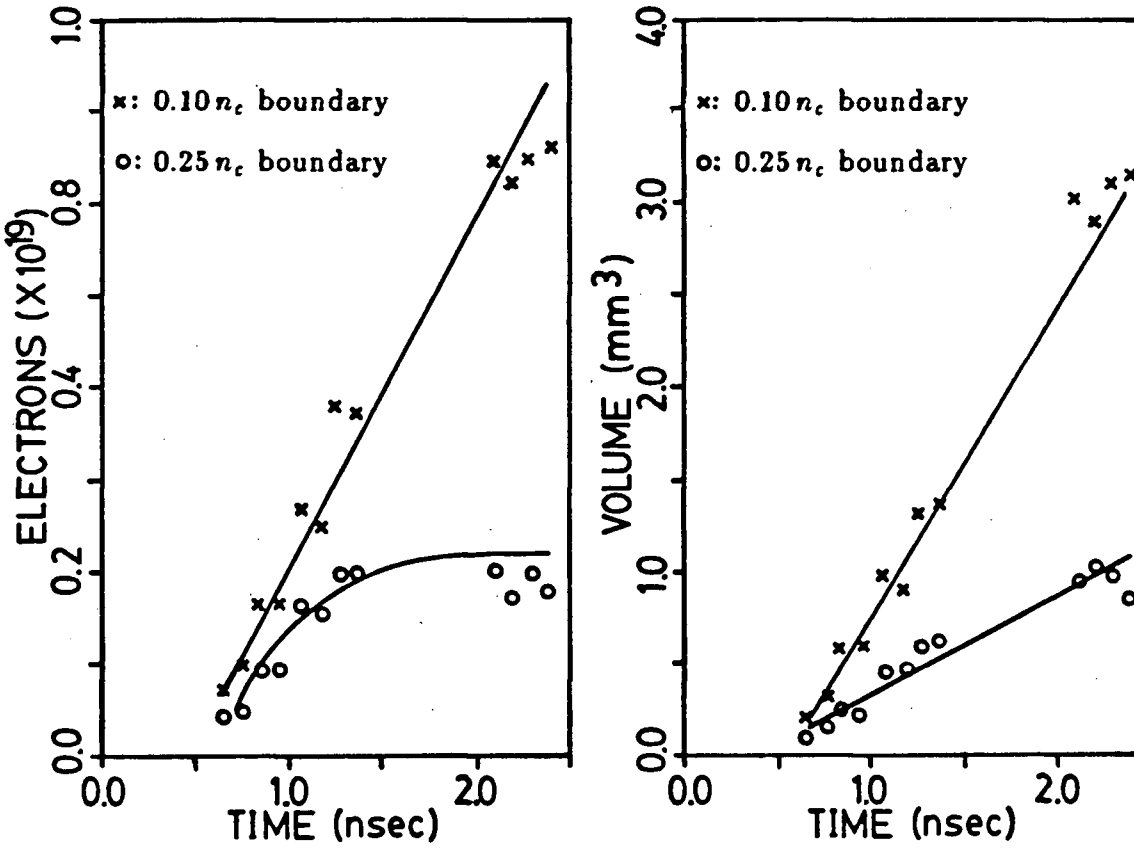

Figure 4.6 — The number of electrons and the volume of a 7.75 J plasma.

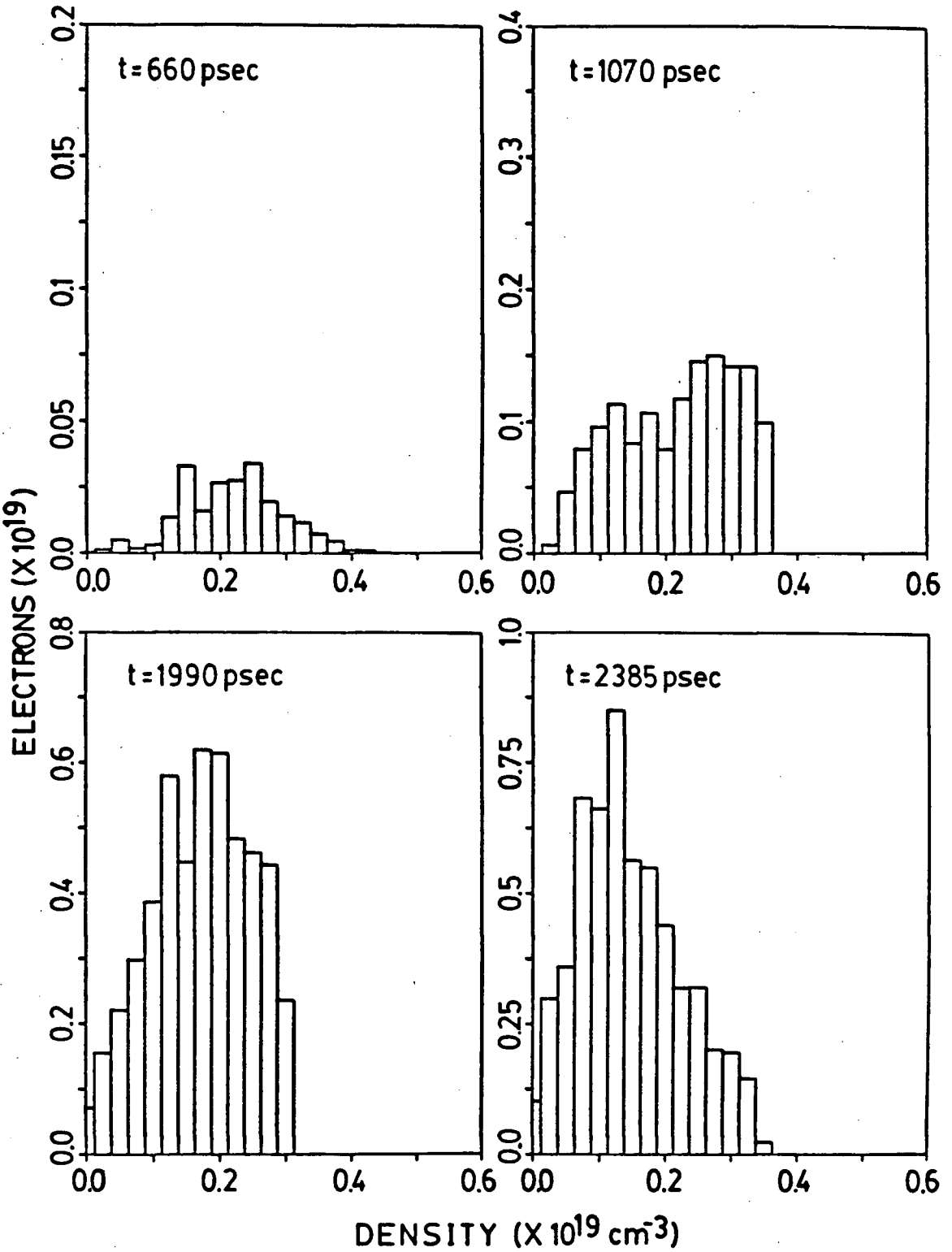

Figure 4.7 — The electron density distribution for a 7.75 J plasma.

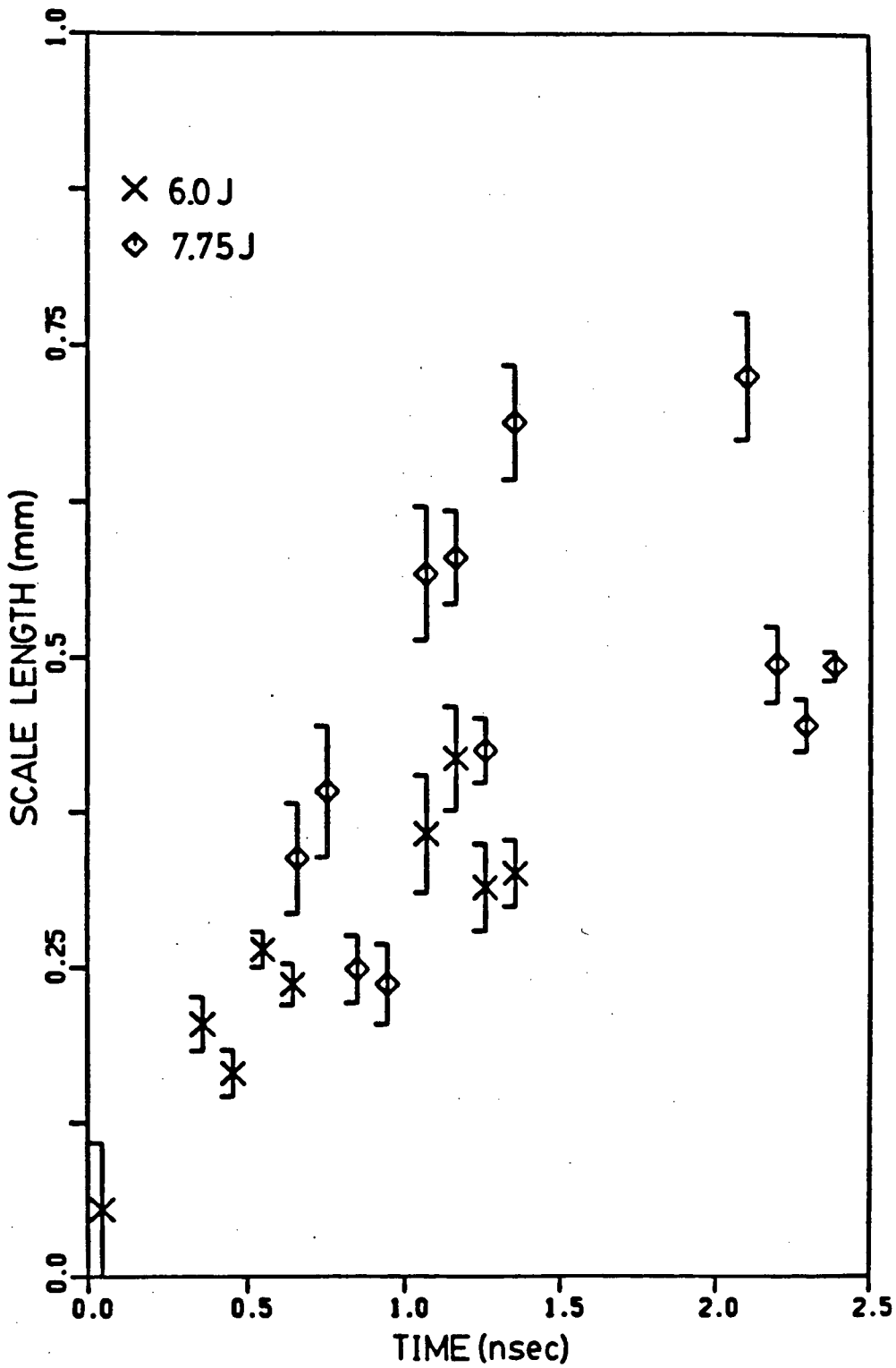

Figure 4.8 — Scale lengths at the quarter critical boundary.

density boundaries from both series of contours in Figures 4.2 and 4.4 with the error bars representing one standard deviation of the values derived along the boundary. Indicated here is the variance in scale length over the lifetime of the laser pulse, from $< \sim 50\,\mu$m up to $\sim 750\,\mu$m.

For a cylindrically symmetric plasma it is more appropriate to refer to radial expansions rather than the volume expansion of the previous section. Figure 4.9 shows the expansion rate of the quarter critical boundary in the front island of the two series of contours. This boundary approaches a constant expansion rate of 1.9×10^6 m/sec for times greater than $\sim$525 and $\sim$900 psec for the 6.0 and 7.75 J plasmas, respectively.

4. The Laser Plasma Interaction Region.

Sections 4.2 and 4.3 discuss the properties of the plasma as a whole. However, despite the scattering effects of the cross-sectional area of the laser beam by the plasma, the effect of plasma expansion carries the bulk of the plasma outside the laser plasma interaction region. Hence, the volume of the plasma along the central axis requires a closer inspection.

Figure 4.10 shows the density profile of the plasma along the central axis for a single laser plama interaction with $t = 1070$ psec to $t = 1355$ psec and $E_{CO_2} = 6.0$ J. Of special interest here is the effect of profile steepening evident in Figures 4.10b through 4.10d. The relatively gentle density gradient across the front island of Figure 4.10b changes dramatically as the density increases past the $0.25\,n_c$ level in Figure 4.10c until Figure 4.10d where the density gradient has attained a much steeper profile. Also evident in Figure 4.10a are the presence of peaks and valleys showing that the plasma density does not increase uniformly along the axis.

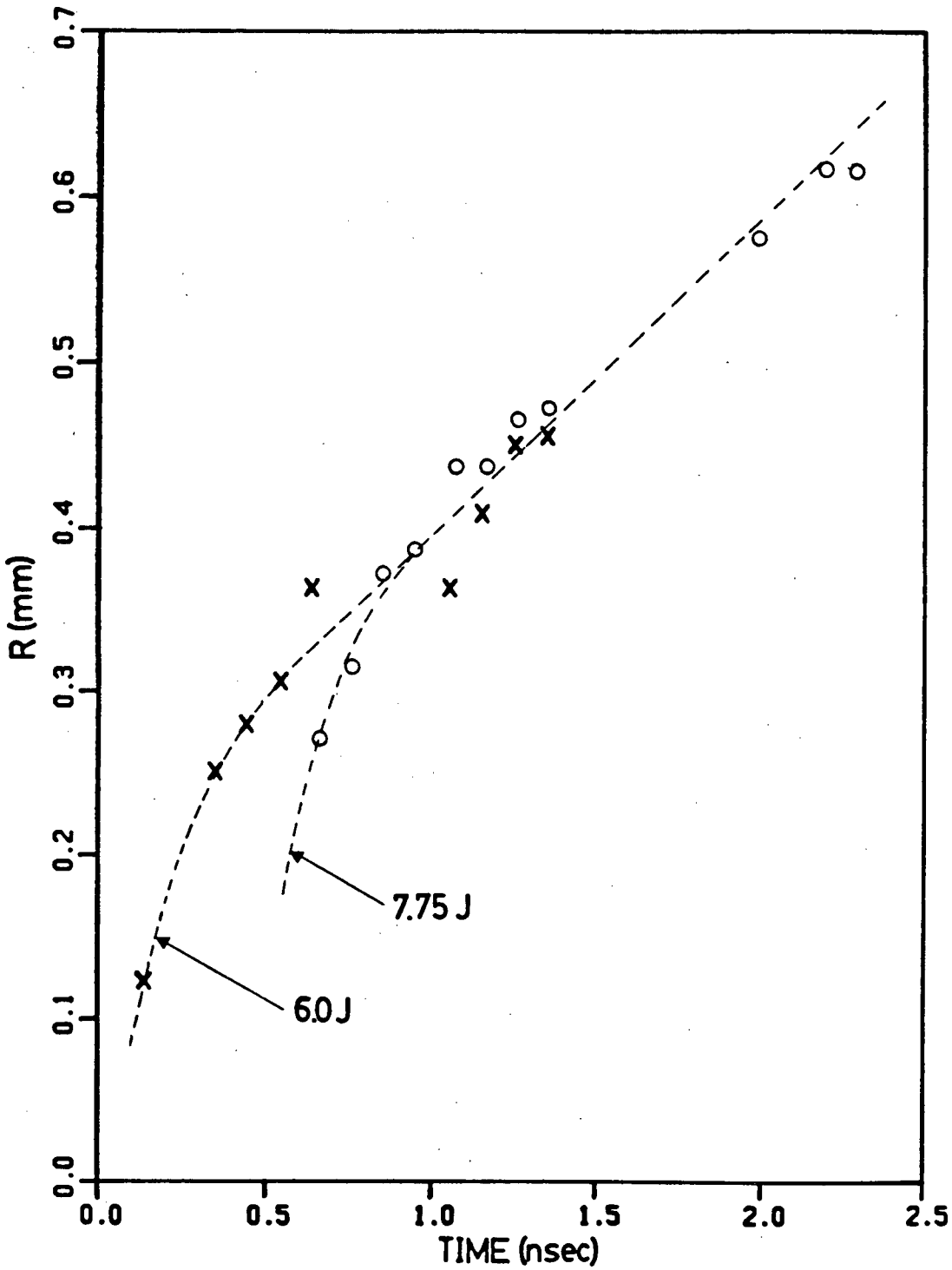

Figure 4.9 — Expansion of the quarter critical boundary.

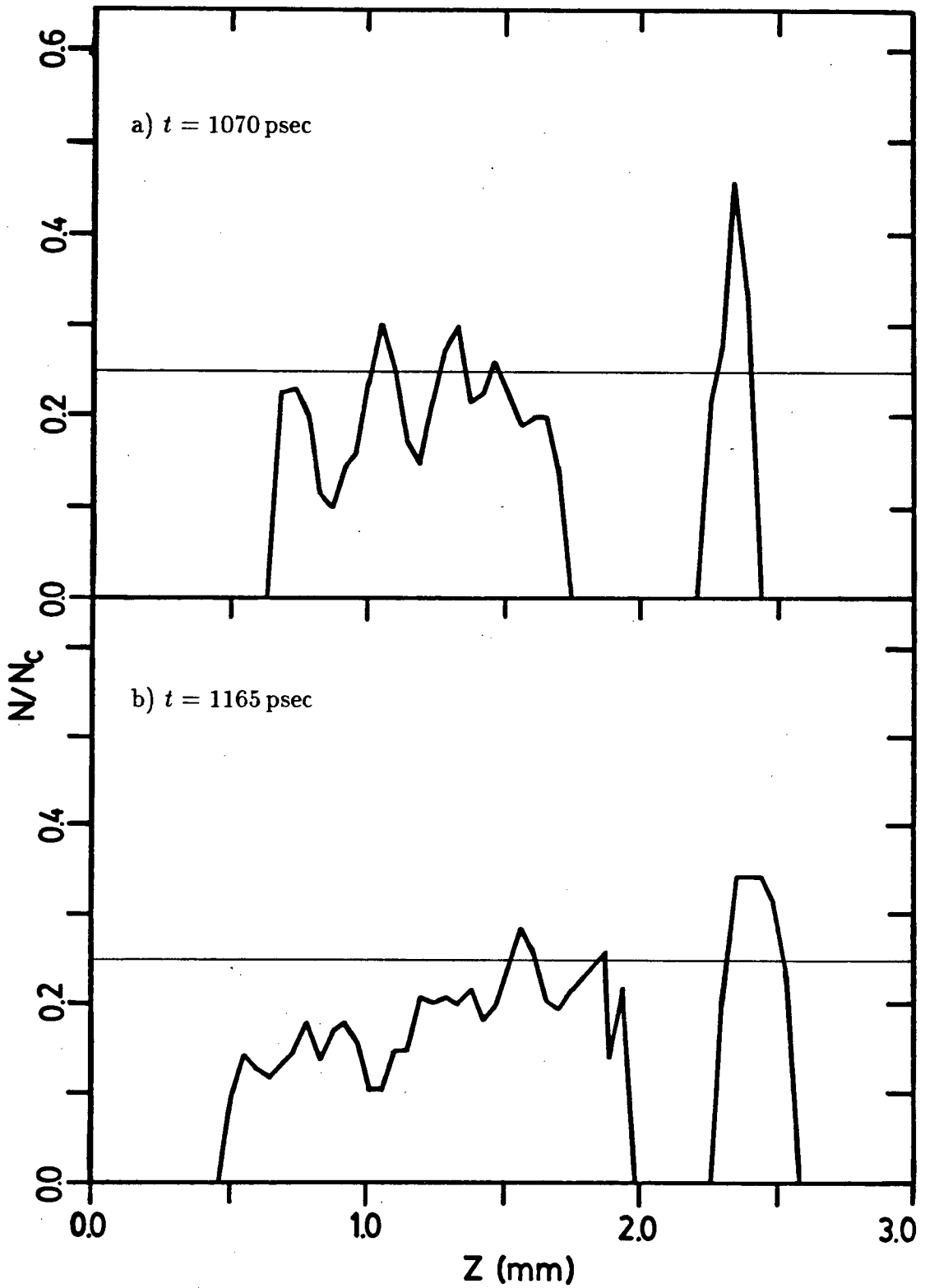

Figure 4.10 — Density profiles along the central axis of the plasma for $E_{CO_2} = 6.0$ J.

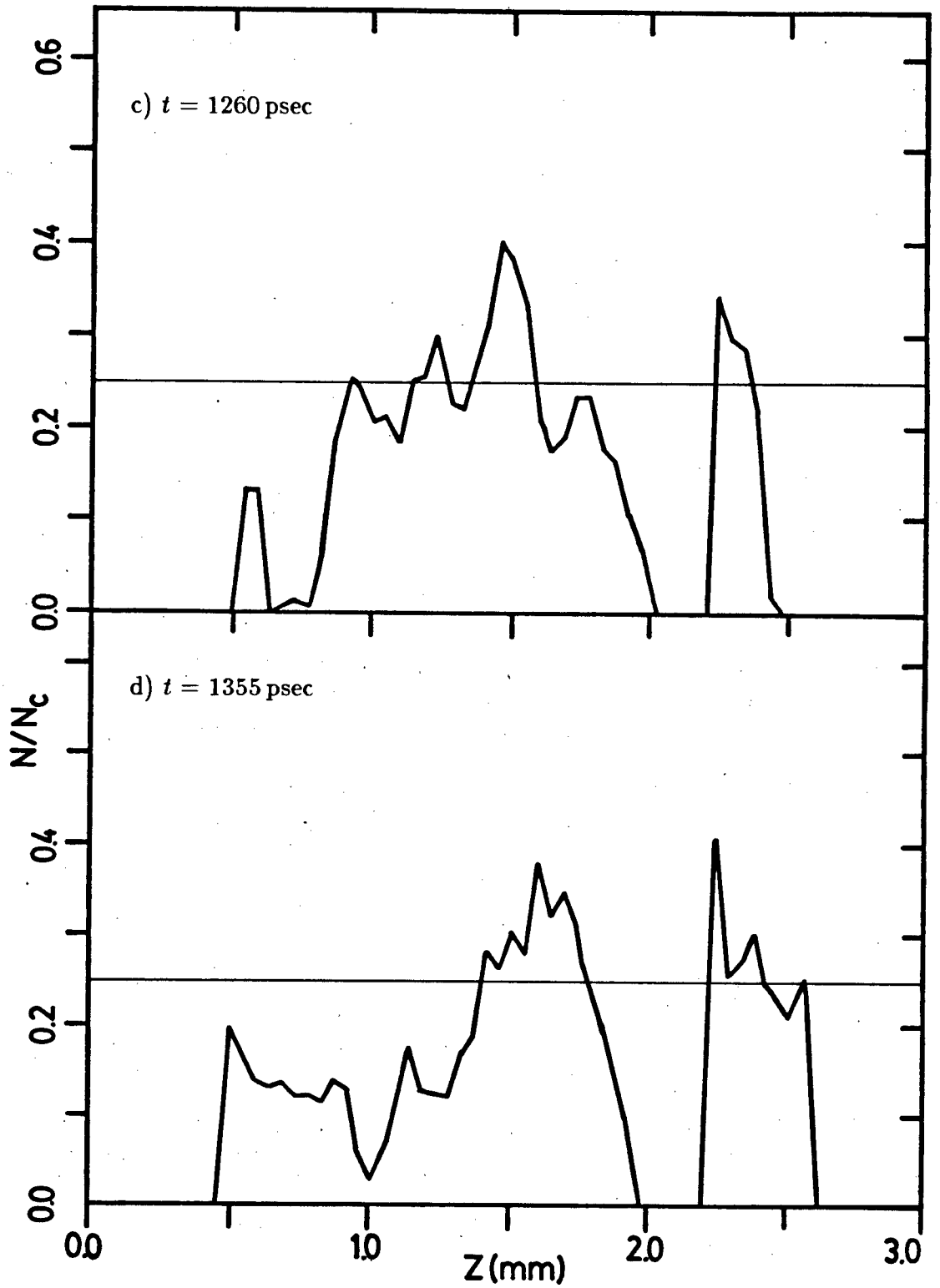

Figure 4.10 — Continued.

CHAPTER V

THE ELECTRONS PRODUCED BY THE TPD INSTABILITY

As discussed in Chapter 1, the main objective of this thesis is to study the electrons generated by the TPD instability; to examine the three dimensional spatial distribution of these electrons and to determine their energy distribution. Photographic film, as discussed in §3.4b, was used to study the spatial distribution while the electron spectrometer of §3.4a was used to determine the energy distribution.

1. The Electron Images.

The film holder of §3.4b was oriented over the gas jet as shown in Figure 5.1 where the wave vector of the incident laser beam is directed along the x-axis ($\hat{k}_o = \hat{x}$) and the beam is polarized in the xy-plane ($\hat{E}_{CO_2} = \hat{y}$). As discussed in §2.3, the TPD-produced EPW's will accelerate electrons along the direction of the wave vectors of the EPW's. Hence, the areas of the film exposed by the electrons can be related to the wave vectors of the EPW's which, as discussed in Chapter VI, can be compared to the theory of §2.2.

The direction of the wave vectors of a particular wave vector $\vec{k}_s$ can be conveniently expressed in terms of two angles θ and φ. φ is the angle between $\vec{k}_s$ and the

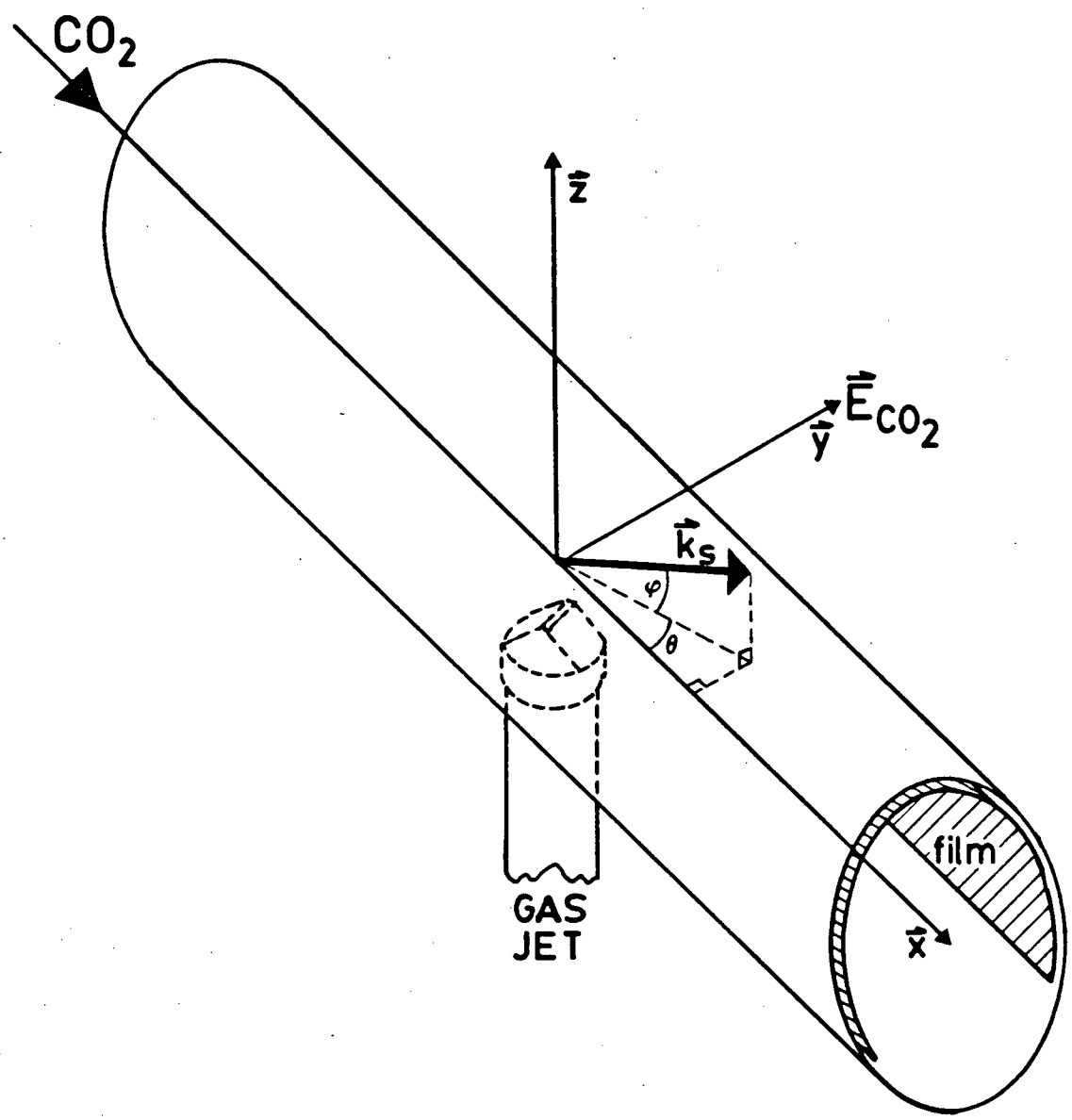

Figure 5.1 — The experimental setup for detection of electrons with photographic film.

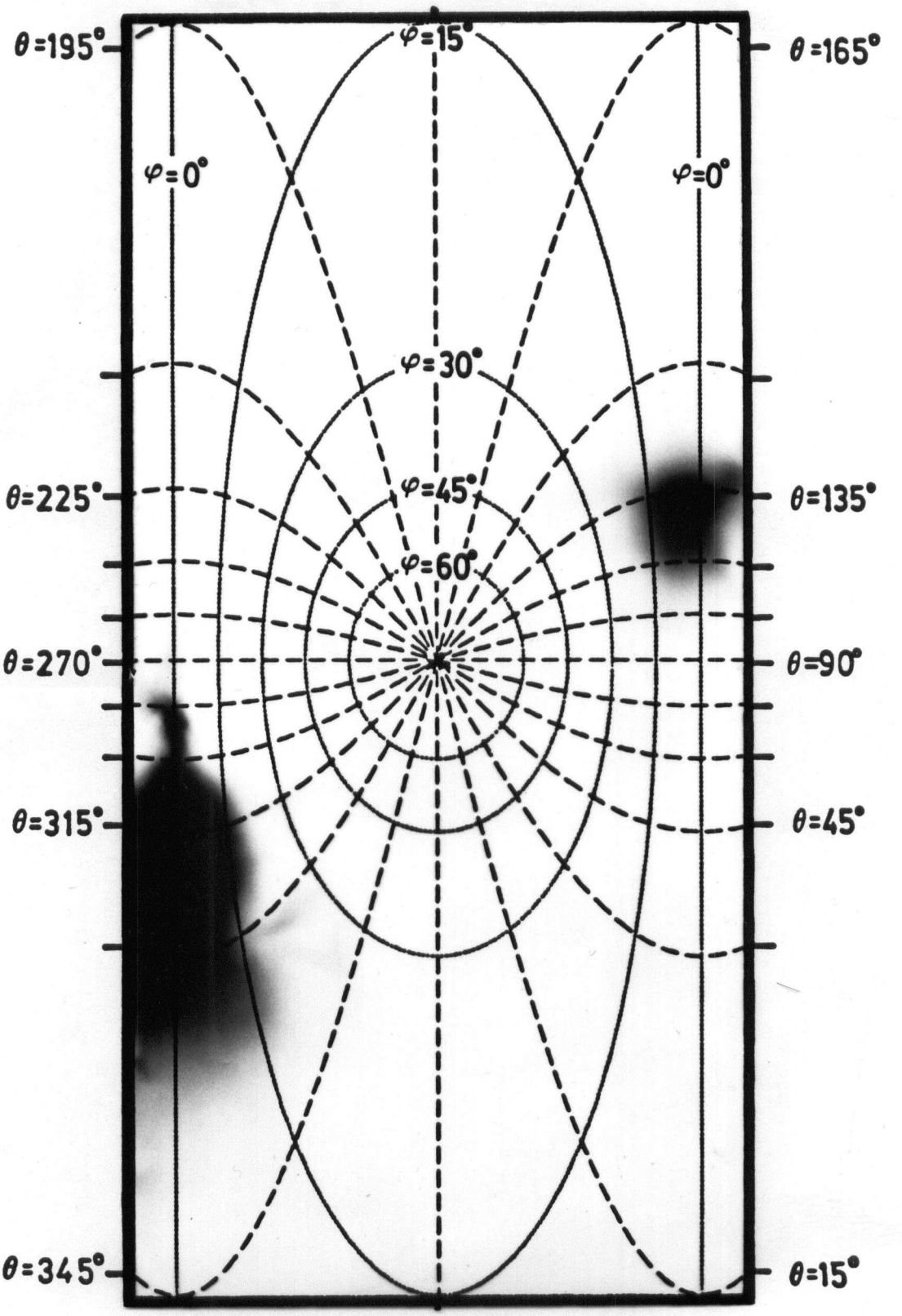

Figure 5.2 — Electron images obtained with a nitrogen target ($E_{CO_2} = 4.5\,\mathrm{J}$).

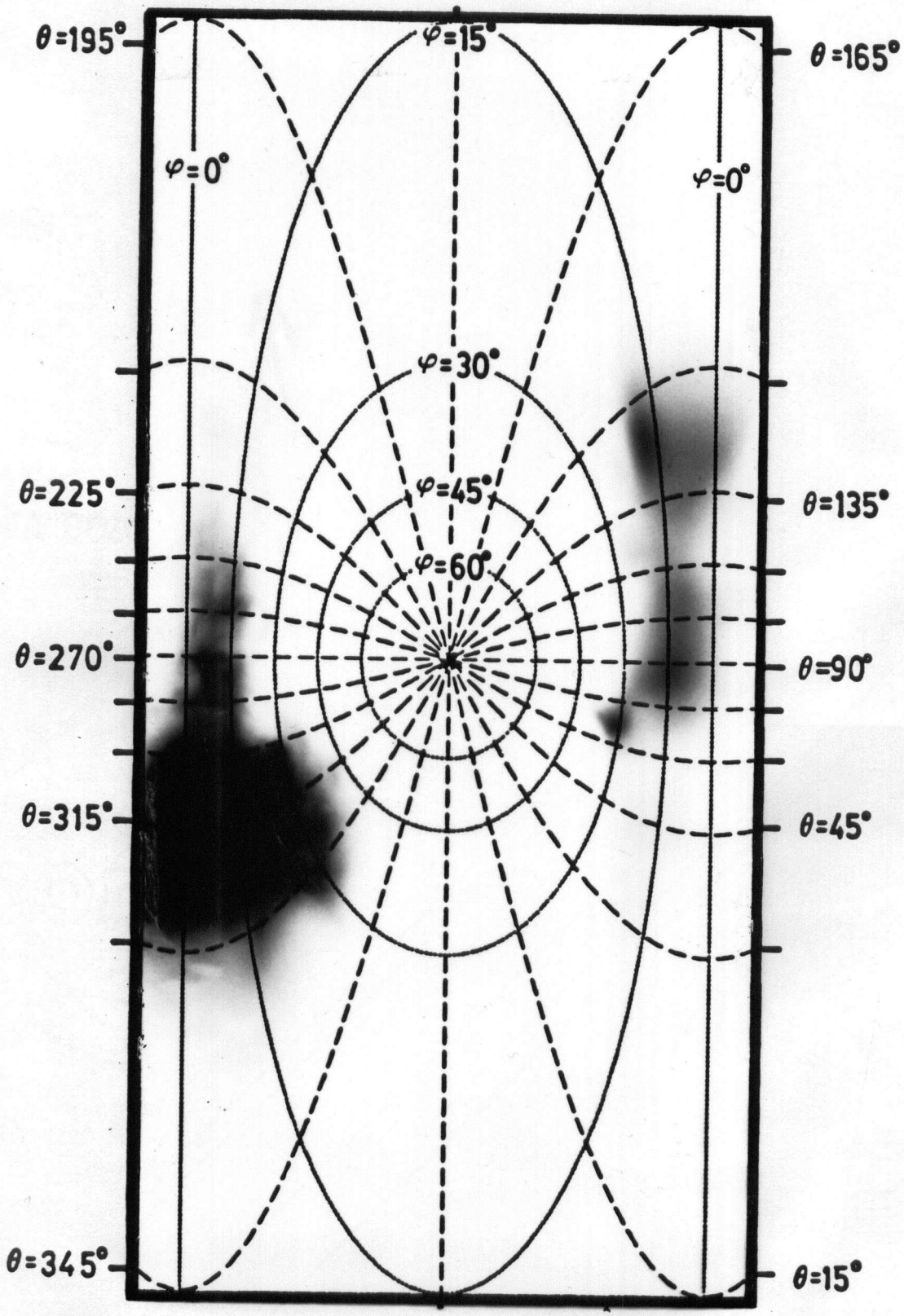

Figure 5.3 — Electron images obtained with a nitrogen target ($E_{CO_2} = 6.0\,\mathrm{J}$).

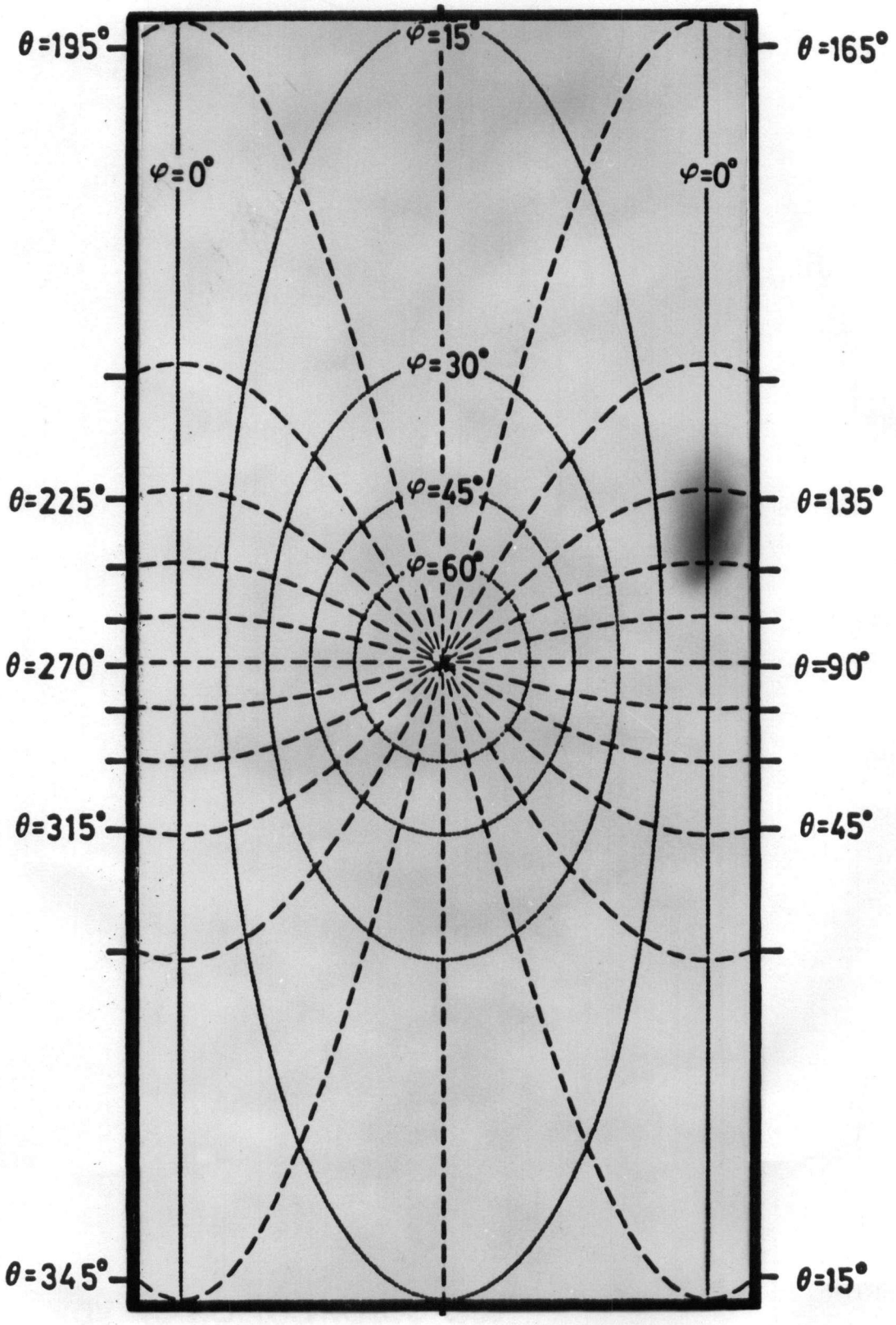

Figure 5.4 — Electron images obtained with a nitrogen target ($E_{CO_2} = 7.0\,\mathrm{J}$).

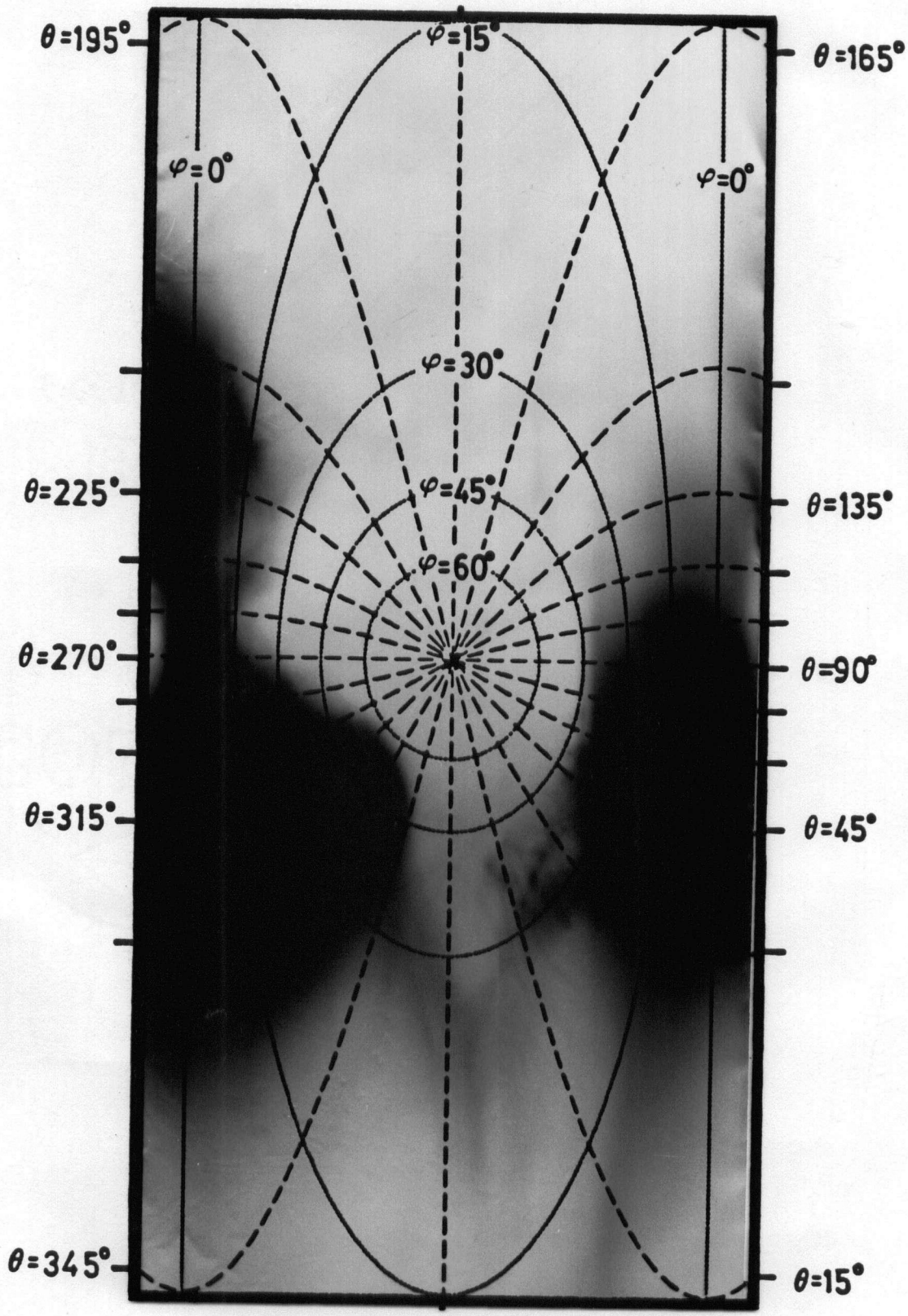

Figure 5.5 — Electron images obtained with a nitrogen target ($E_{CO_2} = 9.0\,\mathrm{J}$).

plane of polarizaration and θ is the angle between $\vec{k}_o$ and the projection of $\vec{k}_s$ onto the plane of polarization. Figure 2.1 can then be used to relate values of θ to the values of k_y/k_o discussed in §2.2. Figures 5.2 through 5.9 show the electron images obtained for eight different laser plasma interactions of varying laser energies, where nitrogen was used as the target gas for the first four figures while helium was used for the remaining four images.

At low energies with the nitrogen jet, the majority of the electron images are concentrated near the plane of polarization at $\theta = 45$, 135, 225, and 315°. However, with higher energies (Figure 5.5, $E_{CO_2} = 9.0\,\mathrm{J}$) electron images were observed above the plane of polarization in the forward scattering direction (as much as $\varphi = 60°$ at $\theta = 315°$). The images recorded with helium as a target gas were similar to those of the nitrogen jet with the exception that electrons were observed above the plane of polarization at lower laser energies. In Figure 5.6, with $E_{CO_2} = 5.0\,\mathrm{J}$, images were recorded in the plane of polarization for $\theta \sim 45$, 135, 215, and 315°. For $E_{CO_2} = 6.0\,\mathrm{J}$ in Figure 5.7, as well as at the higher energies of Figures 5.8 and 5.9, electron images appeared above the plane of polarization in the forward scattering direction as was the case with the nitrogen jet at higher energies.

Also of interest are the effects of non-linear Landau damping versus linear Landau damping evident in Figure 5.4 ($E_{CO_2} = 7.0\,\mathrm{J}$). Here no electrons are observed at $\varphi = 0°$, $\theta = 315°$ despite the recorded image of electrons trapped by an EPW at $\varphi = 0°$, $\theta = 135°$. This effect is attributed to fact that, while theory requires the presence of two EPW's travelling in nearly opposite directions, each wave need not be of equal amplitude. Indeed this is the case of Figure 5.4 where the EPW at $\theta = 135°$ was of sufficient amplitude that the effects of non-linear Landau damping become evident in the presence of electrons transported to the film. However, the corresponding EPW at $\theta = 315°$ was of such low amplitude that electrons were not trapped in the wave potential and damping of this EPW was accomplished by linear Landau damping.

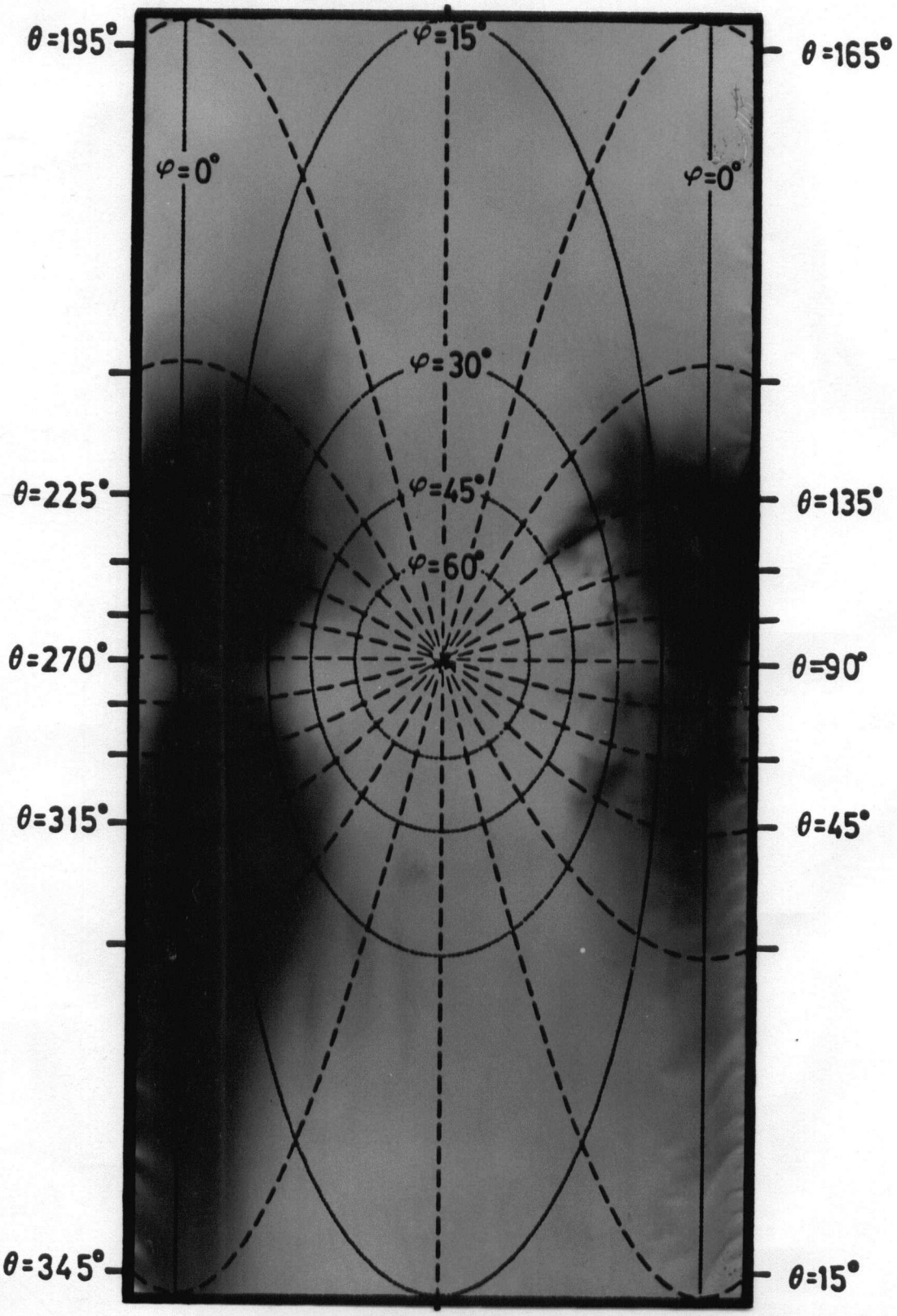

Figure 5.6 — Electron images obtained with a helium target ($E_{CO_2} = 5.0\,\mathrm{J}$).

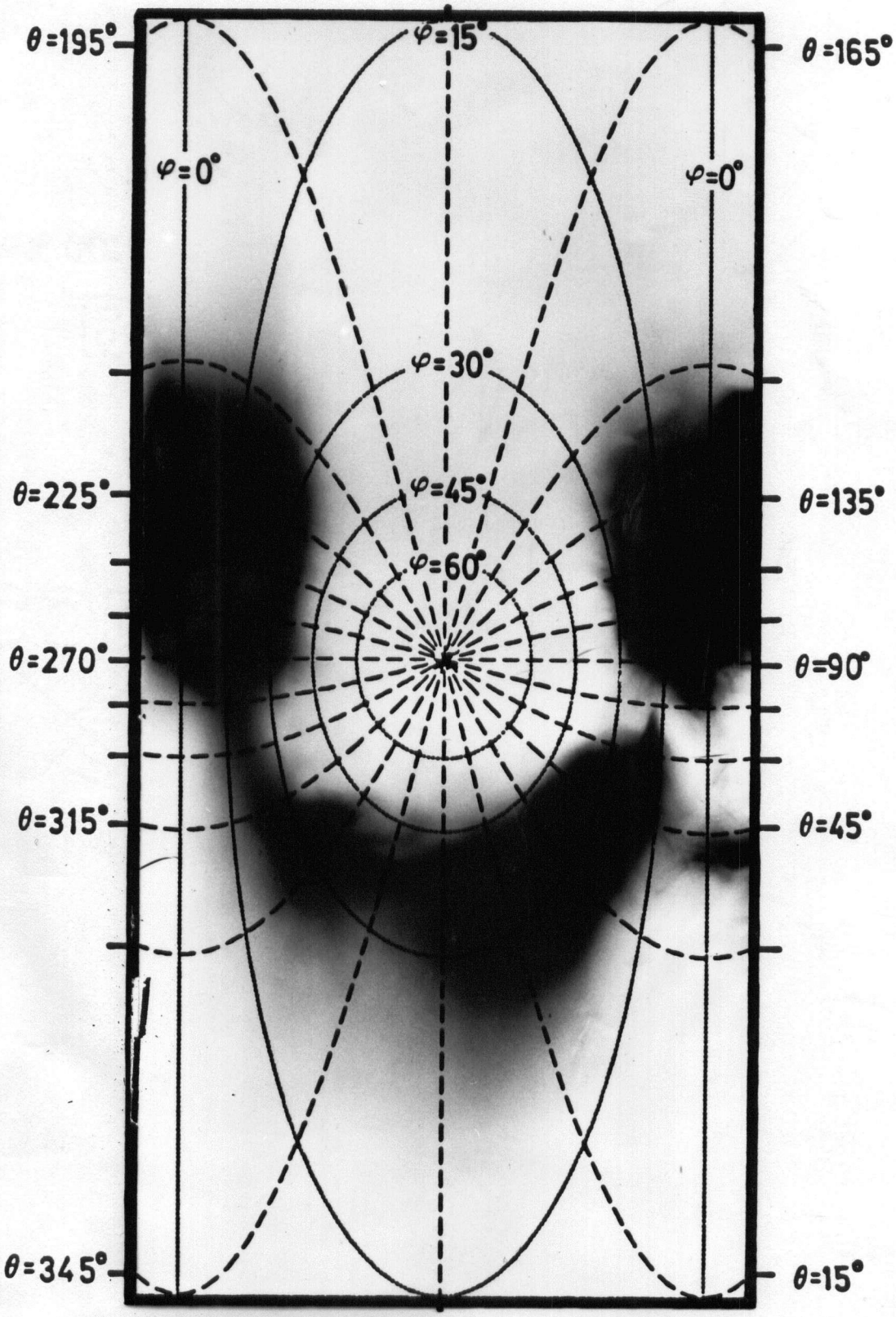

Figure 5.7 — Electron images obtained with a helium target ($E_{CO_2} = 6.0\,\mathrm{J}$).

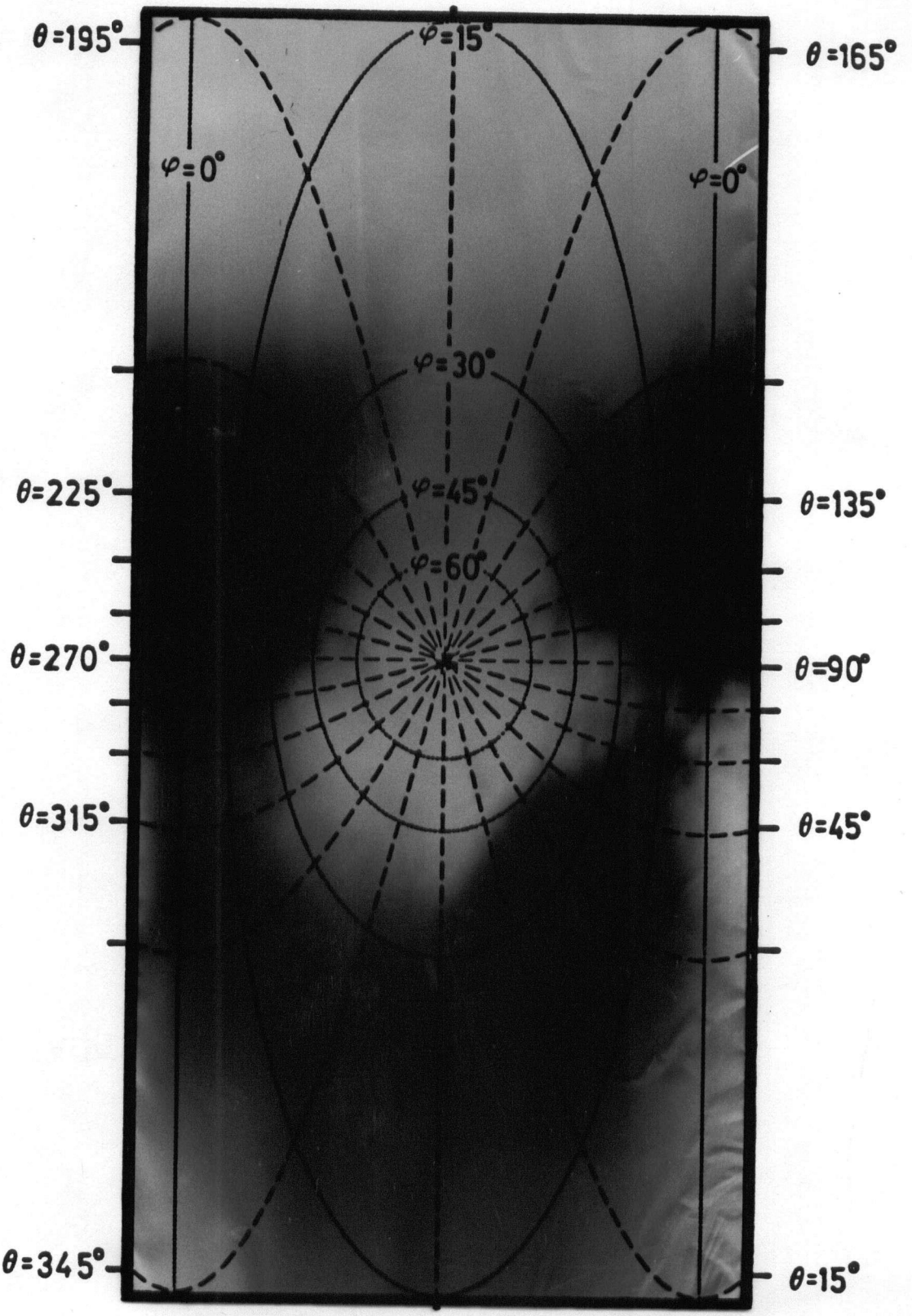

Figure 5.8 — Electron images obtained with a helium target ($E_{CO_2} = 7.0\,\mathrm{J}$).

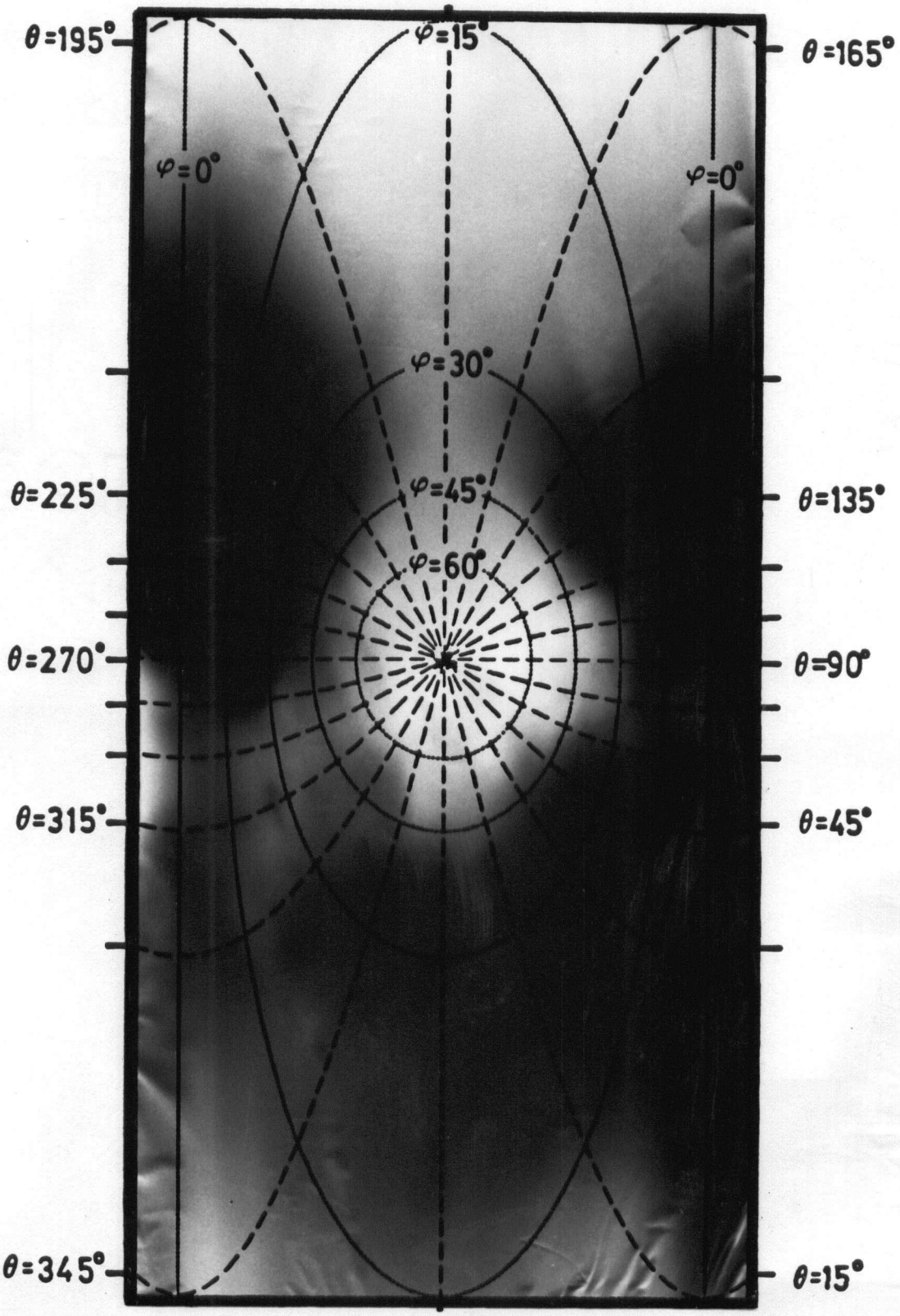

Figure 5.9 — Electron images obtained with a helium target ($E_{CO_2} = 8.5\,\mathrm{J}$).

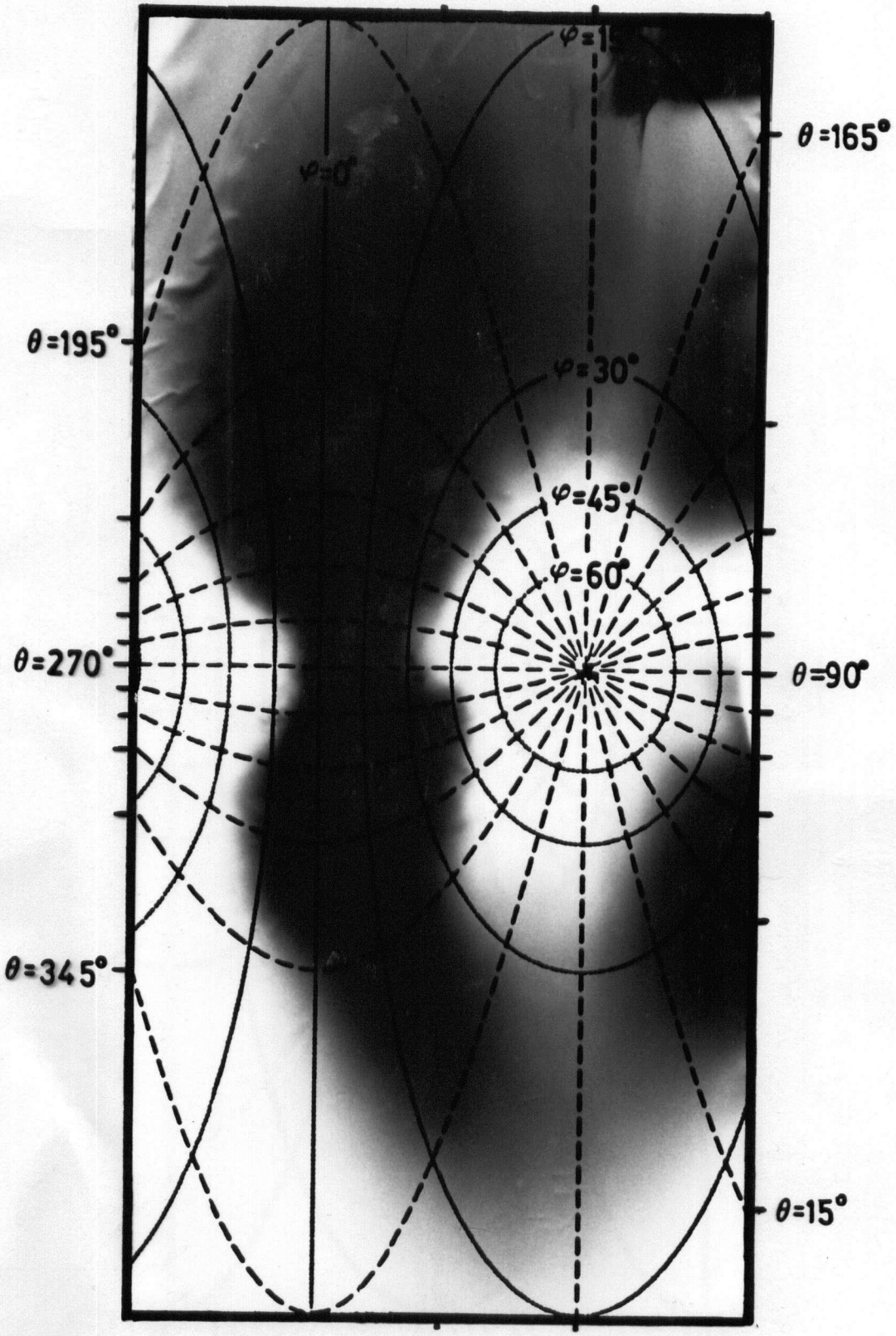

Figure 5.10 — Electron images obtained with the plane of polarization rotated 60°, a helium target and $E_{CO_2} = 6.0\,J$.

To investigate the effects of rotating the plane of polarization a half-wave plate[52] was inserted in front of mirror M_4 of Figure 3.2. With the optical axis of the plate at 30° to the plane of polarization, a 60° rotation of the plane at the target was observed as shown in Figure 5.10 with a helium gas target and $E_{CO_2} = 6.0\,J$. Once again electrons are observed outside the plane of polarization as in Figures 5.5 and 5.7 through 5.9.

2. The Spatial Distribution of the Electrons.

A more detailed evaluation of the spatial distribution of the electrons can be determined from densitometer readings of the negatives shown in §5.1. Some of the density contours obtained from those readings are shown in Figures 5.11 through 5.13. These contours feature the negatives shown in Figures 5.6 through 5.8 where the target gas was helium and the incident laser energies were 5.0, 6.0, and 7.0 J, respectively.

The 5.0 J shot indicates three regions where the electrons struck the film. All three regions are centered in the plane of polarization at $\theta = 126$, 228, and 322° ($k_y/k_o = 1.53$, 4.75, and 2.01). The 6.0 J shot shows three main regions, two in the plane of polarization at $\theta = 126$ and 228° ($k_y/k_o = 1.53$ and 4.75) and one above the plane of polarization at $\varphi = 30°$and $\theta = 39°$($k_y/k_o = 2.35$). In addition to these regions a smaller region is seen at $\varphi = 30°$ and $\theta = 325°$ ($k_y/k_o = 1.73$). The 7.0 J shot shows two main regions, both in the plane of polarization at $\theta = 134$ and 230° ($k_y/k_o = 14.32$ and 2.84). The clear evidence of electrons in the forward scattering direction as indicated in Figure 5.8 is evident here only as a minor contour centered at $\varphi = 19°$and $\theta = 28°$.

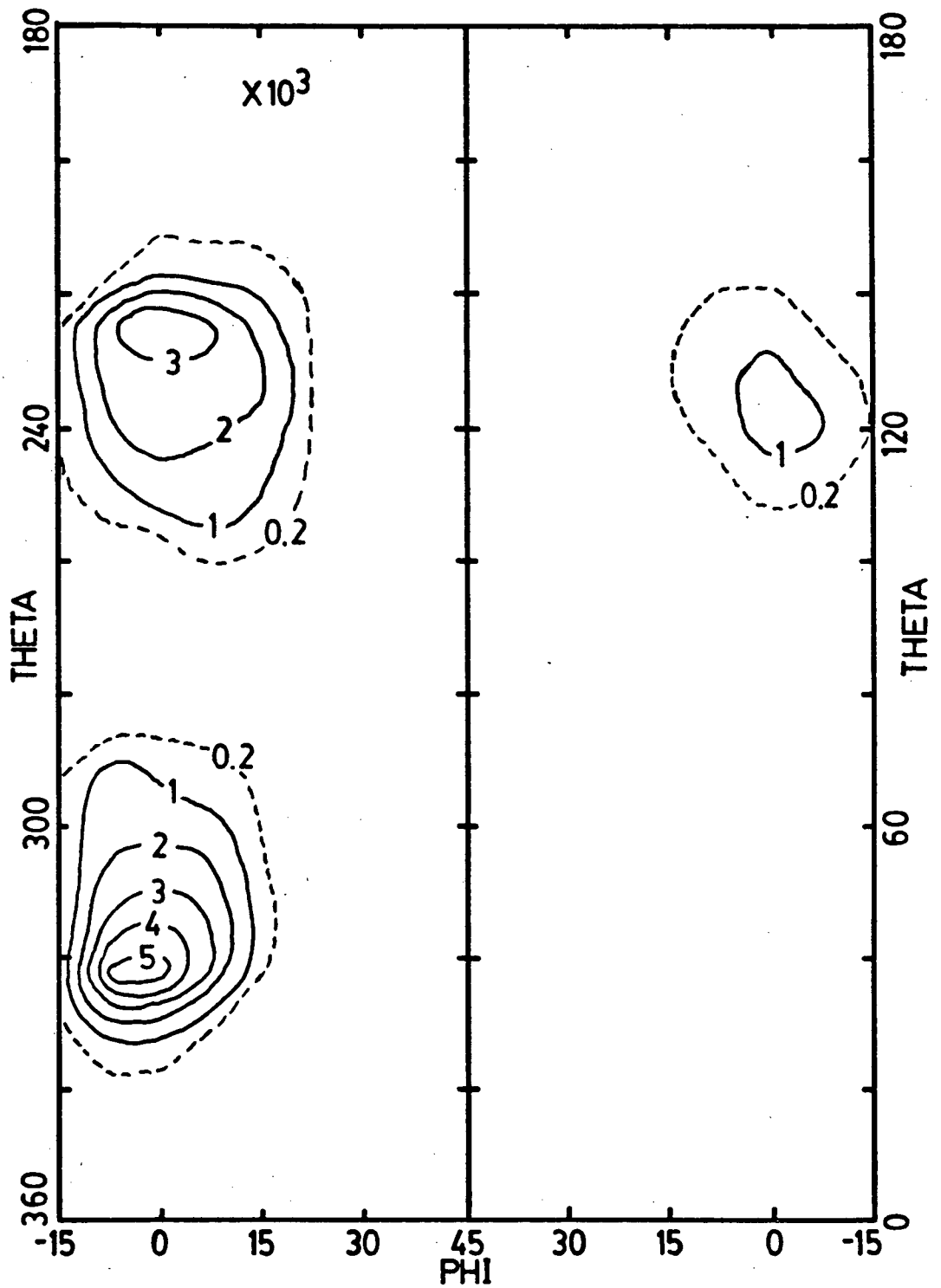

Figure 5.11 — Density contours of the negative shown in Figure 5.6 ($E_{CO_2} = 5.0\,\mathrm{J}$).

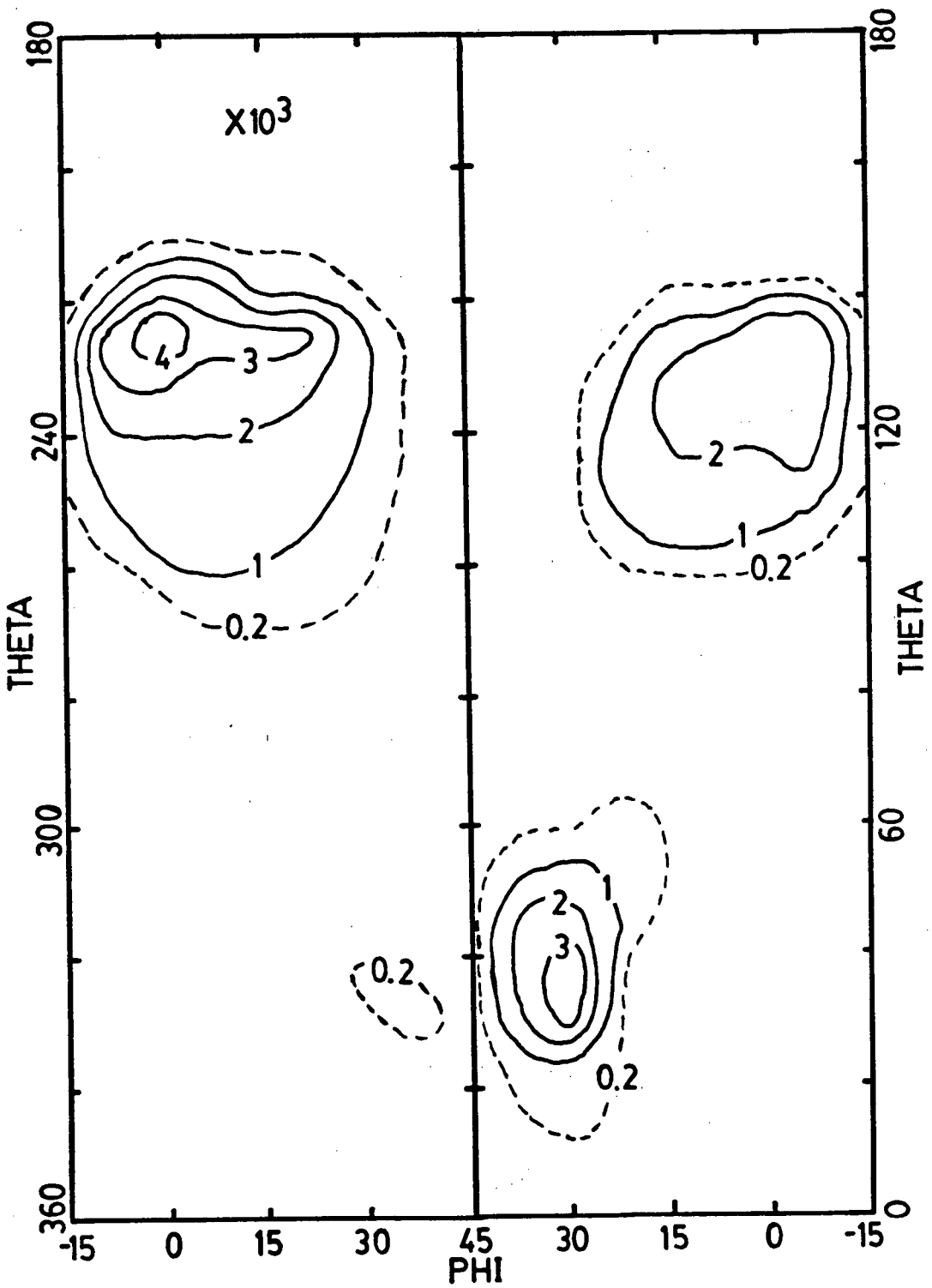

Figure 5.12 — Density contours of the negative shown in Figure 5.7 ($E_{CO_2} = 6.0\,\mathrm{J}$).

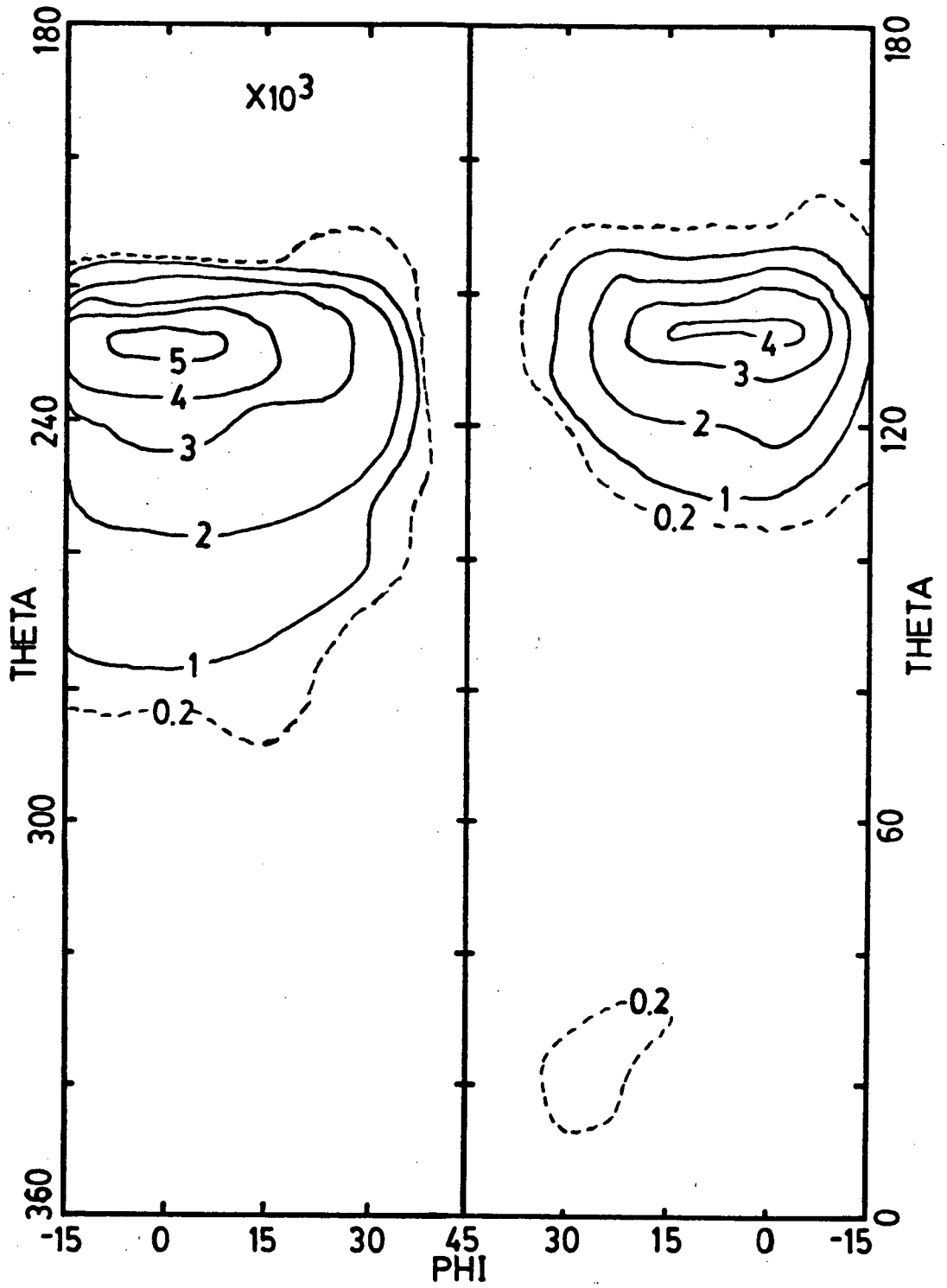

Figure 5.13 — Density contours of the negative shown in Figure 5.8 ($E_{CO_2} = 7.0\,\mathrm{J}$).

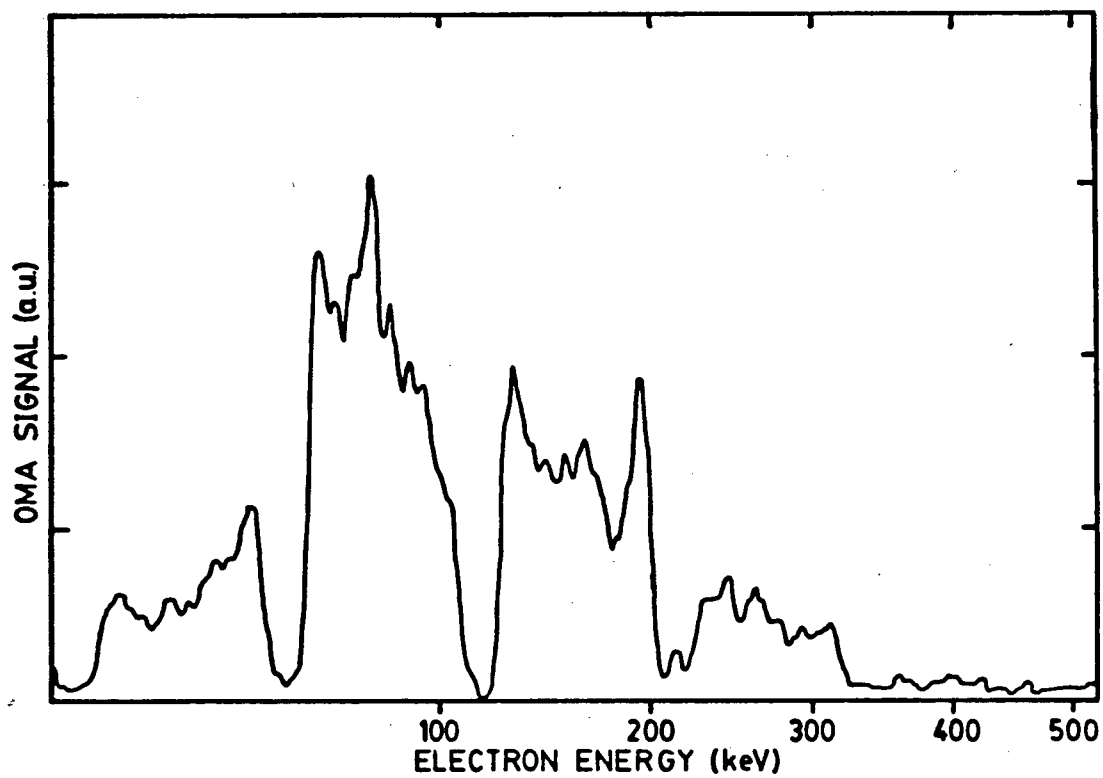

Figure 5.14 — The energy spectrum from a 4.5 J nitrogen plasma.

3. The Energy Spectrum of the Electrons.

Previous results[31–33] have indicated that the energy distribution of the hot electrons produced by the TPD instability obey a 3-D Maxwellian distribution function. Hence, the hot electrons generated by TPD can be characterized by an effective temperature T_h. Ebrahim,[31] Villeneuve,[32] and Meyer[33] report that, for laser interactions of sufficient duration, the energy spectrum of the electrons is given by

$$\frac{dN}{dE} = \frac{2N_o}{\sqrt{\pi}\,(k_b T_h)^{3/2}} \sqrt{E} \exp\left(\frac{-E}{k_b T_h}\right). \qquad (5\text{–}1)$$

Hence, a plot of $\ln\left(E^{-1/2} dN/dE\right)$ as a function of the energy E will yield a linear

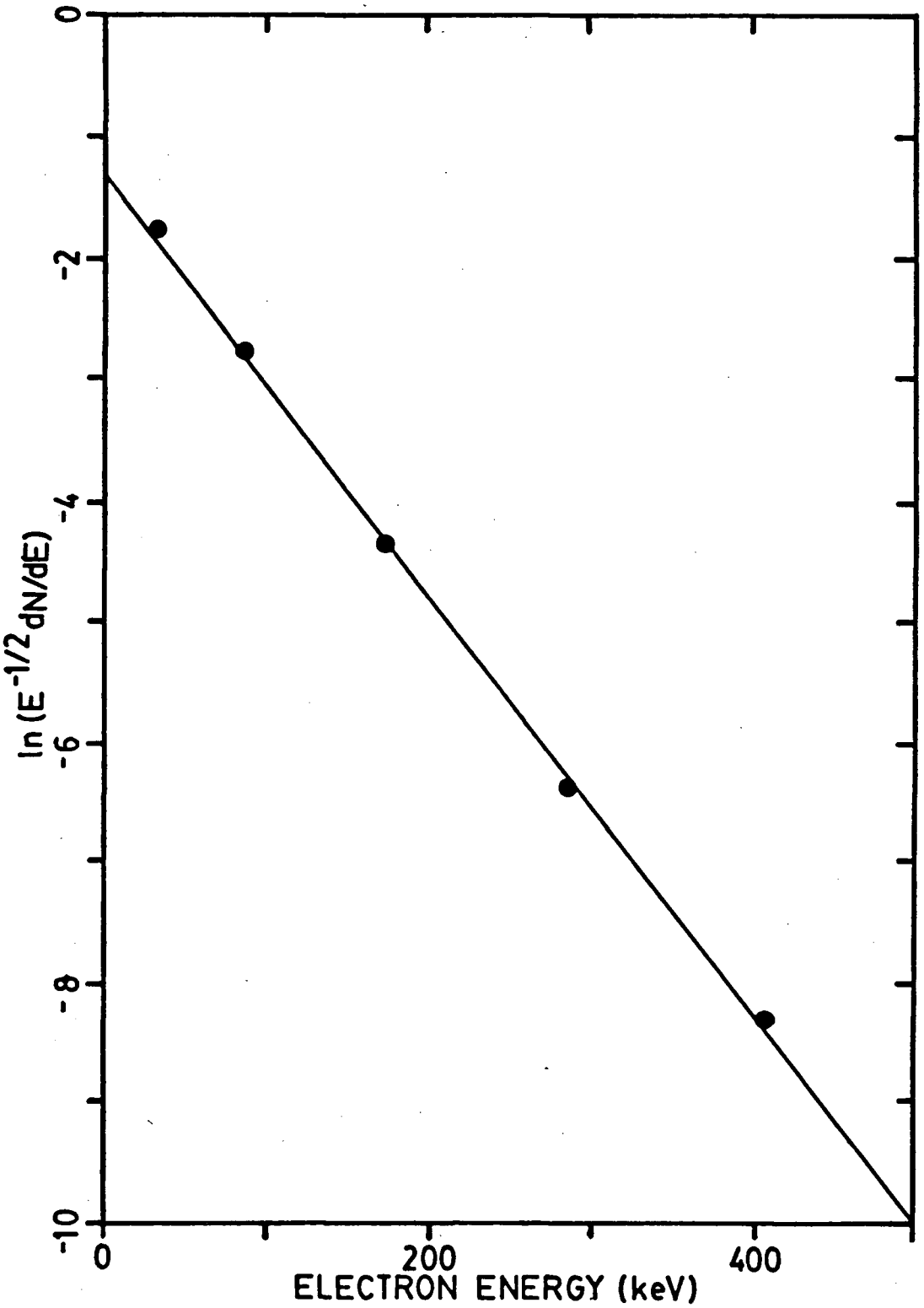

Figure 5.15 — The linear relation between $\ln\left(E^{-1/2}\,dN/dE\right)$ and laser energy verifying a 3-D Maxwellian distribution.

relationship with slope $-1/k_b T_h$ for electrons obeying the 3-D Maxwellian distribution function given by (5–1). It should be noted that this analysis will result in a low estimate of T_h due to the large space-charge potential which the electrons must overcome to escape the plasma.

Figure 5.14 shows a typical energy spectrum obtained with the spectrometer of §3.4a. The normalized values dN obtained from the spectrum using the factors listed in Table III–I yield the linear relation shown in Figure 5.15 with a slope corresponding to $T_h = 57\,\text{keV}$. This verifies the applicability of (5–1) even to the low energy laser shots such as that of Figure 5.14 ($E_{CO2} = 4.5\,\text{J}$).

As in previous reports,[32,33] there exists no correlation between T_h and the incident laser energy. Figures 5.16 and 5.17 show T_h for the nitrogen and helium targets, respectively, with the spectrometer placed in the region where growth rates of the EPW's are maximized ($\theta = 45°$, $\varphi = 0°$). The mean temperature of the electrons from the nitrogen target (99 keV with a standard deviation of 53 keV) is much lower than that of the helium target produced electrons (149 keV with a standard deviation of 54 keV).

Outside the region of maximum growth, the mean hot electron temperatures are lower than those at the maximum. Figure 5.18 shows T_h for various regions other than $\theta = 45°$, $\varphi = 0°$. Here similar mean values of T_h are found for both gas targets (92 keV with a standard deviation of 30 keV for nitrogen and 88 keV with a standard deviation of 15 keV for helium) regardless of the spectrometer position.

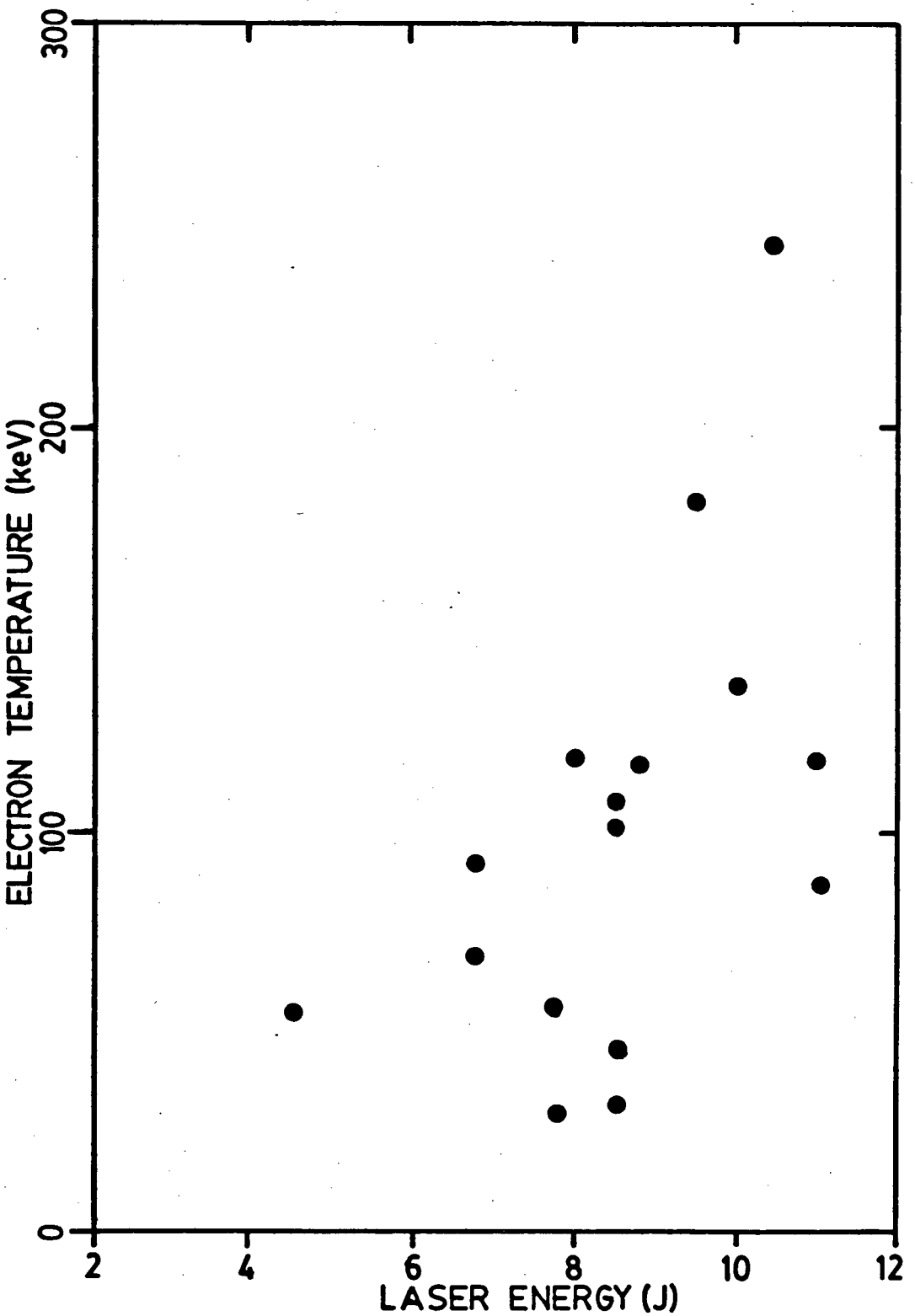

Figure 5.16 — The hot electron temperature as a function of laser energy for a nitrogen target ($\theta = 45°$, $\varphi = 0°$).

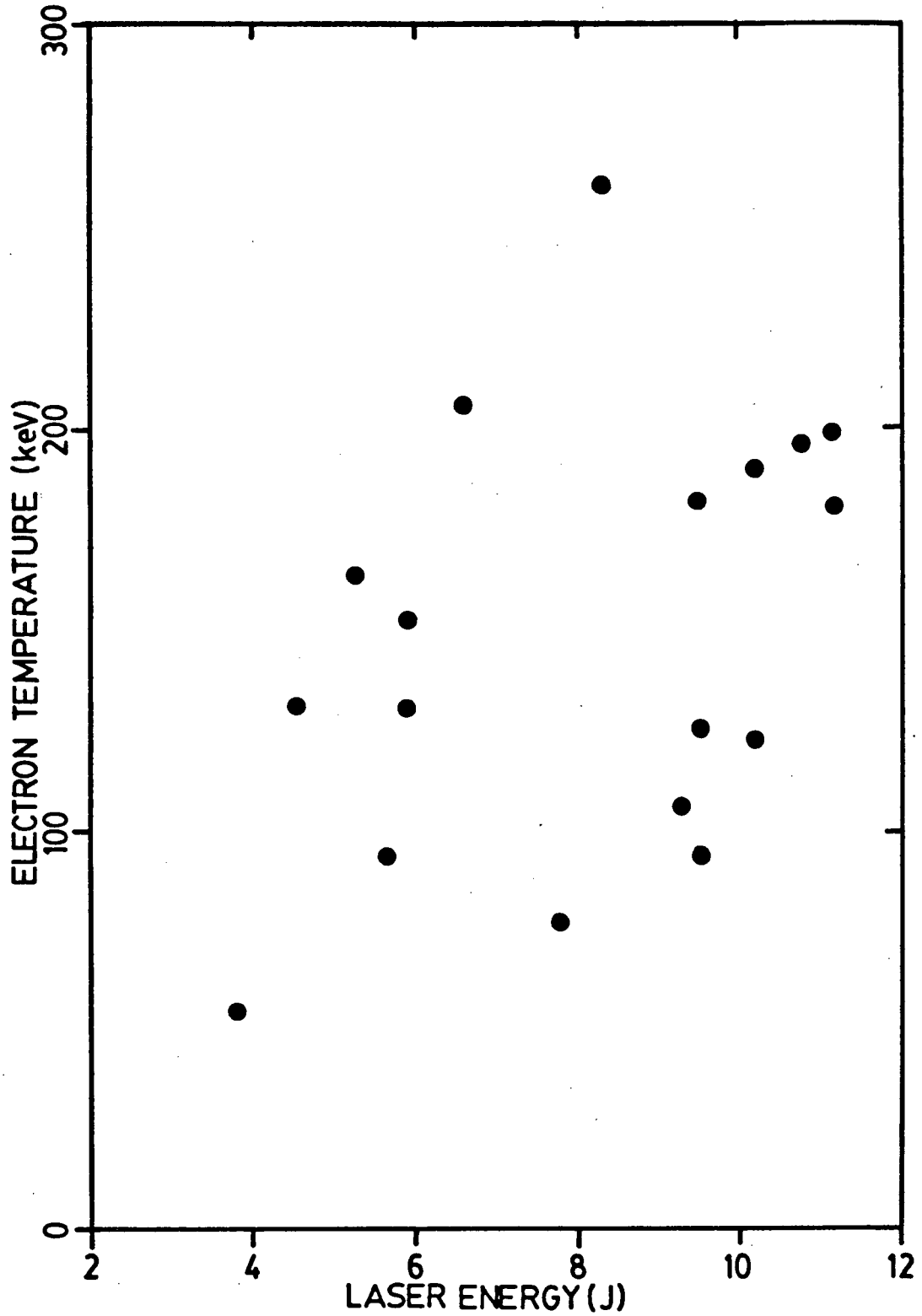

Figure 5.17 — The hot electron temperature as a function of laser energy for a helium target ($\theta = 45°$, $\varphi = 0°$).

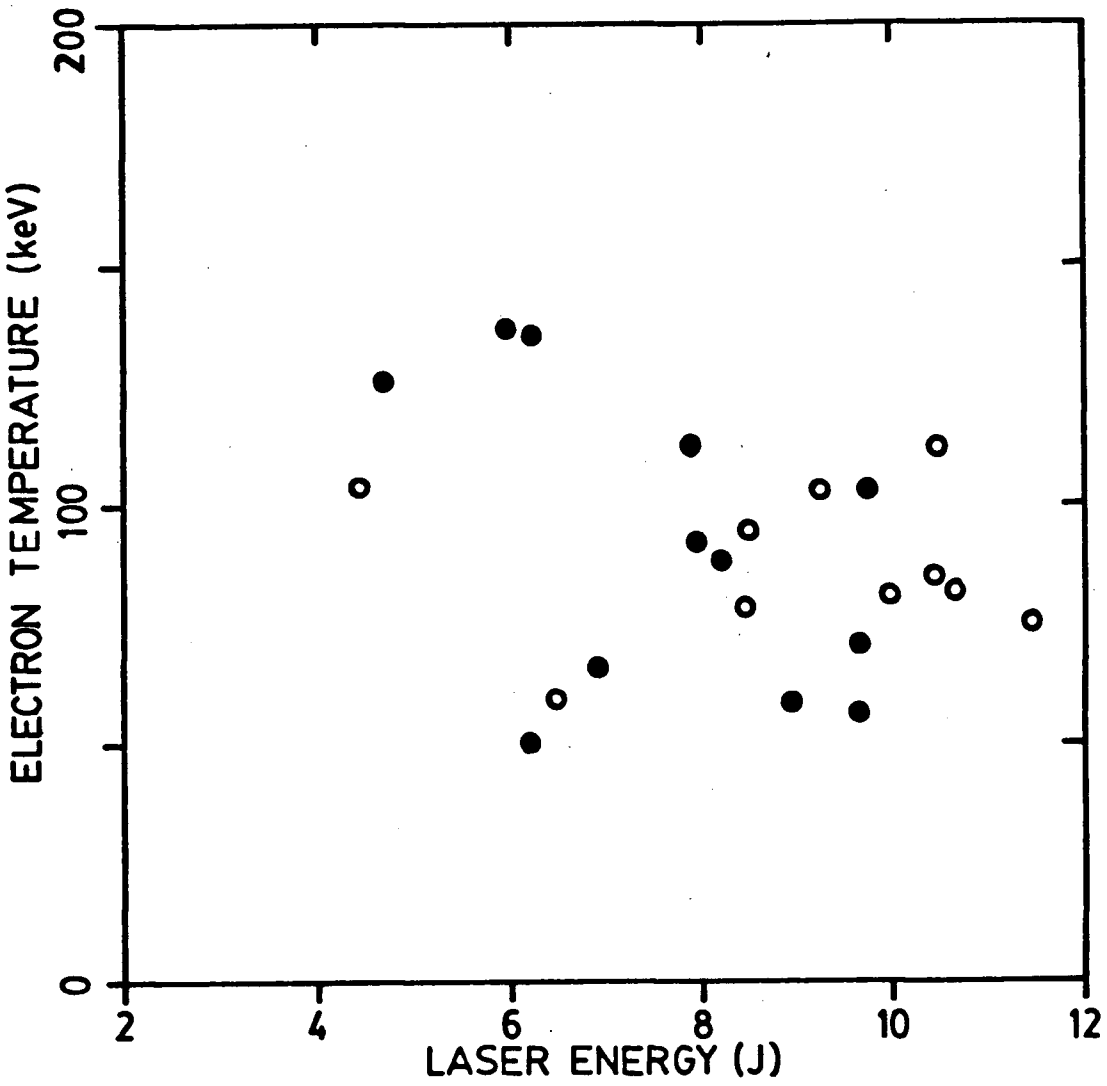

Figure 5.18 — The hot electron temperature as a function of laser energy outside the region of maximum growth rates for a nitrogen target (closed circles) and a helium target (open circles).

CHAPTER VI

DISCUSSION OF RESULTS AND CONCLUSIONS

In Chapter IV all the relevant plasma parameters of the helium jet were determined with the exception of the plasma temperature. Hence, this parameter is estimated below before the parameters of both the nitrogen and helium jets are summarized. Following this, the results of Chapters IV and V are compared to the theoretical predictions discussed in Chapter II, then the EPW's outside the plane of polarization are discussed before conclusions and future recommendations are presented.

1. The Plasma Temperature.

The plasma temperature can be obtained through the use of standard blast wave theory.[53] The high degree of uncertainty associated with the values derived with this theory arises due to several assumptions made which may not be applicable to laser produced plasmas: 1) self-similar motion; 2) adiabatic flow; 3) bounding of the blast wave by a shock wave; and 4) neglecting the effect of hot electrons in the equation of hydrodynamic motion. Nevertheless, this theory has been shown to yield estimates of the plasma temperature which agree with temperatures obtained

by other methods.[37] Basov[53] shows that the electron temperature is related to the velocity v_{CJ} of the blast wave at the Chapman-Jouguet (CJ) detonation (where the shock compression front and the heat expansion front are coincident) by

$$k_b T = \frac{2(\gamma - 1)}{(\gamma + 1)^2 A} v_{CJ} \tag{6–1}$$

where γ is the ratio of specific heats and $A = 5 \times 10^{14}$ erg/g. For the helium jet, (6–1) yields a value for the electron temperature in eV of

$$k_b T = 3.75 \times 10^{-9} v_{CJ}^2 \tag{6–2}$$

when v_{CJ} is given in m/sec.

Graphical analysis of radial expansion curves is used to determine v_{CJ}. At the instant of a CJ detonation, the slope of a log r–log t curve will undergo an abrupt change as can be seen in Figures 6.1a and 6.2a where a CJ detonation occurs at ~360 psec in the 6.0 J plasma and at ~850 psec in the 7.75 J plasma. The slopes of the radial expansion curves at the time of the detonation (Figures 6.1b and 6.2b) yield values of $v_{CJ} = \sim 3.7 \times 10^5$ and $\sim 2.5 \times 10^5$ m/sec and plasma temperatures of ~515 and ~240 eV, respectively for the 6.0 and 7.75 J plasmas. The lower temperature obtained with the higher energy laser beam is an indication of the inaccuracies involved in the graphical analysis of the data rather than an indication that a cooler plasma is observed for the higher energy beam. Hence, the plasma formed with the helium jet can at best be described as having a temperature of several hundred eV.

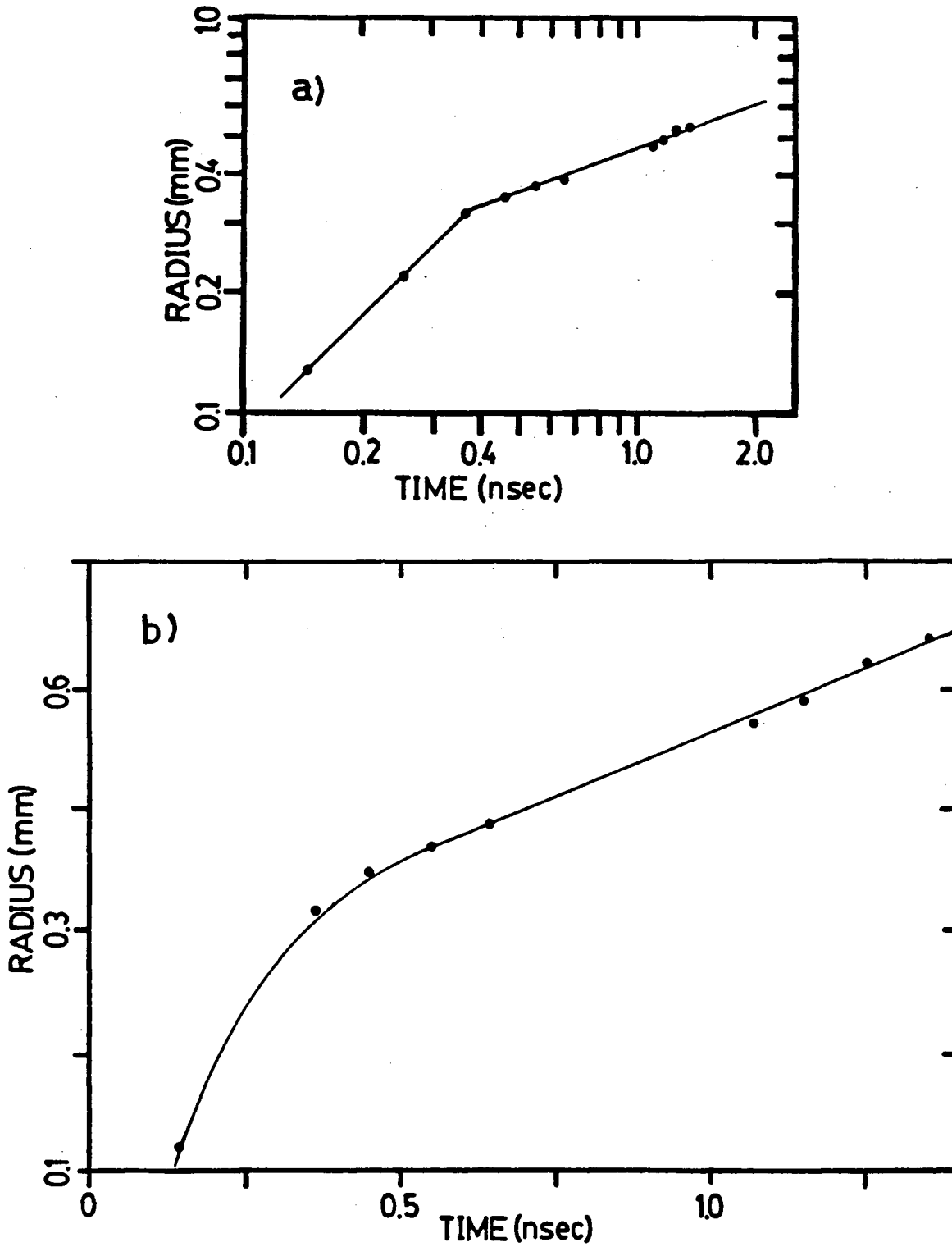

Figure 6.1 — The log-log plot (a) of the radial expansion of a 6.0 J helium plasma used to determine the Chapman-Jouguet detonation time at which v_{CJ} is determined from the radial expansion curve (b).

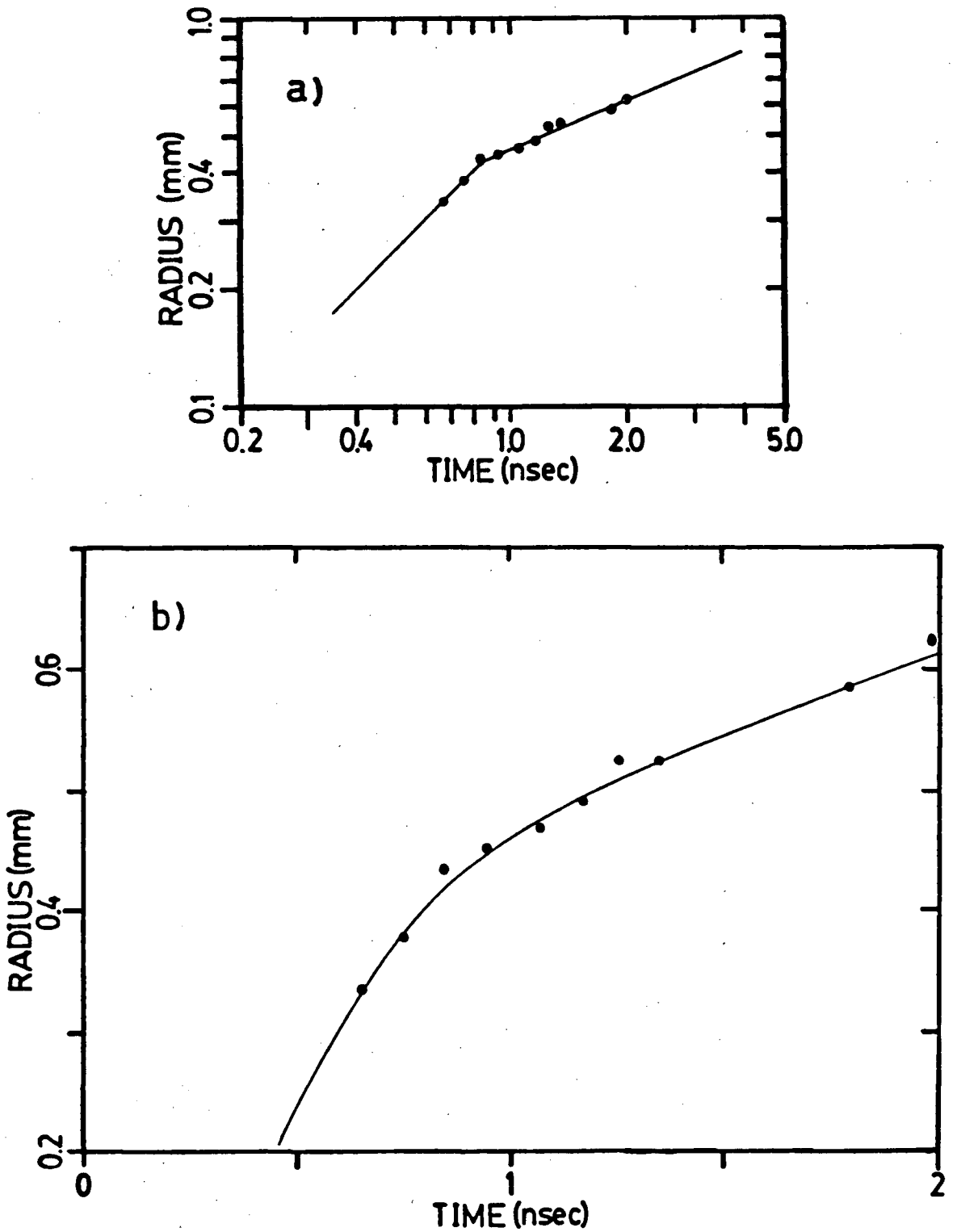

Figure 6.2 — The log-log plot (a) of the radial expansion of a 7.75 J helium plasma used to determine the Chapman-Jouguet detonation time at which v_{CJ} is determined from the radial expansion curve (b).

2. The Plasma Parameters.

The plasma parameters for helium jet have been found to be very similar to the parameters of the nitrogen jet previously reported[13,14,37]. Although both plasmas have scale lengths of the order of 50-700 μm along the quarter critical density boundary, the scale lengths measured for the helium jet were generally lower than the nitrogen jet by a factor of two for a given time during the laser pulse. Both plasmas attain densities of 0.4–0.5 $\times 10^{19}\,\mathrm{cm}^{-3}$ and the rough estimate of a few hundred eV for the plasma temperature of the helium jet agrees with the temperature estimates of the nitrogen jet based on observations of inverse bremsstrahlung absorption and thermal conduction and an analysis of radial expansion rates. Hence, theoretical predictions based on these parameters should yield similar results for both plasmas.

3. TPD Theory and EPW's in the Plane of Polarization.

TPD theory predicts that EPW's are formed with wave vectors in the plane of polarization, the xy-plane, at certain angles to $\vec{k}_o$ as discussed in §2.2. Since the theory makes no predictions for EPW's outside the plane of polarization, discussion of the applicability of the theory will be limited to the EPW's observed in the xy-plane and, for EPW's observed out of the xy-plane, to the projections of these EPW's onto the plane of polarization. Discussion of the observed wave vector components perpendicular to the xy-plane will be reserved to §6.4.

Figure 6.3 compares values of the magnitudes of $(k_y/k_o)_{max}$ for the six pairs of EPW's observed in Figures 5.2 and 5.5 through 5.8 to the theoretical predictions where curves (a) and (b) and the shaded area are the same as those discussed for Figure 2.2. The error bars indicate an uncertainty of $\pm 2°$ in determining θ. Of the four values observed in Figure 5.7 at $I_{14} = 0.38$, the values of $(k_y/k_o)_{max} = 1.37$ and 1.53 are for one pair of EPW's while the values of $(k_y/k_o)_{max} = 2.35$ and 4.75 are for the second pair. For each of the six pairs, the magnitudes of $(k_y/k_o)_{max}$

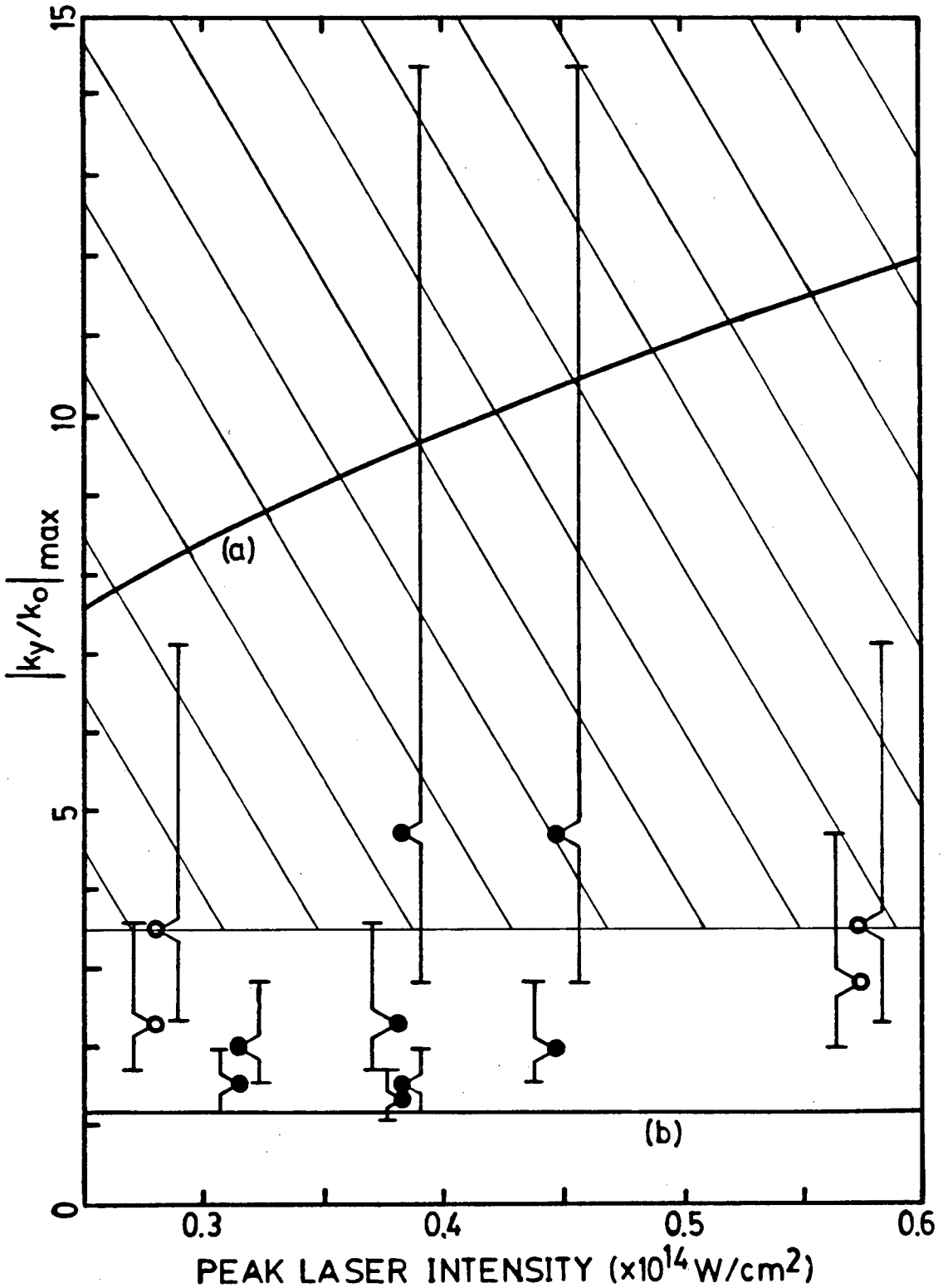

Figure 6.3 — Observed values of $(k_y/k_o)_{max}$ as a function of peak laser intensity.

are equal, within errors, as required by the wave vector matching condition (2-5). That none of the values of $(k_y/k_o)_{max}$ attain the predicted values (curve (a)) is attributed to Landau damping and to the fact that TPD will arise, be saturated and quenched on a short time scale[27] before the peak laser intensity of the pulse arrives at the plasma target.

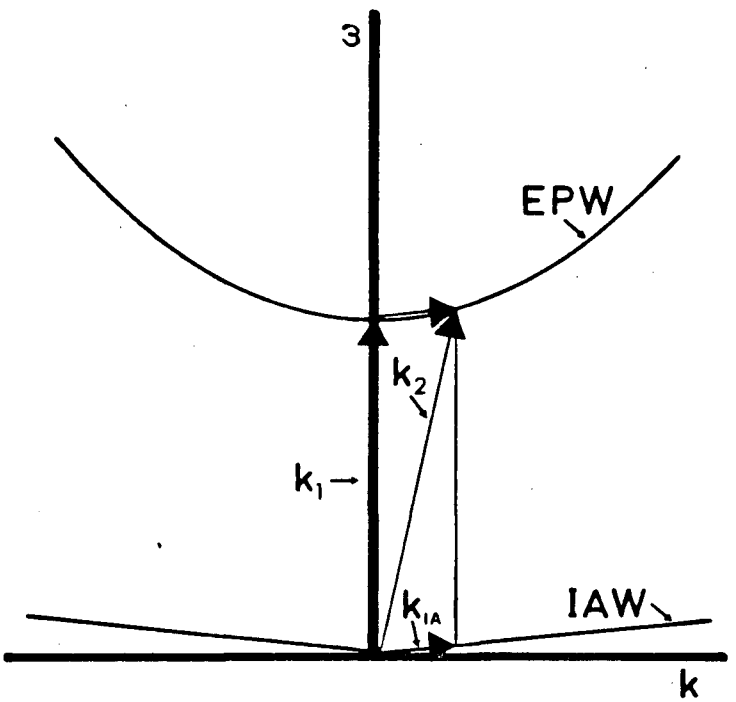

Figure 6.4 — The wave vector-frequency diagram of the electron decay instability.

4. EPW Vector Components Perpendicular to the Plane of Polarization.

The electron images of §5.1 indicate the presence of EPW's with wave vector components perpendicular to the plane of polarization while the discussion of §6.3 shows that the wave vector components in the xy-plane corroborate the theoretical predictions of §2.2. Hence, one can conclude that any wave vector with a vector component along the z-axis arises because of a process other than that of the TPD

instability – that the original EPW produced by TPD undergoes a process whereby a second EPW is generated from the original. The generation of this second EPW can be attributed to the electron decay instability.

The electron decay instability (EDI), as shown in the one dimensional wave vector-frequency diagram of Figure 6.4, arises when an EPW (ω_1, $\vec{k}_1$), with $k_{1z} = 0$ for the case in hand, decays into an EPW (ω_2, $\vec{k}_2$) and an ion acoustic wave (ω_{IA}, $\vec{k}_{IA}$). The frequency and wave vector matching conditions are given by

$$\omega_1 \simeq \omega_2 \pm \omega_{IA} \tag{6–3}$$

and

$$\vec{k}_1 \simeq \vec{k}_2 \pm \vec{k}_{IA}, \tag{6–4}$$

while the appropriate dispersion equations are given by

$$\omega_1^2 = \omega_p^2 + \frac{3}{2} v_e^2 k_1^2 \tag{6–5}$$

$$\omega_2^2 = \omega_p^2 + \frac{3}{2} v_e^2 k_2^2 \tag{6–6}$$

$$\omega_{IA}^2 = \left(\frac{Z k_b T_e + 3 k_b T_i}{m_i} \right) k_{IA}^2, \tag{6–7}$$

and the angle formed by the daughter EPW with the xy-plane is given by

$$\tan \varphi = \frac{k_{2z}}{\left(k_{2x}^2 + k_{2y}^2\right)^{1/2}} = \frac{k_{IAz}}{\left(k_{2x}^2 + k_{2y}^2\right)^{1/2}}. \tag{6–8}$$

The frequency matching condition (6–3) contains two equations. With

$$\omega_1 \simeq \omega_2 + \omega_{IA}, \tag{6–9}$$

it is easily determined that, since $\omega_1 > \omega_2$, $k_1 > k_2$ and geometric considerations show that φ will be maximized when the angle between $\vec{k}_2$ and $\vec{k}_{IA}$ equals 90°. Hence,

$$k_1^2 = k_2^2 + k_{IA}^2 \tag{6-10}$$

and algebraic manipulation of (6–3) through (6–7) with (6–10) yields

$$k_{IA} = \frac{2\omega_1}{(3v_e^2/2\alpha) + \alpha}, \tag{6-11}$$

where

$$\alpha^2 = \left(\frac{Zk_bT_e + 3k_bT_i}{m_i}\right), \tag{6-12}$$

with a maximum value for φ of

$$\sin\varphi_{max} = \frac{k_{IA}}{k_1}. \tag{6-13}$$

This equation, along with (6–10) and (6-11), is valid only for $k_1 > k_{IA}$. With $k_1 < k_{IA}$ the geometric considerations are different and $\varphi_{max} = 90°$ for $0 < k_1 < k_{IA}$. With the second frequency matching condition in (6–3)

$$\omega_1 \simeq \omega_2 - \omega_{IA} \tag{6-14}$$

and, since $\omega_1 < \omega_2$, $k_1 < k_2$. Geometric considerations show that φ will be maximized when the angle between $\vec{k}_1$ and $\vec{k}_{IA}$ equals 90°. Hence,

$$k_2^2 = k_1^2 + k_{IA}^2, \tag{6-15}$$

$$k_{IA} = \frac{2\omega_1}{(3v_e^2/2\alpha) - \alpha}, \tag{6-16}$$

and

$$\tan\varphi_{max} = \frac{k_{IA}}{k_1}. \tag{6-17}$$

The magnitude of the ion acoustic wave vector k_{IA} contributes little to the range of values of φ_{max} since, with $v_e^2 = k_b T_e/m_e$,

$$5.9 \times 10^{-9}\omega_1 \leq k_{IA} \leq 2.6 \times 10^{-9}\omega_1 \tag{6-18}$$

for $100 \leq T_e \leq 500\,\text{eV}$ and $T_i = 2\,\text{eV}$. However, there is a wide range of values for φ_{max} because of the dependence of k_1 on the electron density n_e. The magnitude of the wave vector of an EPW varies as the wave travels through an inhomogeneous plasma. With

$$\omega_p^2 = \frac{n_e e^2}{\epsilon_o m_e}, \tag{6-19}$$

where ϵ_o is the permittivity of free space and e and m_e are the electron charge and mass, for a given wave frequency and electron thermal velocity the wave vector magnitude from (6–5) is

$$k^2 = \frac{2}{3v_e^2}\left(\omega^2 - \frac{n_e e^2}{\epsilon_o m_e}\right). \tag{6-20}$$

Since $\omega^2 \simeq \omega_p^2$ for an EPW, any small increase in n_e results in a large decrease in k and the maximum density n_{max} into which the EPW can propagate (the density for which $\omega_1^2 = \omega_p^2$) is quickly reached.

Of the two frequency matching conditions (6–9) yields values of φ_{max} which are greater than those yielded by (6–14). As can be seen in Figure 6.5, which shows values of φ_{max} plotted as a function of electron density for a 300 eV plasma ($T_i = 2\,\text{eV}$) with $Z = 2$ and $\omega_1 = 9 \times 10^{13}\,\text{sec}^{-1}$($k_{1y} = 1.53\,k_{CO_2}$ and $k_{1x} = 2.12\,k_{CO_2}$ at $n_e = 2.5 \times 10^{18}\,\text{cm}^{-3}$), φ_{max} rapidly approaches 90° as n_e approaches $2.55 \times 10^{18}\,\text{cm}^{-3}$ for EPW's scattered in the forward direction. Conversely, EPW's in the

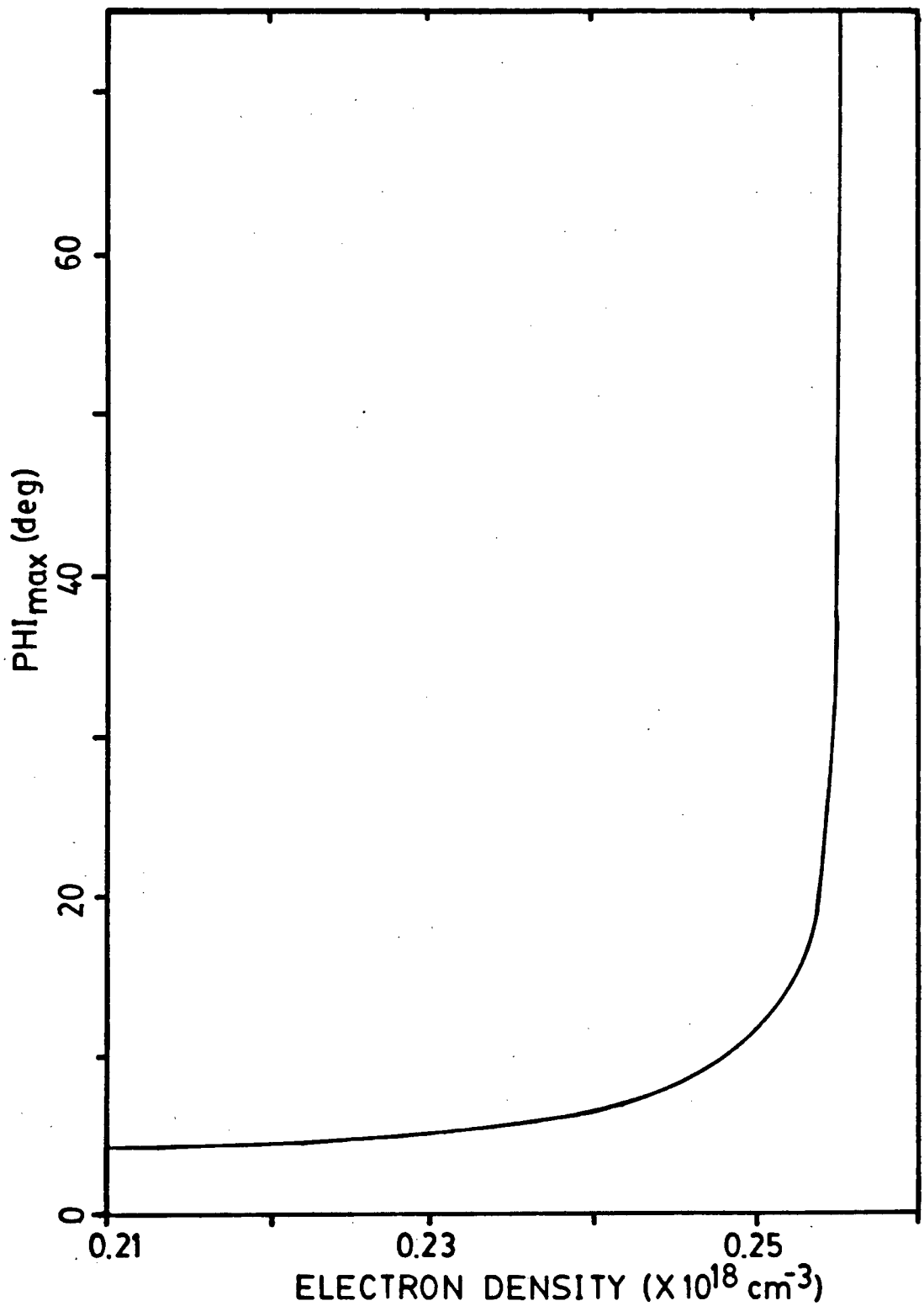

Figure 6.5 — Values of φ_{max} as a function of the electron density.

backscattered direction encounter a falling density gradient for which $\varphi_{max} < 11.0°$. Experimentally, values of φ were observed up to $\sim 55°$ in the forward scattering direction and up to $\sim 8°$ in the backscattered direction.

The observation of EPW vector components outside the xy-plane only at high laser energies can be attributed to the short scale lengths present when the intensities required for the onset of TPD are reached. The constant rise time of the laser pulse independent of peak intensity results in the observed threshold intensity of $\sim 2.5 \times 10^{13}\,\mathrm{W/cm^2}$ ($E_{CO_2} = 4\,\mathrm{J}$) arriving at the plasma at times ranging from $t = 0\,\mathrm{psec}$ for an 8 J laser pulse to $t = 600\,\mathrm{psec}$ for a 4 J pulse. (Here $t = 0$ refers to the arrival of the half maximum of the rising edge of the laser pulse.) For these times, Figure 4.8 shows that the scale length varies from $\sim 50\,\mu\mathrm{m}$ to $\sim 250\,\mu\mathrm{m}$ for the helium jet while reference 14 shows the scale length varies from $\sim 125\,\mu\mathrm{m}$ to $\sim 300\,\mu\mathrm{m}$ for the nitrogen jet ($t = 0$ and $t = 600\,\mathrm{psec}$, respectively). The difference in scale lengths between the two gases for a given time t can be attributed to the different ionization rates of the two gases. At the minimum laser energies when electrons are observed outside the xy-plane ($\sim 6.0\,\mathrm{J}$ for the helium jet and ~ 8.0 J for the nitrogen jet) the scale lengths are $\sim 125\,\mu\mathrm{m}$ for both plasmas when the threshold intensity is reached. Hence, EPW's produced by TPD in plasmas with scale lengths $< \sim 125\,\mu\mathrm{m}$ will undergo the EDI and accelerate electrons outside the plane of polarization.

5. Conclusions and Future Recommendations.

The production of hot electrons by the two-plasmon decay instability in a CO_2 laser produced plasma (with both helium and nitrogen as target gases) was examined in this work in which several original contributions were made to the field of laser fusion. The first original contribution was the characterization of the plasma formed with the helium target using a novel multi-frame interferometer the results of which were summarized in §6.2. The second contribution was the utilization of

photographic film to determine the spatial distribution of the TPD-produced hot electrons for a single laser-plasma interaction. The final original contribution was the first reported evidence of the modification of TPD-produced EPW's by the electron decay instability.

For the first time, clear indications of hot electrons outside the plane of polarization were observed for both target gases. For both gases, no hot electrons were observed for incident energies below ~4.0 J ($I = 2.5 \times 10^{13}$ W/cm^2). At energies up to ~8.0 J for the nitrogen target and ~5.5 J for the helium target, electrons were observed in the plane of polarization at the locations predicted by the TPD theory. However, for higher energies when the scale length of the plasma at the onset of TPD is small ($<\sim 125\,\mu$m), the EPW's produced by TPD are modified by the electron decay instability and the resultant EPW's acquire a vector component perpendicular to the plane of polarization. The magnitude of this component is strongly dependent on the electron density and, as a result, the EPW's propagating towards the higher density regions of the plasma decay into EPW's which are observed up to 55° outside the plane of polarization. EPW's propagating towards the lower density regions of the plasma are affected by the electron decay instability to a much lesser extent and, when affected, decay into EPW's which are observed up to 15° outside the plane of polarization.

The hot electrons produced in the plane of polarization in the regions of maximum growth were found to have greater mean temperature than those produced outside these regions. The electrons observed with the helium target at $\theta = 45°$, $\varphi = 0°$ were found to have a higher mean temperature than those observed with the nitrogen target at the same position (149 keV versus 99 keV). The electrons observed outside this region had the same mean temperature of ~90 keV regardless of the target gas.

Future work in this area in required in order to verify the occurrence of the electron decay instability. Thomson scattering of a probe beam by the ion acoustic

waves in the plane perpendicular to the xy-plane containing the forward scattered EPW's would provide experimental evidence of the EDI. Verification of the process by computer simulation would require an extensive three dimensional model rather than the two dimensional models generally available.

BIBLIOGRAPHY

1. Miley, G.H., *Fusion Energy Conversion*, (American Nuclear Society, Hinsdale, Illinois, 1976).
2. Klotz, I.M. and Rosenberg, R.M., *Introduction to Chemical Thermodynamics*, 2nd ed., (Benjamin/Cummings Publishing Co., Menlo Park, California, 1976).
3. Forslund, D.W., Kindel, J.M., and Lee, K., Phys. Rev. Lett. 39, 284 (1977).
4. Ebrahim, N.A. and Joshi, C., Phys. Fluids 24, 138 (1981).
5. Kolodner, P. and Yablonovitch, E., Phys. Rev. Lett. 37, 1754 (1976).
6. Kruer, W.L., Phys. Fluids 15, 2423 (1972).
7. Kaw, P.K., Lin, A.T., and Dawson, J.M., Phys. Fluids 16, 1976 (1973).
8. Silin, V.P. and Tikhonchuk, V.T., Sov. Phys. JETP 54, 1075 (1981).
9. Estabrook, K., Phys. Rev. Lett. 47, 1396 (1981).
10. Chen, F.F., *Introduction to Plasma Physics and Controlled Fusion, Vol. I: Plasma Physics*, 2nd ed., (Plenum Press, New York, 1984).
11. Cohen, B.I. and Max, C.E., Phys. Fluids, 22, 1115 (1979).
12. Ng, A., Salzmann, D., and Offenberger, A.A., Phys. Rev. Lett., 43, 1502 (1979).
13. Bernard, J.E., Ph.D. Thesis, University of British Columbia (1985).
14. McIntosh, G., M.Sc. Thesis, University of British Columbia (1983).
15. Nishikawa, K., J. Phys. Soc. Japan 24, 916 (1968).
16. Silin, V.P., Sov. Phys. JETP 21, 1127 (1965).
17. Goldman, M.V., Ann. Phys. 38, 95 (1966).

18. Goldman, M.V., Ann. Phys. 38, 117 (1966).

19. Jackson, E.A., Phys. Rev. 153, 235 (1967).

20. Lee, Y.C. and Kaw, P.K., Phys. Rev. Lett. 32, 135 (1974).

21. Liu, C.S. and Rosenbluth, M.N., Phys. Fluids 19, 967 (1976).

22. Lasinski, B.F. and Langdon, A.B., in Laser Program Annual Report, Lawrence Livermore National Laboratory UCRL-50021-77, 1977, pp. 4-49.

23. Simon, A., Short, R.W., Williams, E.A., and Dewandre, T., Phys. Fluids 26, 3107 (1983).

24. Baldis, H.A., Samson, J.C., and Corkum, P.B., Phys. Rev. Lett. 41, 1719 (1978).

25. Baldis, H.A. and Walsh, C.J., Phys. Fluids 26, 1364 (1983).

26. Meyer, J., Bernard, J.E., Hilko, B., Houtman, H., McIntosh, G., and Popil, R., Phys. Fluids 26, 3162 (1983).

27. Meyer, J. and Houtman, H., Phys. Fluids 28, 1549 (1985).

28. Langdon, A.B., Lasinski, B.F., and Kruer, W.L., Phys. Rev. Lett. 43, 133 (1979).

29. O'Neil, T., Phys. Fluids 8, 2255 (1965).

30. Coffey, T.P., Phys. Fluids 14, 1402 (1971).

31. Ebrahim, N.A., Baldis, H.A., Joshi, C., and Benesch, R., Phys. Rev. Lett. 45, 1179 (1980).

32. Villeneuve, D.M., Keck, R.L., Afeyan, B.B., Seka, W., and Williams, E.A., Phys. Fluids 27, 721 (1984).

33. Meyer, J., Bernard, J.E., Hilko, B., Houtman, H., McIntosh, G., and Popil, R., Phys. Rev. A 29, 1375 (1984).

34. Francis, J.R.D., *Fluid Mechanics for Engineering Students*, 4th ed., (Williams Clowes and Sons Ltd., London, 1975).

35. Shapiro, A.H., *Dynamics and Thermodynamics of Compressible Fluid Flow*, Vol. I (Ronald Press Co., New York, 1953).

36. Smith, D.C. and Meyerand, R.G., in *Principles of Laser Plasmas*, ed. by Behefi, G. (Wiley, 1976) pp. 475-507.

37. Popil, R., Ph.D. Thesis, University of British Columbia (1984).

38. Born, M. and Wolf, E., *Principles of Optics*, 4th ed., (Permamon Press, London, 1970).

39. Bracewall, R.N., *The Fourier Transform and Its Applications*, 2nd ed. (McGraw Hill, New York, 1978) pp. 262-264.

40. Houtman, H., Legault, L.E., and Meyer, J., Appl. Opt. 26, 1106 (1987).

41. Houtman, H. and Meyer, J., J. Appl. Phys. 57, 4892 (1985).

42. Alcock, A.J., Corkum, P.B., and James, D.J., Appl. Phys. Lett. 27, 680 (1975).

43. Boreli, F. and Grimeland, B., Nuovo Cimento 2, 336 (1955).

44. Prescott, J.R. and Rulual, A.S., Can. J. Phys. 39, 221 (1961).

45. von Schmeling, H.K., Zeit. Phys. 160, 520 (1960).

46. Dyson, N.A., *X-Rays in Atomic and Nuclear Physics* (Longman, London, 1973).

47. Jahoda, F.C., Little, E.M., Quinn, W.E., Sayer, G.A., and Stratton, T.F., Phys. Rev. 119, 843 (1960).

48. Cosslett, V.E., in *X-Ray Optics and Microanalysis*, ed. by Custaing, R., Descamps, P., and Philibert, J. (Hermann, London, 1966).

49. Dudley, R.A., Nucleonics 12, 25 (1954).

50. Houtman, H. and Meyer, J., Appl. Opt. 23, 2178 (1984).

51. Ahlborn, B. and Liese, W., Phys. Fluids 24, 1955 (1981).

52. Hecht, E. and Zajac, A., *Optics* (Addison-Wesley, Menlo Park, California, 1079).

53. Basov, N.G., Gamaly, E.G. Krokhin, O.N., Mikhailov, Yu.A., Shlizkov, G.V. and Fedotov, S.I., in *Laser Interaction and Related Plasma Phenomena*, Vol. 3B, ed. by Schwarz, H. and Hora, H. (Plenum Press, New York, 1974).